Integrated-Optics Components Utilizing Long-Range Surface Plasmon Polaritons

Boltasseva, Alexandra

Publication date:
2004

Document Version
Publisher's PDF, also known as Version of record

INTEGRATED-OPTICS COMPONENTS UTILIZING LONG-RANGE SURFACE PLASMON POLARITONS

Alexandra Boltasseva

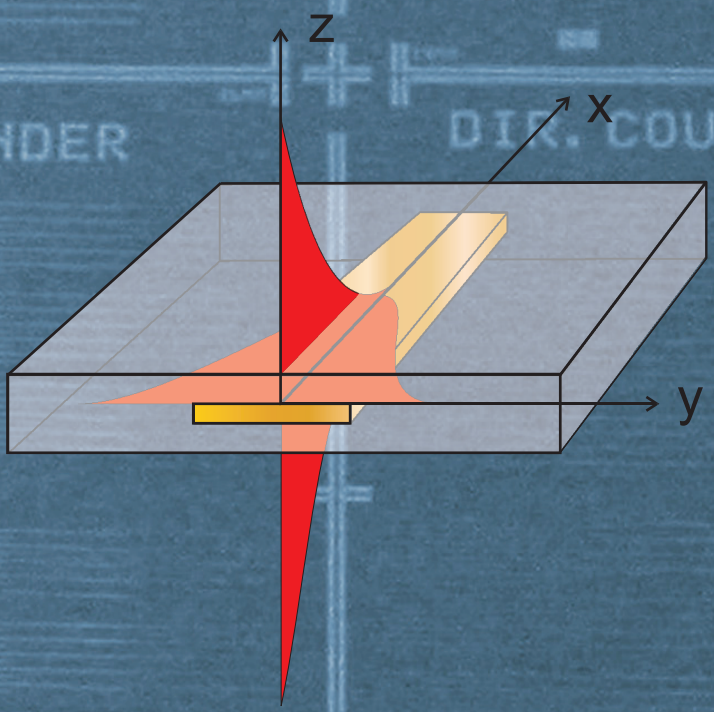

Research Center COM
June 2004

Abstract

This thesis describes a new class of components for integrated optics, based on the propagation of long-range surface plasmon polaritons (LR-SPPs) along metal stripes embedded in a dielectric. These novel components can provide guiding of light as well as coupling and splitting from/into a number of channels with good performance.

Guiding of LR-SPPs along nm-thin and µm-wide gold stripes embedded in polymer is investigated in the wavelength range of 1250 – 1650 nm. LR-SPP guiding properties, such as the propagation loss and mode field diameter, are studied for different stripe widths and thicknesses. A propagation loss of ~ 6 dB/cm, a coupling loss of ~ 0.5 dB (per facet), and a bend loss of ~ 5 dB for a bend radius of 15 mm are evaluated for 15-nm-thick and 8-µm-wide stripes at a wavelength of 1550 nm. LR-SPP-based 3dB power Y-splitters, multi-mode interference waveguides, and directional couplers are also fabricated and optically characterized. At 1570 nm, coupling lengths of 1.9 and 0.8 mm are found for directional couplers with waveguides separated 4 and 0 µm, respectively. LR-SPP-based waveguides and waveguide components are modeled using the effective-refractive-index method and a good agreement with experimental results is obtained.

The interaction of LR-SPPs with photonic crystals (PCs) is also studied. The PC structures are formed by periodic arrays of gold bumps that are arranged in a triangular lattice and placed symmetrically on both sides of a thin gold film. The LR-SPP transmission through and reflection from the PC structures of different lengths and lattice periods as well as the LR-SPP propagation along line defects of different widths are investigated. The experimental results indicate that the multiple LR-SPP scattering, occurring in the investigated PC structures, is rather weak, so that the photonic band gap might be expected only for some particular propagation directions. The possibilities of achieving a full band gap (in the surface plane) for LR-SPPs as well as use of the weak coherent-scattering effect are discussed.

The effective index contrast, achieved in the investigated metallic structures, is found to be large enough for the realization of efficient and compact integrated Bragg gratings. Propagation of LR-SPPs along periodically thickness-modulated metal stripes is studied at telecom wavelengths for different grating parameters. Well pronounced Bragg-grating behavior is exploited to realize a compact wavelength add-drop filter with a bandwidth of ~ 20 nm centered at 1550 nm.

Resumé

Denne afhandling beskriver en ny klasse af komponenter til integreret optik baseret på guidning af langtrækkende overfladeplasmonpolaritoner (LR-SPPs, engelsk) langs tynde metalstriber indlagt i et dielektrikum. Disse unikke komponenter kan danne basis få både guidning, kobling samt splitting til og fra forskellige kanaler i et telekommunikationssystem.

Guidning af LR-SPPs ad nm-tynde og µm-bredde guldstriber indlagt i en polymer, er undersøgt i bølgelængdeområdet 1250-1650 nm. Guidningsegenskaberne af LR-SPPs, såsom transmissionstab og modefield diameter er studeret for forskellige stribebredder og tykkelser. For 15 nm tykke og 8 µm brede striber findes, ved 1550 nm, et transmissionstab på ~ 6 dB/cm, et koblingstab på ~ 0.5 dB (per facet) og et bøjningstab på ~ 5 dB for en bøjningsradius på 15 mm. Ydermere er der fabrikeret og karakteriseret både 3dB power splittere, multi-mode interferensbølgeledere og koblere baseret på LR-SPPs. Ved 1570 nm findes koblingslængder på 1.9 og 0.8 mm for koblere med henholdsvis 4 og 0 µm afstand mellem bølgelederne. LR-SPP-baserede bølgeledere og bølgelederkomponenter er simuleret via effektiv-refraktivt-index metoden, og der findes god overensstemmelse mellem eksperimentelle og teoretiske resultater.

Interaktionen mellem LR-SPPs og fotoniske krystaller er ligeledes blevet studeret. Fotoniske krystalstrukturer skabes ved at en periodisk matrix af guldbump, arrangeret på et triangulært gitter, placeres symmetrisk på hver sin side af en tynd guldfilm. Der er undersøgt transmission gennem og refleksion fra fotoniske krystalstrukturer med forskellig længde og med forskellig gitterkonstant, ligesom LR-SPP transmission gennem linjedefekter af forskellig bredde er blevet studeret. De eksperimentelle resultater indikerer, at den multiple spredning af LR-SPPs i den fotoniske krystalstruktur er temmelig svag, sådan at det fotoniske båndgab, man kunne forvente, kun optræder for udvalgte retninger i strukturen. Mulighederne for at skabe et fuldt båndgab for LR-SPPs (i planet), samt brugen af den svage kohærente spredningseffekt, diskuteres.

Den effektive indekskontrast, opnået i de studerede metalliske strukturer, viser sig at være stor nok til, at der kan realiseres effektive og kompakte integrerede Bragg-gitre. Transmission af LR-SPPs langs periodiskmodulerede metalstriber er, ved telekombølgelængder, studeret for forskellige gitterparametre. Endeligt er den opnåede Bragg-gitter-effekt blevet udnyttet til at realisere et kompakt bølgelængde add-drop filter med en båndbredde på ~ 20 nm centreret omkring 1550 nm.

Index

Acknowledgements

Feeling gratitude and not expressing it is
like wrapping a present and not giving it.
William Arthur Ward

This thesis is the result of my three years Ph.D. studies at the Optoelectronics group at Research Center COM. There are many people who have helped me during these years and I apologize for not mentioning all of them here. First and foremost, I would like to thank my supervisors Jørn M. Hvam (Research Center COM, Technical University of Denmark) and Sergey Bozhevolnyi (Department of Physics and Nanotechnology, Aalborg University) for all their support, guidance and encouragement. I had the unique opportunity to work in collaboration with the start-up company Micro Managed Photons A/S (MMP) during the last two years of my Ph.D. and I am deeply indebted to my "everyday" supervisors Kristjan Leosson and Thomas Nikolajsen for the introduction to the amazing world of surface plasmon polaritons and providing me with such an interesting and challenging project. With all their knowledge and expertise they have shared with me I had gotten a real possibility to participate in the development of the new exciting technology. That has been a really great experience to learn from ones so wise, clever and enthusiastic! Many thanks go to Thomas Søndergaard, Peter Madsen and Kasper Kjær for their help and cooperation. I would also like to thank the rest of my MMP colleagues for fruitful collaboration, useful discussions and nice company dinners. I owe our CEO Bonni Kryger my special thanks – without him this collaboration would not be possible.

I would like to express my sincere gratitude to the entire staff at the Optoelectronics group at COM for a nice friendly atmosphere and the Glass group for a fruitful collaboration within the PICCO project during my first year. Special thanks go to John Erland for inviting me to Denmark (where, after all, I have found not only interesting research project but also my love...) and introducing me to the Danish society and photonic band-gap structures. I am also grateful to Peter Skovgaard for his enthusiasm and support during my first months at COM, to Jesper Arentoft and Martin Kristensen for the introduction to SOI-based planar photonic crystal waveguides and nice collaboration within the PICCO project. I have also enjoyed the cooperation with Peter Borel, Andrei Lavrinenko, Bjarne Tromborg, Valentyn Volkov, and Lars Fradsen.

Also many thanks and my sincere gratitude go to everyone who has proof-read this thesis.

I would like to take the opportunity to acknowledge my former M.Sc. supervisors Alexander Bogatov and Alexander Drakin from P. N. Lebedev Physical Institute of Russian Academy of Sciences for their excellent knowledge and guidance during my master studies that gave me a good start for a Ph.D. study. I am also very grateful to my school teacher of physics Valeri Gorbenko for his catching enthusiasm and physical insight, excellent classes and many-many hours of getting though tricky problems with elegant solutions that, after all, determined my future as a physicist and researcher.

I must also give greatest thanks to my dad for the early introduction to his beloved world of electrical circuits, transformers, colorful resistors and oscilloscopes and his intriguing stories about Big Bang, electrons and black holes, when I was a child; to my mom for her understanding and respecting my choice, which turned out to be slightly different from her dream careers of pediatrician or musician; and to my sister for the living example of getting a Ph.D. degree (in philosophy though) and our endless talks about philosophical problems of modern sciences that stimulated my thought process.

Last but not least, my deep love and sincere gratitude go to my husband, Kim, and my daughter, Victoria, for all their support, love, patience and humor that brighten my days, for bearing with my bad mood in frustrating periods and for always being a light in my life that turns every sun ray into a small miracle.

Preface

"Where shall I begin, please your Majesty?" the White Rabbit
asked. "Begin at the beginning," the King said, very gravely,
"and go on till you come to the end: then stop."
Lewis Carroll, "Alice's Adventures in Wonderland"

I would like to start with some comments about the Ph.D. project, which underwent some transformation on its way, even in its title: It has been changed from "Semiconductor Photonic Crystals for Genuine Integrated Optics and Ultracompact Optical Components" to "Integrated-Optics Components Utilizing Long-Range Surface Plasmon Polaritons". It was a three-year-learn and three-year-change. The project was revolving around nanotechnology and compact optical components, turning from semiconductors to silicon-on-insulator, from photonic crystals to stripe waveguides and back to photonic crystals, only this time in a metal-dielectric system. Since I was mainly involved in the fabrication and optical characterization processes, I had a possibility to work with different material systems – from III-V semiconductors through standard silicon and silicon-on-insulator to metals and advanced optical polymers.

The project started as part of the European IST project "Photonic Integrated Circuits using Photonic Crystal Optics" (PICCO), developing photonic band-gap structures based on two different materials: GaAs and silicon-on-insulator. I took part in optical characterization of these components as well as fabrication of photonic crystals using electron-beam lithography. At that point, I was also involved in the joint activities with Aalborg University participating in fabrication of corrugated metal surfaces supporting surface plasmon polariton propagation. Eventually, the interesting and attractive physics of these surface waves turned surface plasmon polaritons into the highway of my project. As a result, this thesis is mainly about experimental investigation of long-range surface plasmon polaritons (LR-SPPs). However, a small part of the earlier work is included as appendices for those interested in electron-beam lithography and photonic-crystal fabrication[1].

The last half of my Ph.D. study, I worked together with the start-up company MMP A/S, and the thesis follows (more or less) the historical development of this research project. It started with investigation of LR-SPP stripe waveguides and waveguide components in the light of future

[1] For all figures in the thesis, if not stated otherwise, scanning electron microscopy and electron-beam lithography were performed at the Niels Bohr Institute (University of Copenhagen).

applications for integrated optical circuits. Photonic-crystals-related activities ran in parallel with "stripe"-research, aiming at the "ground-breaking applications in optical networking" (quoted from the MMP A/S website). On the way to extreme miniaturization, many obstacles were encountered. However, different solutions were found enabling a range of useful, and sometimes unexpected, applications. In the thesis, following the historical development, LR-SPP Bragg gratings (1D photonic crystals) appear after the general chapter on photonic crystals and detailed study of 2D periodic structures. The reason for this is not only chronological. Stripe-waveguide components are followed by 2D photonic crystals that can, in principle, provide a scaled-down version of all these components, while Bragg gratings are considered as a possible solution for realization of one particular type of devices, namely, integrated optical filters.

List of Acronyms

1D, 2D, 3D – one-, two-, three-dimensional

AFM – atomic force microscopy

ATIR – attenuated total internal reflection

BCB – Benzocyclobutene (polymer)

COM – Research Center COM

DFB – distributed feedback

EBL – electron-beam lithography

EM – electro-magnetic

FWHM – full width at half-maximum

LR-SPP – long-range surface plasmon polariton

MFD – mode field diameter

MMI – multi-mode interferometer

MMP – Micro Managed Photons A/S

OSA – optical spectrum analyzer

PBG – photonic band gap

PC – photonic crystal

PICCO – Photonic Integrated Circuits using Photonic Crystal Optics (European IST project)

PM – polarization maintaining

RIE – reactive ion etching

SEM – scanning electron microscopy

SMF – single mode fiber

SOI – silicon-on-insulator

SP – surface plasmon

SPP – surface plasmon polariton

SPPBG – surface plasmon polariton band gap

TE – transverse electric

TM – transverse magnetic

UV – ultraviolet

1 Introduction

Well begun is half done.
Aristotle

Integrated optical circuits have been intensively developing over the last 30 years with the purpose of reducing the number of electronic-optic interconnections and realizing various functionalities such as routing, splitting, combining, and filtering of optical signals. Currently, several integrated optical technologies are developed with different technological platforms and material systems including III-V semiconductors, silica, silica-on-silicon, and silicon oxynitride with processing based on standard photolithography [1-3], lithium niobate crystals modified with the titanium diffusion [4], as well as technologies based on sol-gel [5], polymers [6], and organo-mineral materials [7]. All existing technologies have their advantages and drawbacks but all have proven to be of preference for different applications. One of the most important characteristics of a technology is its price. Today, low-cost processes are thought to become the winners of the future-integrated-optic-technology competition. In order for integrated optical components to be compact and low-cost, it is highly desirable that they are fabricated on a planar surface. A new approach, which suggests to employ long-range surface plasmon polaritons (LR-SPPs) for guiding of light along thin metal stripes embedded in a dielectric, e.g., a polymer, meets the requirements of low-cost, simplicity of planar fabrication, combined with flexibility and good performance.

Surface plasmon polaritons (SPPs) that represent quasi-two-dimensional electromagnetic excitations propagating along a dielectric-metal interface and having the field components decaying exponentially into both neighboring media [8], are of great interest to a wide range of researches and have been extensively studied by physicists, biologists, and chemists. SPPs first generated a lot of interest in condensed-matter physics followed by the increasing share of the optics community that comes from the recent progress in fabrication of nano-structured metal surfaces, which allows to tailor the properties of the SPPs [9].

The possibility of using SPPs for miniature photonic circuits has attracted a great deal of attention to the field of SPPs during the last years [9]. For example, efficient SPP excitation with subsequent coupling to and guiding along narrow metal stripes has been successfully demonstrated [10-12]. Due to the relatively small propagation length (~ 30 μm in visible and ~ 300 μm in the near-infrared wavelength range for a silver-air interface [8]) SPPs are considered being somewhat

limited in their applications. Furthermore, since SPPs are tightly bound to the metal surface (penetrating ~ 100 nm in dielectric and ~ 10 nm in metal), the conventional "end-fire" coupling of radiation with single-mode fibers cannot be directly applied.

However, the SPP propagation characteristics change drastically when a metal/dielectric interface is replaced by a symmetrical structure of a thin metal film embedded in dielectric. Such a symmetrical structure supports propagation of the *long-range SPP (LR-SPP)*, which is a symmetrical mode formed by two coupled SPPs associated with the two (upper and lower) metal-dielectric interfaces [13]. The main advantage of using a long-range SPP (LR-SPP) is *low propagation loss* (down to a few dB/cm [13,14]). Furthermore, field distribution of an LR-SPP mode, propagating along thin metal stripe, can be matched to that of a single-mode fiber facilitating the *efficient "end-fire" excitation* [14-16].

Combined with relatively easy fabrication, guiding of light via excitation of LR-SPPs has attracted considerable attention over the last years [15-17]. Quite recently, efficient LR-SPP excitation and guiding along 10-nm-thin gold stripes embedded in polymer was realized demonstrating a coupling loss of ~ 0.5 dB and propagation loss of ~ 6-8 dB/cm at ~ 1550 nm [16].

Once low-loss LR-SPP-supporting waveguides have been demonstrated, bends, splitters and other waveguide components based on metal stripes are to be investigated. Bends, which are used for connecting waveguides offset with respect to each other, are very important in integrated optical circuits, because it is often required to properly adjust the separation between adjacent input/output waveguides with respect to that between in/out-coupled (pigtailed) fibers. Over the years, wave propagation in bent waveguides has been studied extensively both theoretically and experimentally for different bend types and different bend performances (including the smallest bend radius and bend loss) have been reported [18-20]. In integrated optical circuits, bends are usually included as parts of larger basic building blocks, such as Y-splitters and directional couplers. These components have generated a lot of interest due to their numerous applications for switching, modulation, wavelength demultiplexing, and power splitting [21]. In recent years, there has also been a growing interest in multimode interference (MMI) waveguide components that offer flexible and reconfigurable functionality used for signal routing and coupling devices [22]. Optical devices based on MMI effects are incorporated in modern phase diversity networks, Mach-Zehnder switches and modulators, balanced coherent receivers, ring lasers and other integrated optical circuits and components.

In order to integrate many functional elements onto one chip, the individual components of the integrated optical circuit should be reduced in size that would also ease the fabrication yield and reduce the cost. On the way to miniaturization of integrated optical components, the SPP related research shifted markedly toward exploring the possibilities for SPP manipulation with artificially created surface structures [9]. Investigations of local excitation [23,24] and manipulation [25-30] of SPPs showed fascinating possibilities for controlling the SPP propagation in the surface plane

with metal nanostructures. Recently, SPP guiding along straight and sharply bent narrow channels in periodically corrugated regions has been realized [31-33]. The underlying physics is similar to that of light propagation in *photonic crystals (PCs)* (or photonic band gap (PBG) structures) [34]. It is based on the inhibition of SPP propagation in the periodic structure within a certain wavelength interval. The band gap for SPPs (SPPBG) was first observed by performing angular and wavelength resolved measurements of the reflectivity of periodically corrugated films (in one [35] and two [36] dimensions). Experimental investigations of the SPPBG structures [31-33] stimulated theoretical considerations of the SPPBG effect [37] and the corresponding waveguiding characteristics [38-40] that corroborated the feasibility of efficient SPP manipulation using periodic arrays of surface scatterers.

It seems natural to try to realize the photonic crystals for LR-SPPs and utilize the PBG concept for miniaturization of guiding structures by adapting the ideas developed for SPPs [24,26,30,31]. In addition to 2D photonic structures, 1D periodic structures, namely *Bragg gratings*, are also considered for realization of LR-SPP-based wavelength selective components. Given the advantage of the low propagation and coupling losses attainable with LR-SPPs, efficient control of the LR-SPP propagation in the surface plane may lead to new possibilities for photonic applications of LR-SPPs.

The thesis consists of seven chapters, including the introduction. The chapters are organized as follows. *Chapter two* introduces the concept of surface plasmon polaritons describing their fundamental properties as well as different methods of SPPs excitation. In the section devoted to applications of surface plasmon polaritons, long-range surface plasmon polaritons are introduced from the perspective of future applications in integrated optics.

In *chapter three* properties of long-range surface plasmon polaritons propagating along thin metal films and finite-width stripes are studied. First, an infinitely wide metal film bounded by two dielectric media is considered, and the propagation loss is calculated for different thicknesses of metal film and different properties of the dielectric media. In the second step, a thin metal stripe of a finite width embedded in dielectric material is analyzed using the effective-refractive-index method, and the dependencies of the propagation loss and lateral mode profile on the stripe width are obtained. The LR-SPP mode profiles are also studied for different configurations.

Chapter four describes the experimental results for optical characterization of fabricated LR-SPP stripe waveguides and waveguide components at telecommunication wavelengths. Experimental results for the propagation loss and mode profiles are reported and compared with the calculated values. LR-SPP-supporting bends and splitters as well as multi-mode interference devices are also described. Reported here are also coupling lengths for directional couplers with different parameters that are compared with the values obtained from the effective-refractive-index approach.

In *chapter five* the general concept of photonic crystals and its implementation for guiding of long-range surface plasmon polaritons are presented. The chapter concerns the design, fabrication and optical characterization of the LR-SPP guiding in 2D periodic structures, performed at telecommunication wavelengths. Experimental investigations of the LR-SPP transmission through and reflection from the PC structures of different lengths, lattice periods and orientations as well as the LR-SPP guiding along line defects in these structures are reported.

Chapter six is devoted to integrated Bragg gratings and intended to provide a basic Bragg grating theory as well as summary of experimental results obtained for Bragg gratings for long-range surface plasmon polaritons. The experimental findings for LR-SPP ridge Bragg gratings are reported, including transmission and reflection spectra. The effective refractive index modulation is estimated using simple description of a lossless Bragg grating. The Bragg grating filter bandwidth as well as the grating strength is also estimated for different grating parameters. The realization of a compact wavelength add-drop filter with a bandwidth of ~ 20 nm centered at 1550 nm is reported at the end of the chapter.

The thesis is concluded in *chapter seven* where summary and conclusions are presented and future directions of the LR-SPP-related research as well as possible applications of LR-SPPs are discussed.

2 From Surface Plasmon Polaritons to Integrated Optics

I am among those who think that science has a great beauty.
A scientist in his laboratory is not a mere technician:
he is also a child confronting natural phenomena
that impress him as though they were fairy-tales.
Marie Sklodowska-Curie

This chapter gives an introduction to the concept of surface plasmon polaritons. The chapter starts with a short section devoted to the simple model for describing optical properties of metals developed by Drude. After that, the terms *plasma* and *plasmons* are introduced for bulk metals. In the next section, plasmons transform into *surface plasmon polaritons* followed by the description of the fundamental properties of these surface waves. Thereafter, different methods of excitation of surface plasmon polaritons are described. The last section is devoted to numerous applications of surface plasmon polaritons. Included here is an introduction (from the perspective of future applications in integrated optics) to the main subject of this work – a special subset of surface plasmon polaritons, namely, *long-range surface plasmon polaritons* that are treated in the next chapter.

2.1 Optical properties of metals: The Drude model

In order to understand optical properties of metals in detail, complicated quantum-mechanical treatment is required. However, a classical model for metals, developed by Drude in 1900 [41], successfully describes many properties of metals and is sufficient in the present context.

The Drude model (the so called *free-electron model*) is based on the kinetic gas theory. It assumes a gas of non-interacting free electrons that have an isotropic effective mass and relaxation time. This means that electrons move freely between independent collisions and the average rate of these collisions γ is connected to the average relaxation time τ, with $\gamma = 1/\tau$. In an external electric field, the electrons obey Newton's law of motion and are accelerated between collisions, and this leads to a drift motion.

The resulting equation of the Drude model predicts quite well the behavior of the frequency dependent dielectric function $\varepsilon(\omega)$ of a metal [42]:

$$\varepsilon(\omega) = 1 - \frac{\omega_p^2}{\omega^2 + i\omega\gamma} = \varepsilon_R(\omega) + i\varepsilon_I(\omega) \quad [2.1]$$

$$\varepsilon_R(\omega) = 1 - \frac{\omega_p^2\tau^2}{1+\omega^2\tau^2}, \varepsilon_I(\omega) = \frac{\omega_p^2\tau}{\omega\left(1+\omega^2\tau^2\right)} \quad [2.2]$$

$$\omega_p^2 = \frac{ne^2}{\varepsilon_0 m} \quad [2.3]$$

where ε_R and ε_I are the real and imaginary part of the dielectric constant, respectively, and ω_p is the plasma frequency (or plasma resonance frequency), determined by the electron density, n, charge, e, and mass[2], m. The relaxation time can be related to the conductivity by the expression [43]:

$$\sigma = \tau\frac{ne^2}{m} \quad [2.4]$$

In the Drude model, the dielectric function of a metal is defined only by the plasma frequency and the electron collision rate. Typically, the plasma frequency ω_p lies in the UV region. For example, the plasma frequency corresponds to a wavelength of approximately 260 nm for silver and to ~ 230 nm for gold (for an electron density $n \sim 10^{22}$ cm^{-3}). The collision rate can be quite rapid so that the time interval between two collisions is tens of femtoseconds. If for some frequency range, $(\omega\tau)^2 >> 1$ (for example, for optical frequencies – $\omega = 3\cdot10^{-15}$ s^{-1} corresponding to $\lambda = 633$nm), the following approximation can be used [42]:

$$\varepsilon(\omega) \approx 1 - \frac{\omega_p^2}{\omega^2} \quad [2.5]$$

This means that above the plasma frequency, the metal becomes effectively transparent ($\varepsilon \to 1$) while below ω_p all incident radiation is reflected ($\varepsilon < 0$).

Let's briefly consider propagation of electromagnetic wave in metals at frequencies below ω_p. From the wave equation $\Delta E - \left(\varepsilon(\omega)/c^2\right)\left(\partial^2 E/\partial t^2\right) = 0$ the wave vector of the propagating electromagnetic wave $E(\vec{r},t) = E\exp\left(i\vec{k}\cdot\vec{r} - i\omega t\right)$ can be expressed as

$$\left|\vec{k}\right|^2 = k^2 = \varepsilon(\omega)\frac{\omega^2}{c^2} \quad [2.6]$$

[2] In a modified version of the Drude model an effective electron mass m is different from the free-electron mass m_0 due to the correction to the quadratic dispersion relation of a free electron originating from the Pauli-exclusion principle.

For frequencies ω smaller than the plasma frequency ω_p, $\varepsilon(\omega)$ is negative meaning that k is purely imaginary[3]. This leads to the exponential decay of the electromagnetic field into the metal $E(x) = E\exp(-|k|x)$ that implies that the light penetrates into the metal only to the skin depth [8,42].

As a classical model, the Drude model has some limitations. Assuming that in a metal the valence electrons can move freely and independently, one gets to the conclusion that all metals are transparent for frequencies $\omega > \omega_p$ and reflect all incident radiation $\omega < \omega_p$, which can not, for example, explain different colors of metals – the yellow tint of gold or reddish color of copper. The reason is that, in reality, the electronic band structure cannot be neglected. That is why the classical Drude model may not be valid at high frequencies, when additional effects such as interband transitions arise. Nevertheless, for many metals at optical frequencies the Drude model generally provides a good agreement with experimental observations.

2.2 Introduction to surface plasmon polaritons

"You know I always thought unicorns were fabulous creatures too,
although I never saw one alive before." "Well, now that we have met,"
said the unicorn, "If you'll believe in me, I'll believe in you."
Lewis Carroll, "Through the Looking Glass"

Surface plasmon polaritons were recognized by the scientific community in 1957 [44], when it was shown that these excitations appeared as a solution to Maxwell's equations under specific conditions. Today, these surface waves are of interest to a large variety of scientists including physicists, chemists, and biologists [8,9,45].

2.2.1 Bulk plasmons in metals

In the classical model of a metal, the positive ions are replaced by the uniform background medium with the positive density equal to the average density of all electrons but of the opposite sign. In this model all electrons can be described as a gas with fluctuating density. These density fluctuations may cause periodic Coulomb attraction or repulsion of electrons giving rise to the longitudinal collective oscillations of the electronic gas or *plasma oscillations*. A quantum of these oscillations is called a *plasmon* (or *bulk plasmon* since it exists in a bulk metal).

Just like in the Drude model, plasma oscillations in a metal can be described using a simple model where the displacement of the electron from its equilibrium position determines the induced polarization. The plasma frequency [2.3] represents the resonant frequency for bulk plasmons.

[3] Here, we do not consider the case of $\mu<0$ (left-handed materials).

2.2.2 Surface waves and some history

The interface between a metal and another medium may also support charge density oscillations. These electron movements form a time-dependent polarization and this leads to the creation of the electromagnetic (EM) field associated with the interface. The charge density oscillations and the EM field are coupled to each other and this coupled state is often called an *interface (or surface) polariton*[4].

Electromagnetic surface waves have a long history. Already in the beginning of the 20th century it was theoretically demonstrated (Zenneck, 1907 [46], Sommerfeld, 1909 [47]) that surface EM waves at radio frequencies occurred at the boundary of two media with inverse optical properties, i.e. the interface between a lossy dielectric, or a metal, and a lossless medium. It was suggested that it was the imaginary ("lossy") part of the dielectric function that was responsible for the trapping of the wave to the surface. But these early investigations were performed in connection with the wireless telegraphy and they dealt with frequencies much smaller than that of light in the optical regime. In that case, the behavior of surface waves is phenomenologically not much different from plane EM waves in free-space.

Half a century later, in 1957, the existence of surface plasma oscillations or *surface plasmon polaritons (SPPs)* that represented coherent fluctuations of the electron charges on a metal boundary was theoretically shown in the pioneering work by Ritchie [44]. Soon after that, the existence of the SPPs was experimentally demonstrated in electron energy-loss experiments by Powell and Swan [48]. The name *surface plasmon polariton*[5] reflects the fact that this type of waves is bound to the *surface* between two regions with different ("inverse") optical properties (dielectric-metal) and represents a coupled state between a *plasmon*, which is a quantum associated with longitudinal waves in the collective motion of electrons, and a free EM field, yielding a *polariton* type excitation.

The surface charge oscillations constitute a mixed transversal and longitudinal electromagnetic field in the two media, which disappears at infinity (for $|z| \rightarrow \infty$) and has its maximum at the interface ($z = 0$), which is typical for surface waves (Figure 2.1).

Due to boundary conditions, SPP modes are only possible for *p*-polarization of the light (TM modes) reflecting the fact that these modes are transverse magnetic in nature, and the surface charge is produced by the electric field normal to the surface. This combined nature leads to the

[4] The term *interface (or surface) polariton* is normally used for coupled mechanical-electromagnetic excitations at the interface corresponding to any kind of excitation inside the solid (e.g. phonon-polariton, plasmon-polariton, magnon-polariton).

[5] In literature surface plasmon polaritons are sometimes called just *surface plasmons*. Strictly speaking, the term *surface plasmon is* slightly non-physical since it reflects only existence of the electron density oscillations as if they occur without coupling with the EM field.

situation where the field component perpendicular to the surface is enhanced near the surface and decays exponentially away from the interface. TE modes (or *s*-polarized modes) do not satisfy the boundary conditions, which can be explained by simple considerations – *s*-polarized surface oscillations cannot exist because the electric field is continuous along the boundary and thus no surface charge is produced.

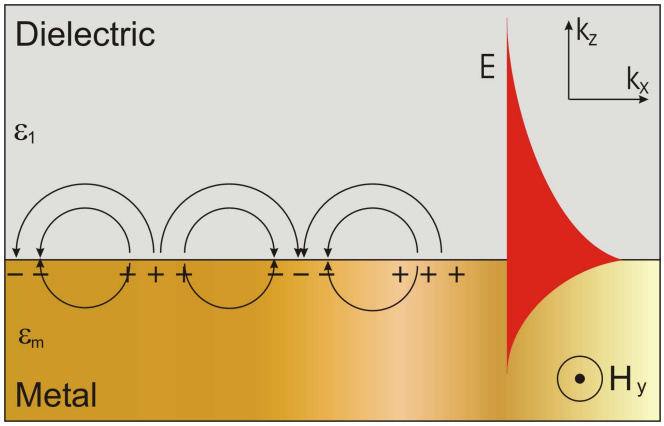

Figure 2.1 Schematic of the charges and the electromagnetic field of surface plasmon polariton propagating along a metal-dielectric interface in the **x** direction together with the exponential dependence of the field, **E**, in the **z** direction. The magnetic field, $\mathbf{H_y}$, is perpendicular to the plane of incidence (**y** direction) while the electric field, **E**, is kept within the plane incidence (**x,z**).

2.2.3 Dispersion relation

A theoretical description of SPPs has to include the interaction between the charge oscillations and the EM field. Boundary conditions at the interface lead to a difference between the frequency of the surface charge oscillations and that of the bulk plasmon oscillations. The main properties of SPPs can be obtained from simple electrodynamics theory, when Maxwell equations are applied to an ideal interface. The simplified derivation of the dispersion relation for SPPs can be found, for example, in reference [8].

The *dispersion relation* for the plane surface of a semi-infinite metal with the dielectric function $\varepsilon_m = \varepsilon_R + i\varepsilon_I$, adjacent to a medium ε_1 (typically air), relates the SPP wave vector k_x (which is continuous along the interface) to the frequency ω [8,49]:

$$k_x = \frac{\omega}{c}\sqrt{\frac{\varepsilon_1 \varepsilon_m}{\varepsilon_1 + \varepsilon_m}} > k_0 = \frac{\omega}{c}\sqrt{\varepsilon_1} \qquad [2.7]$$

where k_0 is a free space wave vector. The dispersion relation for the propagation constant β is written as:

$$\beta = \frac{2\pi}{\lambda_0}\sqrt{\frac{\varepsilon_1 \varepsilon_m}{\varepsilon_1 + \varepsilon_m}} \qquad [2.8]$$

where λ_0 is the wavelength of the light in vacuum.

Under the assumption that besides real ω and ε_1, $\varepsilon_I < |\varepsilon_R|$ one can obtain a complex wave vector $k_x = k_{xR} + ik_{xI}$ where

$$k_{xR} = \frac{\omega}{c}\sqrt{\frac{\varepsilon_R \varepsilon_1}{\varepsilon_R + \varepsilon_1}} \qquad [2.9]$$

$$k_{xI} = \frac{\omega}{c}\left(\frac{\varepsilon_R \varepsilon_1}{\varepsilon_R + \varepsilon_1}\right)^{3/2}\left(\frac{\varepsilon_I}{2(\varepsilon_R)^2}\right) \qquad [2.10]$$

In order to have a finite k_{xR}, the conditions $\varepsilon_R < 0$ and $|\varepsilon_R| > \varepsilon_1$ have to be fulfilled, which can be achieved in a metal or highly doped semiconductor [8]. In the visible and infrared region, many metals exhibit a negative dielectric function, including gold, silver, aluminum, and copper. The value of k_{xI} determines the internal absorption and will be discussed below. In the following k_x will be used in general instead of k_{xR}. One can also write an expression for the SPP wavelength:

$$\lambda_{SPP} = \frac{2\pi}{\mathrm{Re}\,\beta} = \lambda_0\sqrt{\frac{\varepsilon_R + \varepsilon_1}{\varepsilon_1 \varepsilon_R}} < \lambda_0 \qquad [2.11]$$

The graphical representation of the dispersion relation for SPPs is shown in Figure 2.2.

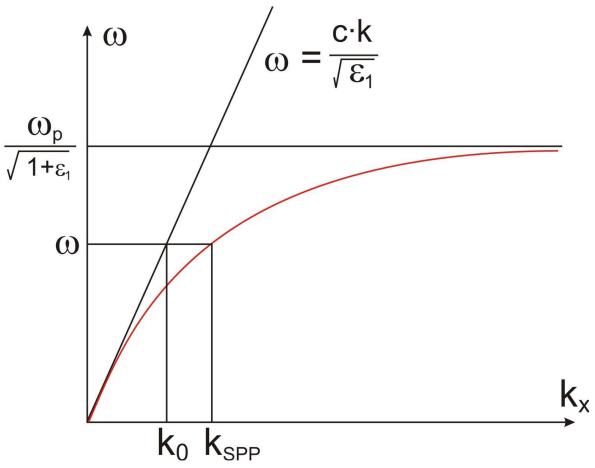

Figure 2.2 The dispersion relation of surface plasmon polaritons. Note that the plasmon curve lies to the right of the photon line (light line) – the SPP mode has greater momentum ($\mathbf{k_{SPP}}$) than a free space light ($\mathbf{k_0}$) at the same frequency $\boldsymbol{\omega}$.

The surface plasmon curve lies to the right of the light line (Eq. [2.7]), which can be explained in simple words using an analogy with particles and their momenta – since a SPP represents a coupled state between electron oscillations and the EM field, one can say that the light is, in a way, trapped to the electron oscillations and hence "heavier" than the free light. As an example, the SPP wave vector for a silver-air interface in the red part of the visible spectrum is found to be $k_x \approx 1.03 \cdot k_0$.

The dispersion relation approaches the light line at small k_x but still remains larger, which means that SPPs cannot spontaneously transform into light: they are called *non-radiative* SPP. At larger k_x or $\varepsilon_R \to -\varepsilon_1$ the value of ω approaches (Eq. [2.5]):

$$\omega = \sqrt{\frac{\omega_p}{1+\varepsilon_1}} \qquad [2.12]$$

which gets smaller with increasing ε_1.

At large k_x the group velocity and the phase velocity goes to zero, so that the SPP resembles localized fluctuations of the electron plasma [8].

2.2.4 Spatial extension of the surface plasmon polariton fields

The wave vector component k_z can be expressed as [8]:

$$k_{zi} = \sqrt{\varepsilon_i \left(\frac{\omega}{c}\right)^2 - k_x^2}, i = 1, m \qquad [2.13]$$

Due to the relations $k_x > \left(\omega\sqrt{\varepsilon_1}\right)/c$ and $\varepsilon_R < 0$, the wave vector components k_{z1} and k_{zm} are purely imaginary so that, as mentioned above, the field amplitude of the SPPs decreases exponentially as $\exp(-|k_z||z|)$ in the direction perpendicular to the surface (Figure 2.3). This reflects the "trapped", non-radiative nature of SPPs, where light does not propagate away from the surface.

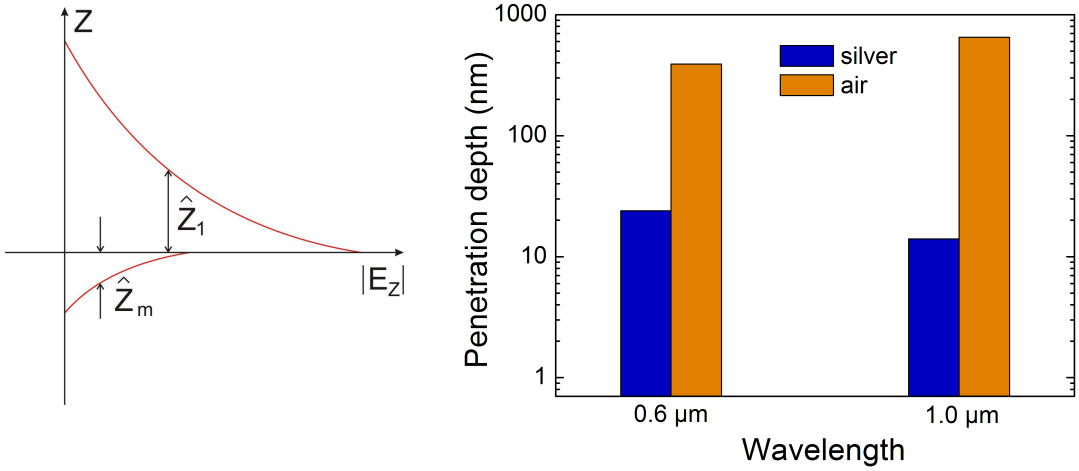

Figure 2.3 (Left) Surface plasmon polariton field perpendicular to the surface and **(right)** comparison of the decay lengths in the dielectric ($\mathbf{z_1}$) and in the metal ($\mathbf{z_m}$) for a silver-air interface at two wavelengths.

The value of the penetration (decay length) is determined as the distance at which the field falls to 1/e:

$$\hat{z} = \frac{1}{|k_z|} \qquad [2.14]$$

This yields a decay length in the dielectric medium with ε_1 equal to $\hat{z}_1 = (\lambda/2\pi)\sqrt{(\varepsilon_R + \varepsilon_1)/\varepsilon_1^2}$, which is (for dielectric medium such as glass or air) typically on the order of half of the wavelength involved. The skin depth in the medium ε_m (typically metal) is smaller and is given by $\hat{z}_m = (\lambda/2\pi)\sqrt{(\varepsilon_R + \varepsilon_1)/\varepsilon_R^2}$. For example, for a silver-air (ε_1=1) interface at a wavelength of 600 nm the field penetrates approximately 24 nm into the metal and about 390 nm into the air ($\varepsilon_R = -16$), while for a gold-air interface ($\varepsilon_R = -8.5$) the field penetrates approximately 31 nm into the metal and 280 nm into the air. At the wavelength of 1 μm, for silver ($\varepsilon_R = -48$) these values are on the order of 650 nm and 14 nm, respectively (Figure 2.3).

At low k_x or very large $|\varepsilon_R|$ values, the field has a strong transverse component E_z compared to the longitudinal component E_x and the field extends far into the air – in this case these surface waves resemble the ones earlier discovered by Zenneck and Sommerfeld. In the metal, E_z is smaller than E_x. At large k_x, when both components E_x and E_z become equal, $\hat{z}$ is primarily determined by $1/k_x$ and gives a strong confinement of the field to the surface in both media [8].

2.2.5 Propagation length of surface plasmon polaritons

Since the wave vector k_x is complex, it has two components along the x direction – one is that of a traveling wave while the second is a damping term, which means that along the interface the intensity of SPPs decreases as $\exp(-2k_{xI}x)$. One can define a propagation length L after which the intensity decreases to 1/e. The propagation length is then determined by k_{xI} (Eq. [2.10]) and given by:

$$L = \frac{1}{2k_{xI}} \qquad [2.15]$$

Due to the wavelength dependence of k_{xI} [2.10] and ε_I [2.2], the propagation length depends on the frequency of the SPP mode and the plasma frequency of the metal. It is the imaginary part of the dielectric constant of metal that primarily determines how far the SPP will propagate. In order to have large propagation lengths, ε_I should be as small as possible. That's why silver and gold, that have high conductivity (see [2.2] and [2.4]), are considered to be the best candidates when making SPP-supporting interfaces at optical frequencies. For example, the propagation length for the silver-air interface increases from approximately 22 μm at the wavelength of 633 nm to ~ 500 μm and ~ 800 μm at 1.0 μm and 1.55 μm respectively ($\varepsilon_I \sim 3$ for silver at 1550 nm [50]) (Figure 2.4).

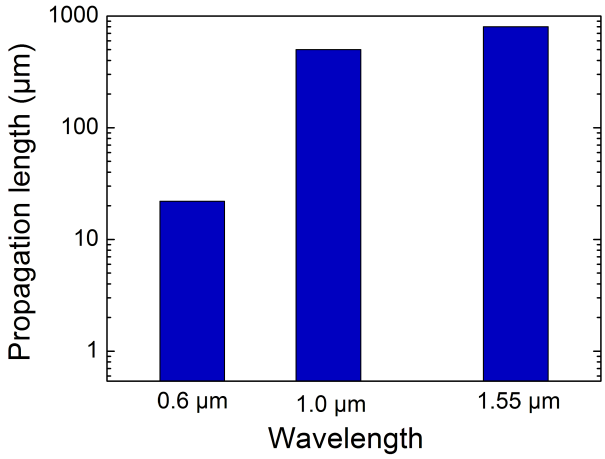

Figure 2.4 The surface plasmon polariton propagation length for a silver-air interface for three different wavelengths.

2.3 Methods of excitation of surface plasmon polaritons

There are several ways of exciting surface plasmon polaritons propagating along a metal-dielectric interface. The two methods that have been used most extensively are excitation by electrons and by light.

When SPPs are excited by an *electron* beam, electrons penetrating the metal transfer momentum and energy to the electrons of the metal. Since the incident electrons are scattered at different angles, they deliver different momenta, which makes it possible to study the dispersion relation for SPPs in a wide range of wave vectors k_x. An overview of this type of SPP excitation as well as a description of how to study physical SPP properties using electrons can be found, for example, in [8].

The excitation *by light* meets a difficulty – surface plasmon polaritons cannot be coupled directly from the free-space electromagnetic radiation of the same energy because SPPs travel too slowly. As was mentioned above, their associated wave vector is too large to satisfy conservation of energy and momentum (Figure 2.2). Three main techniques are used to provide the missing momentum: *Attenuated (or frustrated) total internal reflection* (ATIR) (also called *prism coupling*) [49,51,52], *grating coupling* [8,49], and scattering from a topological defect [23].

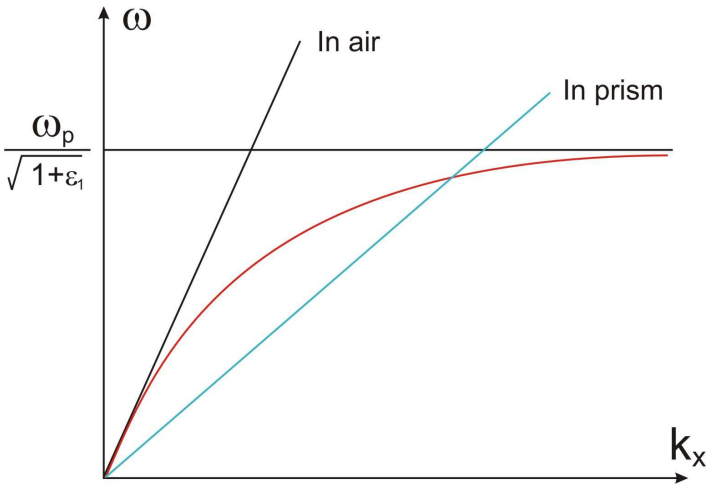

Figure 2.5 Schematic of the dispersion relations involved in the prism coupling method: Surface plasmon polariton on the metal-air interface **(red)** together with the light lines in air **(black)** and in the dielectric prism **(blue)** demonstrating the possibility of SPP excitation using prism coupling.

The ATIR technique is the most popular method of SPP excitation [8]. In this configuration, the incident EM radiation is passed through an optically dense medium, which increases its wave vector (Figure 2.5). In practice the configuration is quite simple and requires only adapting the optically dense dielectric medium (typically a prism made of a material with a dielectric constant ε_3 >0) to the metal-dielectric interface. The incident beam traveling through the prism then reflects from the boundary between the optically dense medium and either a less dense dielectric medium (Otto configuration [52]) or the metallic layer (Kretschmann-Raether configuration [51]) (Figure 2.6). An evanescent field extends from this interface and "drives" the electrons on the metal-dielectric interface producing a surface plasmon polariton. In the ATIR technique, the SPP excitation is recognized as a minimum in the totally reflected intensity (ATIR minimum) [8].

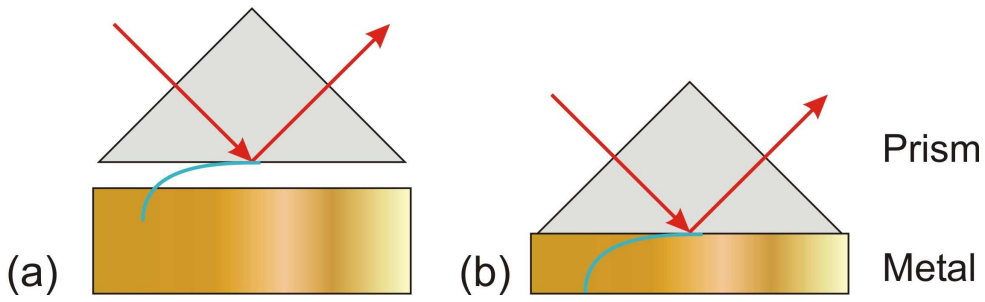

Figure 2.6 Schematics of the attenuated total internal reflection (ATIR) method of excitation of surface plasmon polaritons in **(a)** Otto and **(b)** Kretschmann-Raether configurations.

The ATIR method in the Otto configuration, when a dielectric (typically air) lies between the prism and the metal surface, is mostly used for surfaces that should not be damaged or touched by

the prism, for example, for studying single crystal metal surfaces. Practically, it is a quite difficult technique since the metal has to be placed within 200 nm from the prism surface so that the decaying evanescent wave can still excite the SPPs on the metal-air interface. In case of the Kretschmann-Raether configuration, the metal is in contact with the prism, which can be achieved by depositing metal directly on the prism or by means of immersion techniques. The requirement here is that the thickness of the metal should not be too large (for example, 40-50-nm-thick gold film is used for λ = 633 nm) if a plasmon should be excited on the metal-air interface.

A *grating coupler* can also be used for SPP excitation [8]. In this technique the incident EM radiation is directed towards a surface with a spatial periodicity, Λ, similar to the wavelength of the radiation (for example, a reflection diffraction grating). The incident beam is diffracted producing propagating modes traveling away from the interface and evanescent modes that exist only at the interface. These evanescent modes have wave vectors parallel to the interface and equal to the corresponding component of the incident radiation but with the integer of the grating vector added or subtracted from it. Thus, grating couplers provide a way of increasing the wave vector of the light to be momentum matched so that it can couple to SPPs, which run along the interface between the grating and the surrounding medium. The resonance is again observed as a minimum of the reflected light [8].

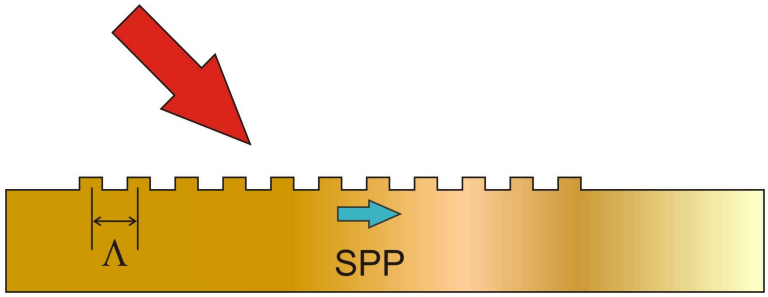

Figure 2.7 Schematic of a grating coupler for the excitation of surface plasmon polaritons.

Similarly, SPPs propagating along a grating or rough surface can reduce their wave vector and be transformed into light. SPP-photon coupling via roughness [8], allows the SPP mode to couple with light in a controlled way providing an important feature that can be used in future SPP-based photonic circuits [53].

Yet another way of coupling photons to SPPs is to use scattering from a topological defect on the surface, such as a subwavelength hole or protrusion [23]. This method is often used for exciting localized surface plasmons. SPP investigations in the terahertz frequency range have utilized the aperture coupling technique [54].

2.4 Applications of surface plasmon polaritons

I am enough of an artist to draw freely upon my imagination.
Imagination is more important than knowledge.
Knowledge is limited. Imagination encircles the world.
Albert Einstein

Two main features of surface plasmon polaritons can be exploited in many ways namely the *surface field enhancement* at the resonance excitation and the *sensitivity* of the resonance angle to the surface properties. Many fundamental properties of SPP's have been studied and a lot of applications have been suggested including subwavelength optics [9,55], photonic (plasmonic) integrated circuits [11,12,25,30,31], biological and chemical sensing [56], nano-lithography [57], magneto-optic data storage [58], solar cells [59], as well as light generation and microscopy [60,61].

The fact that the SPP field components decay exponentially away from the interface and show rather tight field intensity confinement to the metal surface (typically on the order of or smaller than the wavelength in the corresponding media) makes SPPs very sensitive to surface irregularities. The SPP has therefore been considered as a tool for surface sensing and analysis [8] and has been exploited for many years. In the ATIR configuration, the SPP resonance position (ATIR minimum) is extremely sensitive to the interface structure. An adsorption process, for example, leads to a shift in the SPP resonance and allows the mass coverage at the surface to be monitored with high accuracy. The main advantage of this technique is the localization of the field at the interface so that the device is less sensitive to structural changes in the bulk phase. On the other hand, the extreme surface sensitivity can also be very hard to work with since even slight defects or dirt on the surface will cause a SPP resonance shift. The SPPs can also be used to monitor biological interactions. The excitation of the SPPs between chemically modified thin metal film surface and a solution can be used to probe the interactions between substances, attached to the metal surface, and biological molecules (enzymes, proteins) in the solution [45].

In the field of optics, one of the most attractive features of SPPs is the possibility to localize and guide light using subwavelength-sized structures. Many interesting findings and possible applications of SPPs in this direction have been reported by many groups [9-12,23,26,31-33]. Recent progress in the fabrication of nano-structured surfaces has paved the way for exploitation of SPPs for radiation guiding along straight and sharply bent channels in (periodically) corrugated regions [11,31,33] and along narrow metal stripes [10-12], which could become building blocks for future photonic circuits.

Even though straight and bent waveguides have been realized in many different material systems, there is one unique and attractive feature about SPPs: They use metal as a waveguiding medium, which means that such metallic waveguides can carry radiation and electrical signal at the same time. This may lead to a completely new area of photonics [9] including such applications as signal switching and sensing.

The surface field enhancement specific to surface plasmon polaritons has generated a lot of interest within condensed-matter physics due to possibility of increasing nonlinearities and investigating light-matter interactions. This light concentration becomes even more attractive when dealing with very small (subwavelength) metallic structures, supporting localized surface plasmons. Localized surface plasmons provide giant local (electric) field enhancement that can be used, for example, in surface-enhanced Raman spectroscopy for single molecule detection [62].

Photonic applications of SPPs are still considered to be somewhat limited due to their small propagation length (they are even known as *lossy 2D waves*) and non-compatibility with standard fiber optics. However, the interesting nature of surface plasmon polaritons has not exhausted all it's possibilities – SPPs become more attractive for photonic applications when the metal film in question is sandwiched between identical dielectric layers (Figure 2.8).

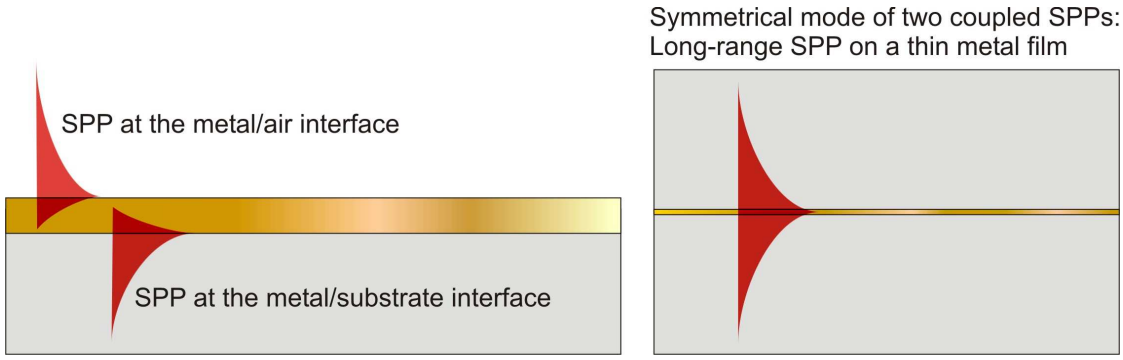

Figure 2.8 Schematic of long-range surface plasmon polariton formation.

In a symmetrical structure, two identical SPPs associated with the two (upper and lower) metal-dielectric interfaces become coupled, forming two modes: symmetrical and asymmetrical (with respect to the orientation of the main electric field component). It is the symmetrical mode that is of great interest and importance from a potential applications point of view of for two reasons. First, the attenuation of the symmetrical mode, also called the *long-range SPP (LR-SPP)* mode, decreases drastically with the decrease of the film thickness leading to an increase in the propagation length [13]. At the same time, for sufficiently thin metal films, the LR-SPP field components can extend several micrometers into the cladding via two identical evanescent tails facilitating the optical excitation, because the mode size is now close to that of the standard single-mode fiber (Figure 2.9). The existence of a long-range surface plasmon-polariton mode, which

could be excited on a thin metal film, was for the first time theoretically demonstrated by Sarid [13]. Since then, LR-SPPs have been studied both theoretically [14,17,63,64] and experimentally [15,16] for different configurations of metal-dielectric structures.

The "end-fire" excitation of LR-SPPs was first proposed by Burke et al. [14] and realized by Charbonneau et al., who experimentally observed LR-SPP propagation along thin gold stripes of finite width embedded in silica glass [15]. Efficient LR-SPP excitation and guiding along 10-nm-thin gold stripes embedded in polymer was recently realized by Nikolajsen *et. al.* showing a coupling loss of ~ 0.5 dB and propagation loss of ~ 6-8 dB/cm at 1550 nm [16].

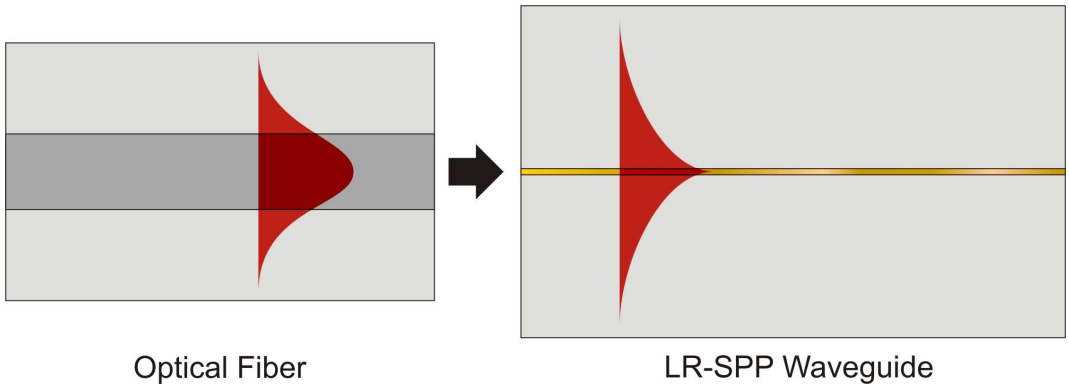

Figure 2.9 "End-fire" coupling technique for exciting long-range surface plasmon polaritons using standard optical fiber.

Figure 2.10 illustrates schematically the hierarchy of the integrated optical components that are discussed in this thesis. It begins with the simplest structure – the straight waveguide. Then, sharp and S-bends are introduced as basic building blocks for slightly more complicated devices: the Y-splitters and directional couplers that perform power splitting between two waveguides.

Multi-mode waveguides are also discussed in the light of multimode interference. Then straight waveguides and Y-splitters are introduced in photonic crystals (2D periodic structure) with the purpose of reducing the dimensions of these waveguide components. Thereafter, the simplest form of an integrated Bragg grating filter (1D periodic structure) is studied, where the filtered signal is reflected back into the input waveguide of the device. Finally, by combining two Bragg gratings and straight waveguides, it is possible to construct an integrated device, which separates the reflected signal from the incident signal – the simple version of the add-drop filter.

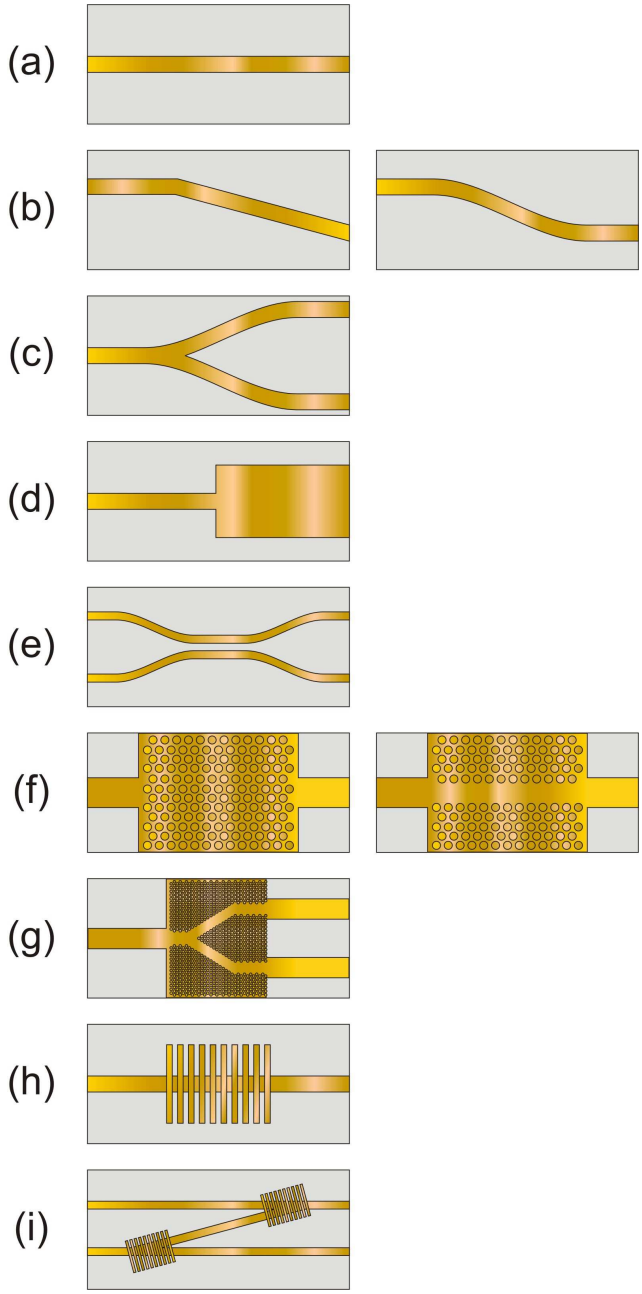

Figure 2.10 A hierarchy illustrating the types of devices that are considered in this work: **(a)** straight and **(b)** bent waveguide, **(c)** Y-splitter, **(d)** multimode waveguide, **(e)** directional coupler, **(f)** photonic crystal (PC) structure without and with linear defect, **(g)** PC-based Y-splitter, **(h)** Bragg grating and **(i)** add-drop filter composed of straight waveguides and Bragg gratings.

3 Long-Range Surface Plasmon Polaritons: Description and Modeling

The moment one gives close attention to anything,
even a blade of grass, it becomes a mysterious,
awesome, indescribably magnificent world in itself.
Henry Miller

In this chapter, properties of long-range surface plasmon polaritons propagating along thin metal films and finite-width stripes are studied. First, an *infinitely wide* metal film bounded by two dielectric media is considered. Using a one-dimensional mode solver, the propagation loss is calculated for different thicknesses of metal films and different properties of cladding layers (thickness, refractive index). The vertical mode profiles are studied for different metal films and cladding thicknesses for both symmetric and asymmetric configurations.

In the second step, a thin metal stripe of a *finite width* embedded in dielectric material is analyzed using the effective-refractive-index method. The dependencies of the propagation loss and lateral mode profile on the stripe width are obtained. Based on the effective-refractive-index approach, simple modeling of multi-mode interference waveguides and directional couplers is performed.

3.1 Long-range surface plasmon polaritons on thin metal films

3.1.1 Dispersion relations

Characteristics of SPP waves propagating along thin metal films embedded in a dielectric were first considered by Sarid who showed that the imaginary part of the propagation constant of the symmetrical mode, i.e., the LR-SPP mode, goes to zero as the metal film thickness decreases, implying the possibility of achieving very long propagation distances [13]. Properties of the LR-SPP mode supported by a thin metal film of infinite width can be analyzed by solving a dispersion

relation for confined electromagnetic waves. This relation can be obtained from the boundary condition for the tangential field components, which was reported by Burke *et. al.* [14].

The analyzed geometry is composed of a metal film of variable thickness t and dielectric constant $\varepsilon_m = \varepsilon_R + i\varepsilon_I$, which is bounded by two dielectric media with dielectric constants ε_1 and ε_3 so that $\varepsilon_1 \geq \varepsilon_3$ (Figure 3.1).

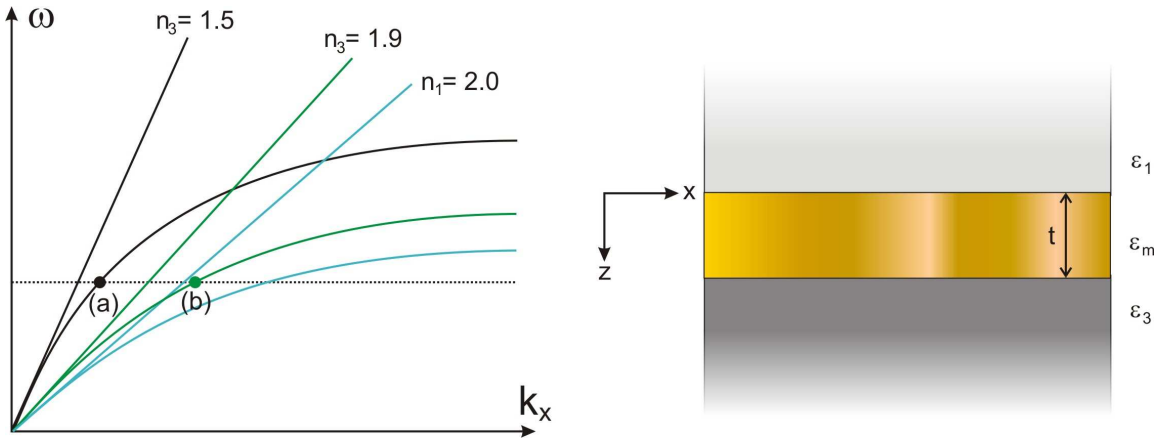

Figure 3.1 (Left) Dispersion curves for surface plasmon polaritons propagating along the ε_1 - ε_m and ε_3 - ε_m boundaries for the geometry shown on the **right** at t $\rightarrow \infty$. The points at the same frequency lie in the **(a)** leaky and **(b)** bound mode regions of the light line $n_1=(\varepsilon_1)^{1/2}=2.0$ [14].

Since surface plasmon-polariton waves are transverse magnetic in nature, they can be described by their magnetic fields parallel to the surface. When the wave is propagating along the x direction its magnetic field is given by

$$H = f(z)C\exp\left[i(\omega t - \beta x)\right] \qquad [3.1]$$

where $\beta = \beta_R - i\beta_I$ is the complex propagation constant parallel to the surface, $f(z)$ is the depth distribution of the magnetic field, and C is a normalization constant [14]. The electric field components can then be derived from Maxwell equations [14]:

$$E_x = \frac{i}{\sigma\varepsilon\varepsilon_0}\frac{\partial H_y}{\partial z}, E_z = -\frac{\beta}{\sigma\varepsilon\varepsilon_0}H_y \qquad [3.2]$$

The depth distributions can be written as [14]:

$$\varepsilon_1:\ f(z) = e^{S_1 z} \ \text{ for } z < 0 \qquad [3.3]$$

$$\varepsilon_m:\ f(z) = \cosh(S_m z) + \frac{S_1\varepsilon_m}{S_m\varepsilon_1}\sinh(S_m z) \ \text{ for } 0 > z > t \qquad [3.4]$$

$$\varepsilon_3:\ f(z) = \left(\cosh(S_m t) + \frac{S_1\varepsilon_m}{S_m\varepsilon_1}\sinh(S_m t)\right)e^{-S_3(z-t)} \ \text{ for } z > t \qquad [3.5]$$

where S_1, S_m, and S_3 are derived from the wave equations as

$$S_1^2 = \beta^2 - \varepsilon_1 k_0^2, S_m^2 = \beta^2 - \varepsilon_m k_0^2, S_3^2 = \beta^2 - \varepsilon_3 k_0^2 \qquad [3.6]$$

For non-radiative behavior $S^2 = \beta^2 - \varepsilon k_0^2$ is positive in both media, while in the case of a leaky (radiative) mode ($S^2 < 0$) S is imaginary and the field in that medium corresponds to a plane wave radiating away from the interface.

The equations for the fields (Eq. [3.3] - Eq. [3.5]) satisfy the condition that the tangential magnetic fields are continuous at $z = 0$ and $z = t$. From the continuity of the tangential electric field at $z = t$ one can derive the dispersion relation:

$$\tanh(S_m t)\left(\varepsilon_1 \varepsilon_3 S_m^2 + \varepsilon_m^2 S_1 S_3\right) + \left[S_m\left(\varepsilon_1 S_3 + \varepsilon_3 S_1\right)\varepsilon_m\right] = 0 \qquad [3.7]$$

The transcendental set of equations [3.6] and [3.7] can be solved numerically when dealing with a specific metal-dielectric configuration.

The solutions to the dispersion relation (Eq. [3.7]) are well known for thick metal films, when t is much larger than the skin depth ($\tanh(S_m t) \rightarrow 1$). They represent two SPPs propagating along the ε_1-ε_m and ε_m-ε_3 interfaces with dispersion relations similar to the one derived above (Eq. [2.7] and [2.8]). The dispersion curves for surface plasmon polaritons propagating along two interfaces are shown in Figure 3.1 for the refractive indices $n_1=(\varepsilon_1)^{1/2} = 2.0$, $n_3=(\varepsilon_3)^{1/2} = 1.9$ or 1.5 and $\varepsilon_I = 0$ (from [14]). For the semi-infinite media, the LR-SPP curves lie below the "light" lines for each medium, indicating the non-radiative, or bound, nature of SPPs. In reality, due to dissipation in the metal, ε_I, is positive, which leads to a finite propagation length (complex propagation constant β).

For a finite film thickness, the SPP modes, associated with each interface, are coupled and form two mixed modes. The dispersion of these waves depends on the thickness of the metal. For a symmetrical structure $(\varepsilon_1)^{1/2} = (\varepsilon_3)^{1/2}$ the modes stay below the light line (non-radiative) for all film thicknesses. When $(\varepsilon_1)^{1/2} \neq (\varepsilon_3)^{1/2}$, with the decrease in metal thickness one of the modes may start to leak (radiate) into the medium with higher refractive index. The studies of SPP modes propagating along thin metal films surrounded by dissimilar dielectrics have shown that LR-SPPs could be supported even by highly asymmetric configurations [64].

3.1.2 Guiding by symmetric structures

In symmetric structure $(\varepsilon_1)^{1/2} = (\varepsilon_3)^{1/2}$, the physically important solutions, corresponding to non-radiative waves, represent two modes with the fields exponentially decaying into both the ε_1 and the ε_3 media. Because of the symmetry of the structure, the field distributions should be either

symmetric or antisymmetric with respect to the center of the metal film. The symmetric mode profile has no zero-crossing inside the metal while the asymmetric mode profile has one zero-crossing (Figure 3.2). For the antisymmetric mode, the increase in real part of the propagation constant β_R with decreasing film thickness leads to an increase in the decay constant (or propagation loss). This "lossy" mode, formed by two SPPs, is often called *short-range SPP*. Conversely for the symmetric mode, *long-range SPP*, as the real part of the propagation constant β_R approaches the propagation constant in the dielectric $(\varepsilon_1)^{1/2} \cdot k_0$ (as $t \to 0$), the dissipation in the metal is reduced [14]. With the thickness of metal going to zero, the LR-SPP fields in the dielectric media approach those of a plane wave and the loss goes to zero (for a lossless dielectric) [14].

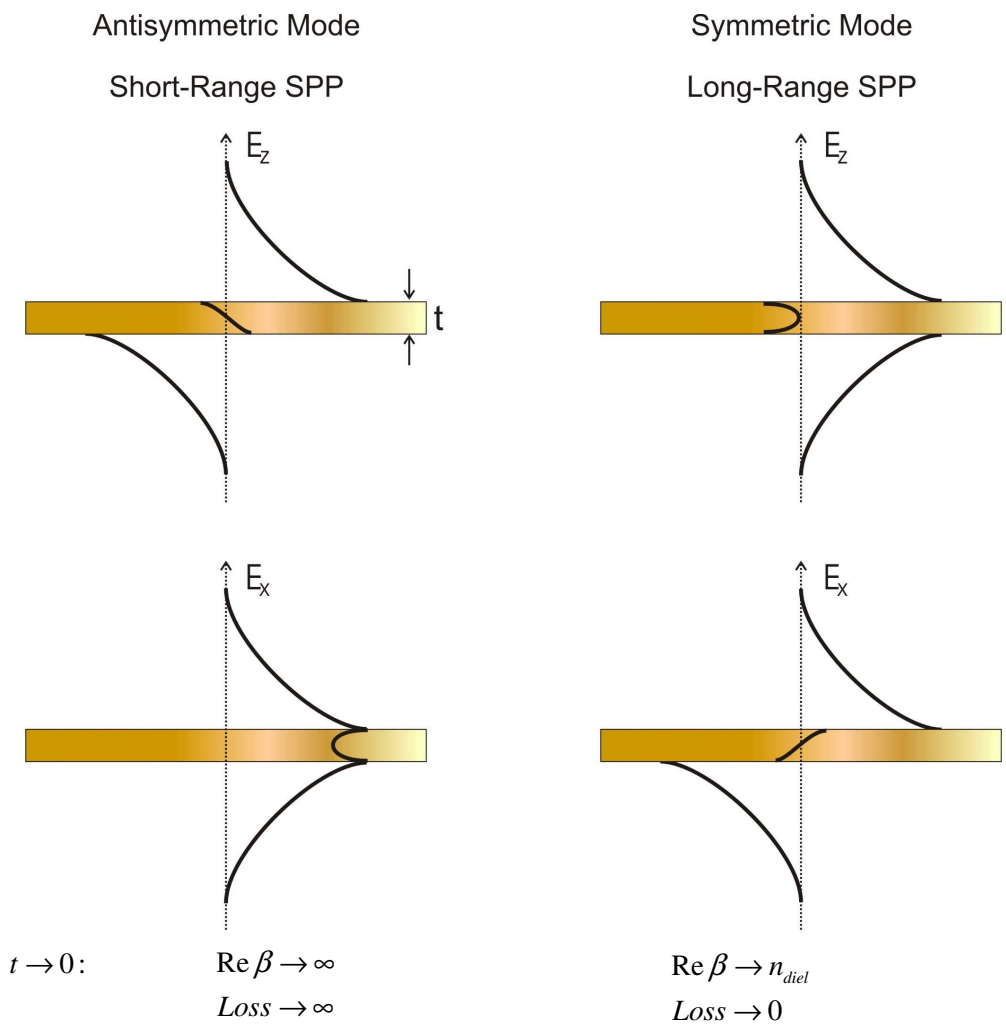

Figure 3.2 Field distributions for short-range and long-range SPPs together with the comparative behavior of the real part of the propagation constant (β) and loss with the decreasing metal thickness ($t \to 0$).

It is the symmetric, LR-SPP mode that is of practical interest because of the long propagation length achievable for thin metal films. For example, at a wavelength of 633 nm the propagation

length increases from 22 µm for SPP on semi-infinite metal to 610 µm for LR-SPP propagating along a 15-nm-thick silver film embedded in a dielectric (n=1.5).

3.1.3 Propagation loss

To proceed with the numerical solutions for LR-SPP modes, infinitely wide metal stripes embedded in a lossless dielectric with the refractive index n = 1.535 (which corresponds to the dielectric material used in this work) are considered. The LR-SPP modes characteristics were studied using a one-dimensional mode solver by Kymata Software.

The propagation loss dependence on the thickness of the metal film is presented in Figure 3.3 for two different metals at 1550 nm. The propagation loss decreases monotonically with the reduction in metal thickness and approaches a regime with a loss less than 1 dB/cm. In practice, fabrication of continuous metal film thinner than 10 nm is very difficult; and hence the lower limit for LR-SPP propagation loss is approximately 1 dB/cm, which is acceptable for many photonic applications.

The wavelength dependence of the propagation loss for two different thicknesses of the metal film is shown in Figure 3.3. For example, for 10-nm-thick gold film, the loss increases monotonically towards shorter wavelengths from ~ 1 dB/cm at 1700 nm to ~ 3 dB/cm at 1300 nm.

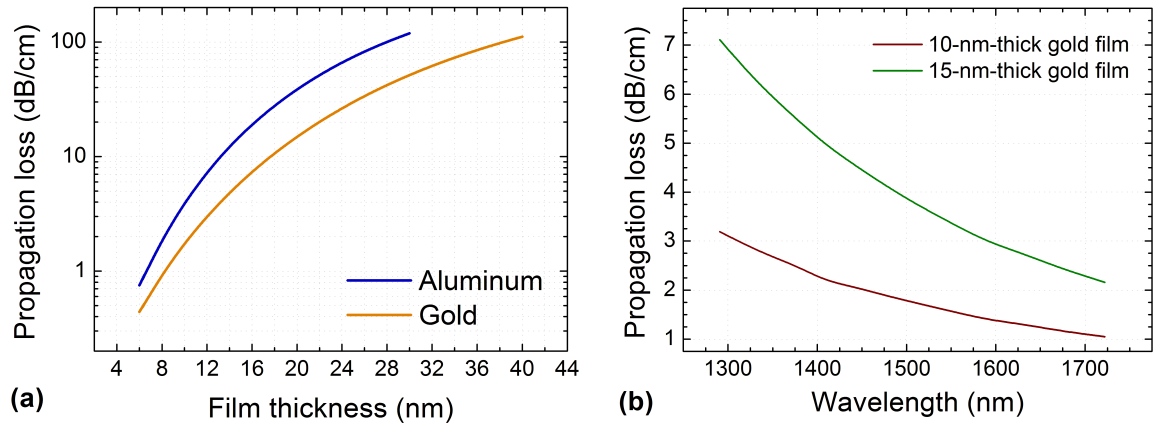

Figure 3.3 **(a)** Calculated LR-SPP propagation loss at 1550 nm for different thicknesses of gold and aluminum films and **(b)** wavelength dependence of the LR-SPP propagation loss for 10- and 15-nm-thick gold film.

In order to consider a structure close to real samples, the symmetrical geometry shown in Figure 3.4 (left) is analyzed. A metal film of thickness t is surrounded by two identical dielectric layers characterized by the refractive index n = 1.535, corresponding to the refractive index of

BCB (Benzocyclobutene) polymer at the light wavelength of 1.55 µm, and thickness *d*. The structure is placed on a silicon substrate with the refractive index 3.47. The metal in this analysis is gold with the complex refractive index $n = 0.55 + 11.5i$ [65].

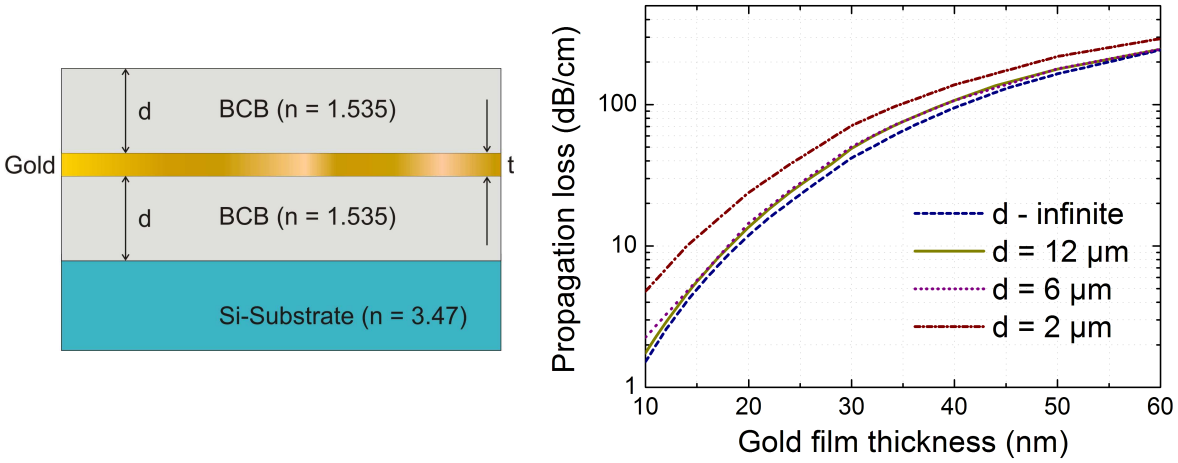

Figure 3.4 Calculated LR-SPP propagation loss (at 1550 nm) for different thicknesses of polymer cladding layers in the structure shown on the left.

The LR-SPP propagation loss at the wavelength of 1.55 µm was analyzed for different thicknesses of metal film and BCB cladding (Figure 3.4). In the case of infinite polymer cladding, the propagation loss was found to increase monotonically with increasing film thickness from ~ 1.5 dB/cm (for a 10-nm-thick gold film) to ~ 250 dB/cm (for a film thickness of 60 nm). For 12-µm-thick polymer claddings the loss increases from ~ 1.7 dB/cm for a 10-nm-thick gold film to ~ 250 dB/cm for a film thickness of 60 nm. The reduction in the cladding thickness leads to an increase in propagation loss, which is connected to the fact that the polymer layers become too thin to accommodate the LR-SPP field. For example, for a 10-nm-thick metal film, reducing the polymer thickness to 2 µm changes the LR-SPP propagation loss from ~ 1.5 dB/cm to ~ 5 dB/cm (Figure 3.4). This is accompanied with the changes in the LR-SPP mode field profile and is discussed in the following section.

3.1.4 Vertical mode field diameter

The vertical mode profile consists of two exponential tails that decay into the dielectric media. For infinite dielectric surroundings, the decay length is determined by the metal thickness and reflects how tight the LR-SPP is bound to the metal (Figure 3.5). With decreasing thickness of the metal, the LR-SPP mode becomes less bound to the metal and it penetrates deeper into the dielectric.

Even though the transverse distribution of the LR-SPP mode is by nature not Gaussian, it turns out that the overlap integral between the LR-SPP and a Gaussian distributions can be better than 97% (Figure 3.5). The mode field diameter (MFD) for the intensity distribution is defined as the distribution width at the $1/e^2$ level. In the following, the Gaussian MFD, found by fitting a Gaussian distribution to the actual LR-SPP mode profile, is used for the comparison of the LR-SPP mode characteristics for different parameters of the structure.

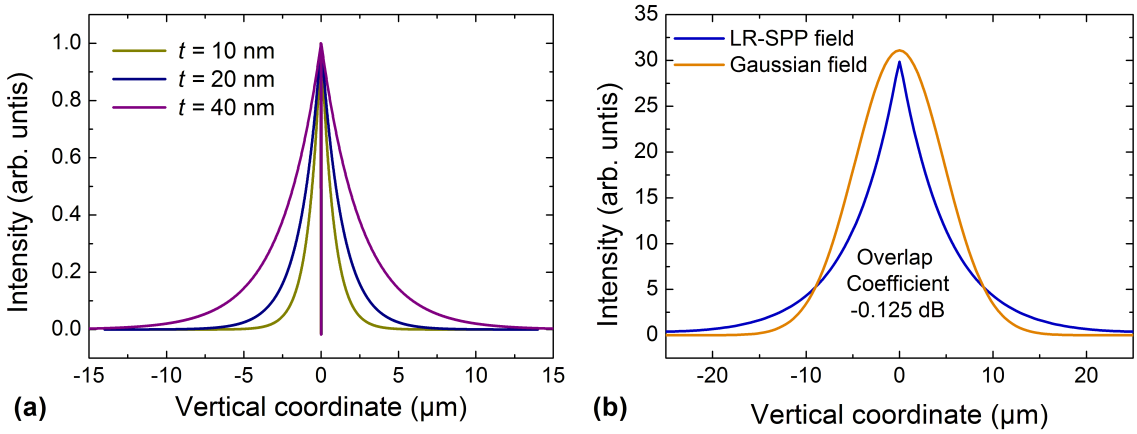

Figure 3.5 **(a)** Calculated vertical mode profiles for the LR-SPP propagating along a gold film embedded in an infinite dielectric (n=1.535) for different film thicknesses together with **(b)** the Gaussian fit to the LR-SPP profile for 10-nm-thick film.

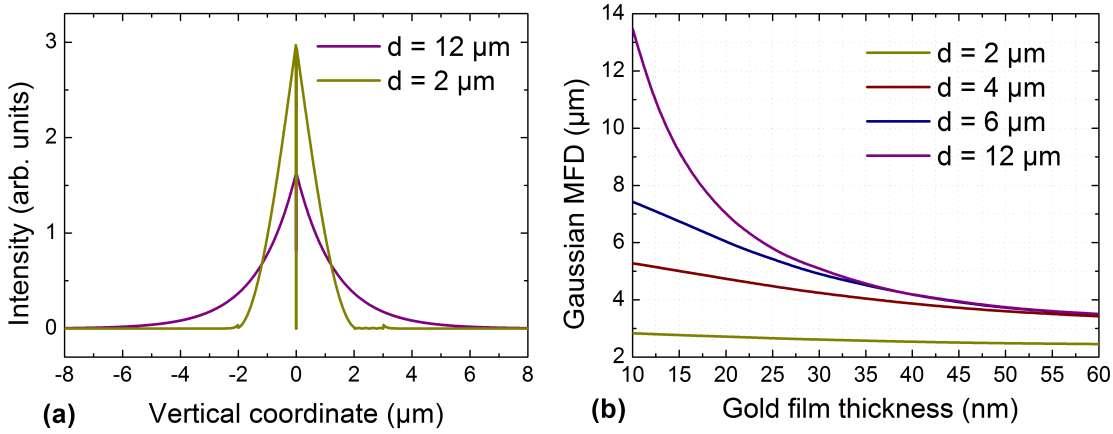

Figure 3.6 **(a)** Calculated vertical mode profiles for the 20-nm-thick gold film for two different thicknesses of the polymer cladding and **(b)** the Gaussian mode field diameter for different thicknesses of polymer cladding layers. The wavelength is 1550 nm.

In practice, in order to support LR-SPP propagation with low propagation loss, one should ensure a symmetrical structure. This means that the two polymer layers should have the same refractive index and be thick enough so that the LR-SPP EM field is located inside the polymer and does not penetrate into the silicon substrate or the air. For sufficiently thick enough cladding layers,

the LR-SPP mode profile in depth (perpendicular to the sample surface) is primarily determined by the metal thickness.

For finite thicknesses of the polymer claddings (see geometry in Figure 3.4), the mode profile depends not only on the thickness of the metal layer but also on the cladding thicknesses. The polymer thickness can be used to tune the vertical profile of the LR-SPP mode as demonstrated in Figure 3.6 (a). For a gold thickness of 20 nm, the width of the LR-SPP depth profile changes from ~ 10 µm for a 12-µm-thick cladding to ~ 4 µm for a polymer thickness of 2 µm.

3.1.5 Effective refractive index

The dependence of the LR-SPP effective refractive index on the gold film thickness is presented in Figure 3.7 for infinite and 6-µm-thick dielectric claddings.

Since the change in the effective refractive index is small compared to the absolute value of the refractive index itself, the plotted value b, for convenience, shows the difference between the LR-SPP effective refractive index and the refractive index of the cladding. The normalized index b is determined as

$$b = \frac{N_{eff} - n_{cl}}{n_{cl}} \qquad [3.8]$$

where n_{cl} is the refractive index of the cladding (1.535), and N_{eff} is the mode effective refractive index.

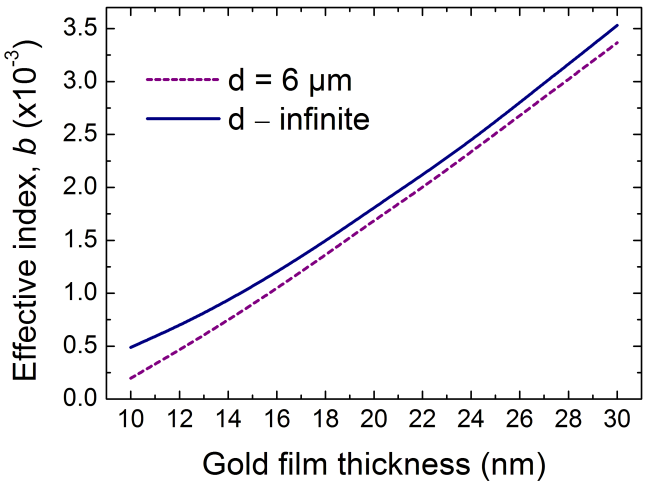

Figure 3.7 Calculated normalized LR-SPP effective refractive index calculated for infinite and 6-µm-thick polymer claddings.

3.1.6 The influence of the asymmetry of the structure

To study how a slight asymmetry will influence the LR-SPP properties, the same geometry as in Figure 3.4 was analyzed for a polymer cladding thickness of 12 µm only with variable refractive index of the top cladding (Figure 3.8).

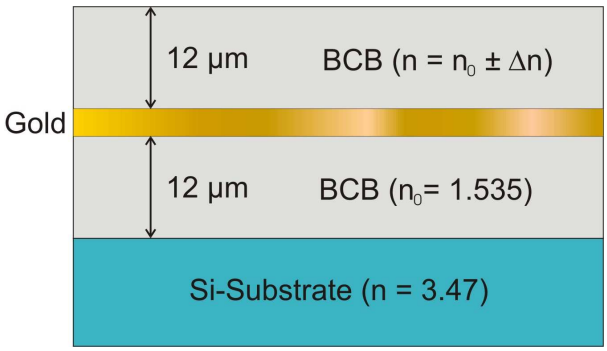

Figure 3.8 Sample geometry with variable refractive index of the top polymer cladding.

The dependence of the LR-SPP propagation loss on the refractive index difference between top and bottom cladding layers is shown in Figure 3.9 for gold thicknesses of 10 and 15 nm. The asymmetry-sensitive LR-SPP mode was found to have a propagation loss increasing from 1.7 dB/cm for a symmetrical structure to approximately 4 dB/cm for a refractive index difference of ± 0.006 for a 10-nm-thick film.

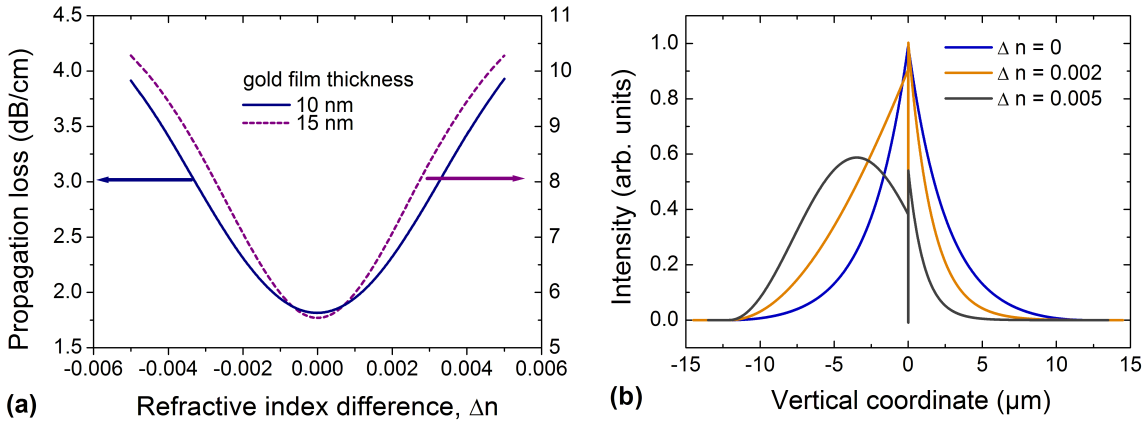

Figure 3.9 (a) Calculated dependence of the LR-SPP propagation loss on the refractive index difference between the two polymer claddings, Δn, together with **(b)** the vertical field distribution for the 10-nm-thick gold film for three different Δn. For Δn > 0.005 one of the modes starts to leak into the medium with the higher refractive index. The wavelength is 1550 nm.

The vertical mode profile was also found to change significantly depending on the asymmetry of the structure. The increase in the propagation loss with the increasing asymmetry is

accompanied by the change from a symmetrical LR-SPP mode depth profile to an asymmetrical one (Figure 3.9). Further increase of the refractive index difference (more than ± 0.005) will create a standard slab waveguide formed by a polymer layer with higher refractive index surrounded by two media with lower refractive index, leading to the situation when one of the SPP modes becomes leaky (Figure 3.9).

3.2 LR-SPP guiding by thin metal stripes: Effective refractive index approach

3.2.1 The effective refractive index method

Confinement of the light within the metal film plane can be achieved by making narrow metal stripes in analogy with dielectric waveguides. The properties of LR-SPP modes guided by a waveguide structure composed of a thin lossy metal film of finite width, surrounded by a dielectric, were for the first time studied theoretically by Berini in 2000 [17]. In the simple qualitative analysis, the characteristics of the LR-SPP mode were found by using the *effective-refractive-index method*, which is considered to be reasonably accurate for waveguide modes being far from cutoff [66].

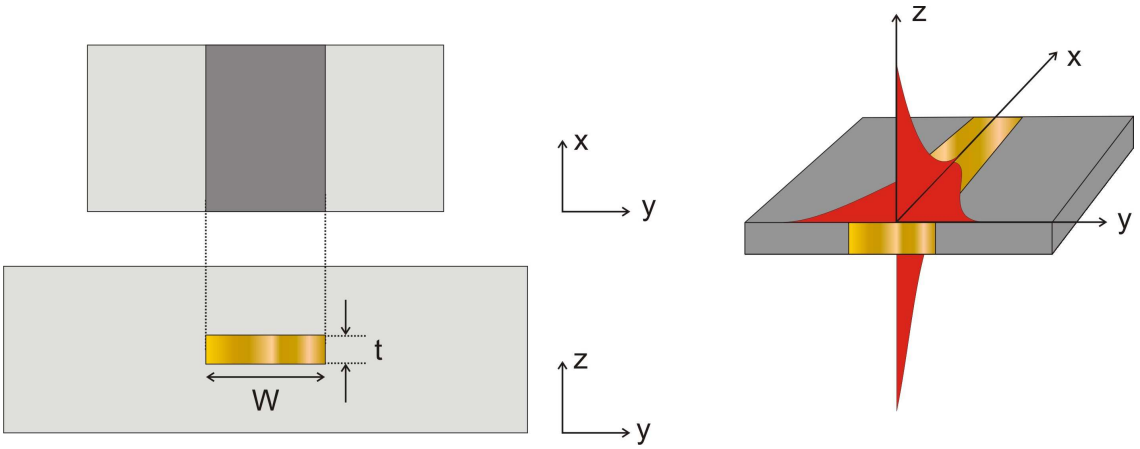

Figure 3.10 (Left) Cross section **(z,y)** and top view **(x,y)** of a stripe waveguide together with **(right)** mode field distributions in transverse **(z)** and lateral **(y)** directions.

In this approach, in the first step, the structure with an infinitely wide metal film is analyzed yielding the vertical LR-SPP mode profile and the effective index (geometry in Figure 3.4). For example, at 1.55µm, the effective index for a 10-nm-thick gold film is found to be N_{eff}=1.535755+0.00000496*i*. In the second step, a symmetric slab waveguide, suggested by the top view of Figure 3.10, is considered. This slab has a thickness equal to the width of the metal stripe

and a core refractive index of N_{eff}. The effective refractive index uses the guiding characteristics of this equivalent slab waveguide to predict the guiding characteristics of the stripe waveguide in the *y*-direction. This is simply done by substituting the effective refractive index N_{eff} for the metal film and performing calculations for a TE mode propagating in such a slab.

The geometry of the structure used in this work is shown in Figure 3.11. A metal stripe of variable thickness *t* and width *w* is surrounded by a polymer characterized by the refractive index *n*. The whole structure is placed on a silicon substrate.

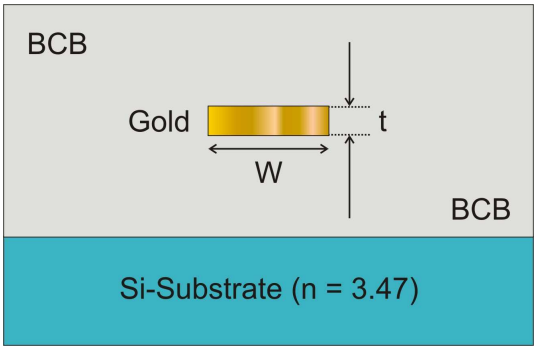

Figure 3.11 The geometry of a metal stripe of variable thickness *t* and width *w* surrounded by a polymer (n =1.535) layers. The structure is placed on a silicon substrate (n =3.47).

While analysis of the structure with the infinitely wide metal film yields the vertical LR-SPP mode profile, the effective refractive index method provides the lateral mode profile (parallel to the sample surface) as well as a corrected value for the mode effective refractive index and the propagation loss.

3.2.2 Mode effective index and propagation loss

The effective index of the LR-SPP mode as a function of the waveguide width for a 10-nm-thick stripe is shown in Figure 3.12. For each mode, the mode effective index increases monotonically with increasing stripe width. The simulations indicated that, for the stripe thickness of 10 nm, the multi-mode regime sets in for stripes wider than 20 µm (Figure 3.12). This feature was used to design MMI waveguides (section 3.2.4). For 15-nm-thick metal, this regime starts already at a stripe width of 12 µm.

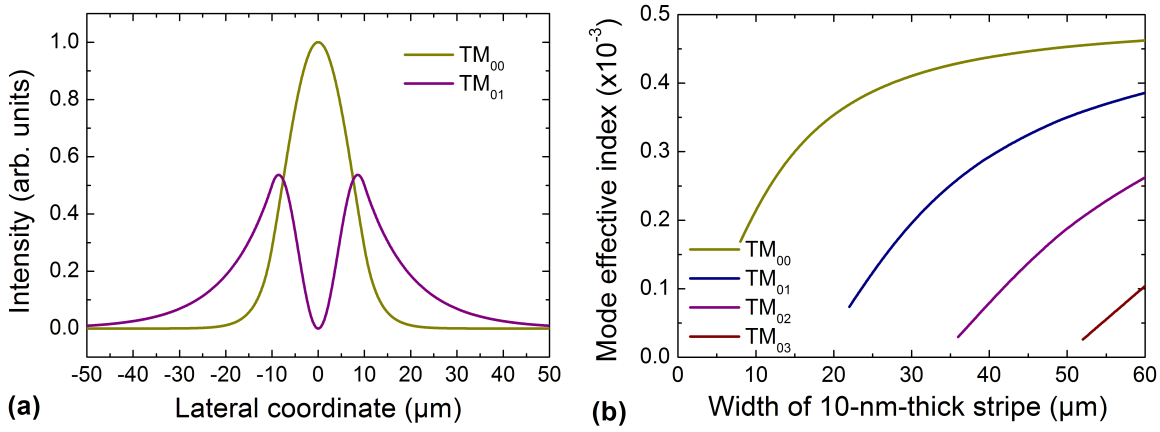

Figure 3.12 (a) The fundamental and second order modes for 10-nm-thick and 20-μm-wide stripe together with **(b)** the LR-SPP mode effective index for a 10-nm-thick stripe. Modeling performed using the effective index approach.

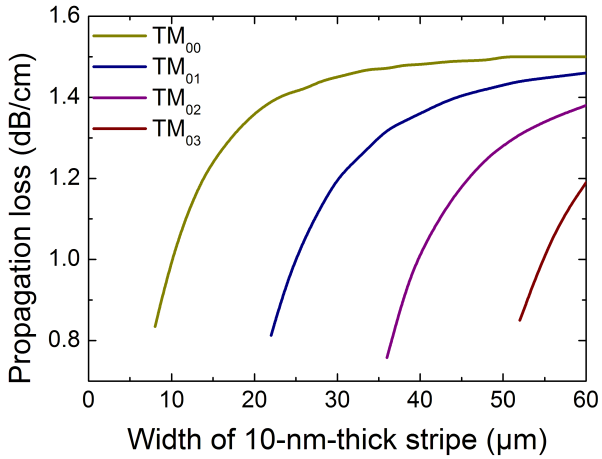

Figure 3.13 The LR-SPP propagation loss for a 10-nm-thick stripe. Modeling performed using the effective index approach.

The propagation loss was found to decrease with the stripe width (a similar trend was also predicted theoretically in [17,50] by using more exact models) implying the possibility to reach very low propagation loss. For example, propagation loss below 1 dB/cm can be achieved for a 10-nm-thick stripe by reducing its widths to below 5 μm (Figure 3.13).

3.2.3 Lateral mode field diameter

The lateral LR-SPP mode field diameter is found as the MFD of the Gaussian curve fitted to the lateral LR-SPP field distribution (Figure 3.14). The lateral MFD as a function of the stripe width for gold film thicknesses of 10 and 14 nm is shown in Figure 3.14. The MFD was found first to

decrease following the decrease in the stripe width and then to increase again indicating a poorer light confinement by narrow stripes, which has also been shown using more detailed theoretical models [17].

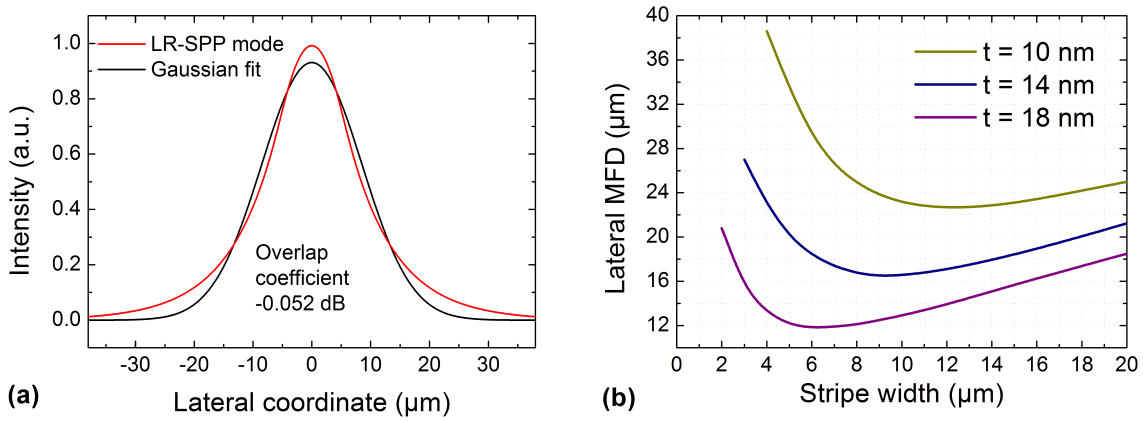

Figure 3.14 (a) The lateral mode profile fitted to a Gaussian distribution for a 10-nm-thick and 10-μm-wide stripe together with **(b)** the lateral LR-SPP mode field diameter for different gold film thicknesses.

3.2.4 Modeling of multi-mode interference waveguides

Multi-mode interference (MMI) is widely used in many key components in integrated optics, including splitters, recombiners, and couplers. An MMI device comprises a wide multi-mode waveguide in which the interference between different modes leads to self-imaging effects [22]. By placing the output waveguides at different image points it is possible to implement a wide range of splitting, wavelength division, and recombining functions with the possibility of a large number of input and output arms.

The description of the underlying self-imaging principle as well as a complete analysis of MMI devices can be found in [22]. The beat length between two lowest-order modes, L_π, can be expressed as:

$$L_\pi = \frac{\pi}{(\beta_0 - \beta_1)} = \frac{\lambda}{2\left(N_0^{eff} - N_1^{eff}\right)} \qquad [3.9]$$

where λ is the wavelength, β_0, β_1, N_0^{eff} and N_1^{eff} are the propagation constants and effective indices of the zero- and first-order mode, respectively (Figure 3.15), calculated by using the effective refractive index method.

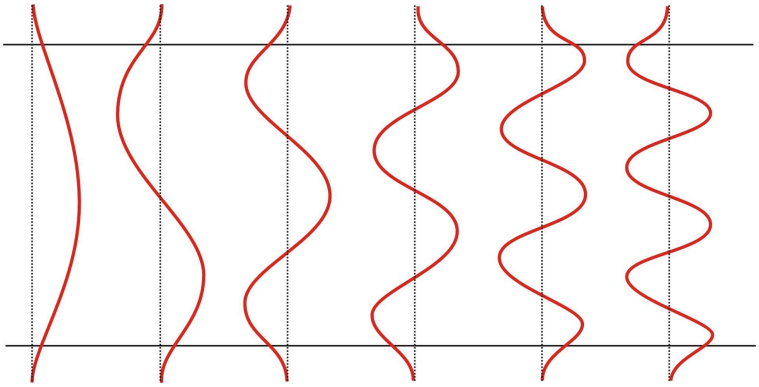

Figure 3.15 Lateral field profiles (amplitude-normalized), corresponding to the first 6 guided modes in a multi-mode waveguide.

For a single-mode input waveguide positioned symmetrically with respect to the MMI center line, *N*-fold images are obtained at distances [22]:

$$L = \frac{p}{N}\left(\frac{3L_\pi}{4}\right) \text{ with } p=0,1,2,\ldots \qquad [3.10]$$

As an example, a 14-nm-thick and 40-μm-wide gold stripe embedded in an infinite dielectric is considered. In this multi-mode waveguide, a symmetric input beam excites two lowest symmetric modes (00 and 02). The effective indices for the 00 and 02 modes are 1.536344 and 1.535678 respectively. This gives a beat length of 1.164 mm, which allows calculating the distances to the single- (or one-fold) and double (or two-fold) image planes.

3.2.5 Modeling of directional couplers

Directional couplers (DCs) are also very important components in the field of integrated optics since they are used in optical switches, power dividers, filters, and modulators. The directional coupler consists of two straight waveguides that are placed sufficiently close to each other so that optical energy can be transferred from one waveguide to the other.

The simplest model of the coupled-waveguide system consists of two uniform, parallel waveguides in close proximity (Figure 3.16). The conventional principle of coupling is based on the existence of evanescent mode fields outside the waveguides. In this case, the coupling coefficient falls off exponentially with the separation distance. Theoretical analysis for coupled optical waveguides can be performed using coupled-mode theory, which gives simple analytical solutions for the mode-coupling process in a directional coupler device [67,68].

The power transmitted through the direct, I_{II}, and coupled, I_x, arms of a DC with the interaction length L can be written as [68]:

$$I_{II} = \cos^2(\kappa L), I_X = \sin^2(\kappa L) \qquad [3.11]$$

where κ is a wavelength dependent coupling constant. The coupling length corresponding to full power transfer from one arm to another is then defined as

$$L_{\pi/2} = \pi / 2\kappa \qquad [3.12]$$

In order to describe a directional coupler, the same approach as for modeling of MMI devices is used. The coupling region is modeled as two parallel waveguides (Figure 3.16); and the coupling length is estimated as a beat length between the two lowest order modes.

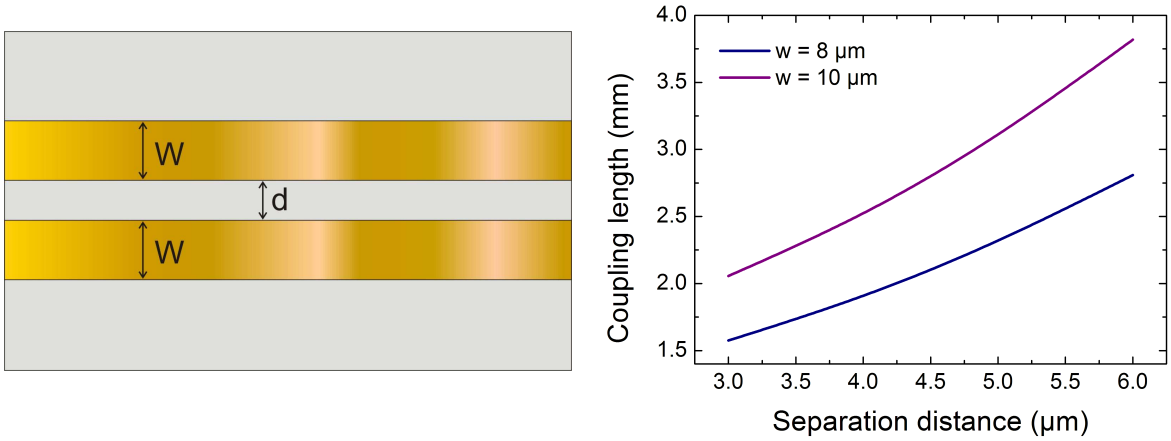

Figure 3.16 (Left) Coupling region of a directional coupler based on stripe waveguides of width *w* separated by a distance *d* together with **(right)** calculated coupling length vs. separation distance.

The dependence of the coupling length on the separation distance between waveguides is presented in Figure 3.16 showing the increase in the coupling length with the increasing separation between waveguides. This behavior is in agreement with the conventional DC theory based on exponential field decay away from the waveguides.

4 Waveguide Components Utilizing Long-Range Surface Plasmon Polaritons

Perfect as the wing of a bird may be, it will never enable the bird
to fly if unsupported by the air. Facts are the air of scientist,
without them you can never rise.
Ivan P. Pavlov

This chapter starts by describing the design and fabrication of polymer-based stripe waveguides supporting long-range surface plasmon polariton propagation. Experimental findings are presented for optical characterization of fabricated waveguides and waveguide components at telecommunication wavelengths. Guiding of LR-SPPs along thin gold stripes embedded in polymer is investigated for different thicknesses and widths of stripes. The description of the fabrication procedure and experimental arrangement are followed by experimental results for the propagation loss for different stripe thicknesses. Thereafter, mode profile measurements are presented as part of the optical characterization of straight waveguides. Realization of LR-SPP-supporting bends and splitters as well as multi-mode interference devices is also reported. Finally, coupling between two waveguides in directional couplers is studied and coupling lengths are determined for directional couplers with different parameters and compared with the values obtained from the effective-refractive-index approach.

4.1 Fabrication and experimental arrangement

To fabricate LR-SPP stripe waveguides, a silicon substrate (4" or 6") was first spin coated with a layer of BCB (Benzocyclobutene) polymer with a thickness of 13-15 µm and then with a layer of UV resist. Stripe waveguides and waveguide devices were patterned using standard UV lithography, gold deposition and lift-off. As a final fabrication step, the spin coating of the top cladding, consisting of another 13- to 15-µm-thick BCB layer, was performed. Since the symmetry of the structure is very important for the LR-SPP properties (propagation loss, mode field diameter)

it was carefully ensured that the cladding layers had the same refractive index and were thick enough to accommodate the EM field of the LR-SPP. This was realized by applying the same polymer for the top and bottom claddings under identical spinning and curing conditions. After the final polymer curing the wafer was cut into individual samples.

Fabricated samples included straight stripe waveguides of different widths (from 2 µm to 12 µm), S-bends of different lengths with 200-µm-offset, Y-splitters, 40- and 60-µm-wide multimode waveguides, and directional couplers with different interaction lengths and separations. The multimode waveguides were connected to single-mode (8-µm-wide) waveguides positioned symmetrically with respect to the MMI center line.

For optical characterization of the LR-SPP stripe waveguides and waveguide devices standard transmission measurements were carried out (Figure 4.1). In order to excite the LR-SPP mode, "end-fire" coupling of light was performed using a tunable laser (1550 nm or 1570 nm) or a broadband light source (two multiplexed LED diodes – 1310 nm and 1550 nm), together with a polarization controller. Light polarized perpendicular to the waveguide plane was launched into the LR-SPP waveguide by butt-coupling from a polarization-maintaining (PM) fiber with a MFD of 10.8 µm. To ensure that the polarization of light was orthogonal to the waveguide layer, angular adjustments of the PM fiber were performed. 1 km of coiled standard single mode fiber was used as out-coupling fiber in order to strip off all light coupled into the fiber cladding. Index matching gel was used to decrease the scattering due to roughness and reflection at the sample edges. The output signal was detected by a powermeter (for measurements performed with the laser) or an optical spectrum analyzer (for broadband measurements).

The adjustment of the in- and out-coupling fibers with respect to the stripe waveguide was accomplished by maximizing the amount of light transmitted through a waveguide (active alignment). It should be mentioned that almost all light coupled from the input fiber to the cladding was stripped away before reaching the end facet of the sample so that only the LR-SPP mode confined to the waveguide was observed at the output making the alignments of the fibers quite easy.

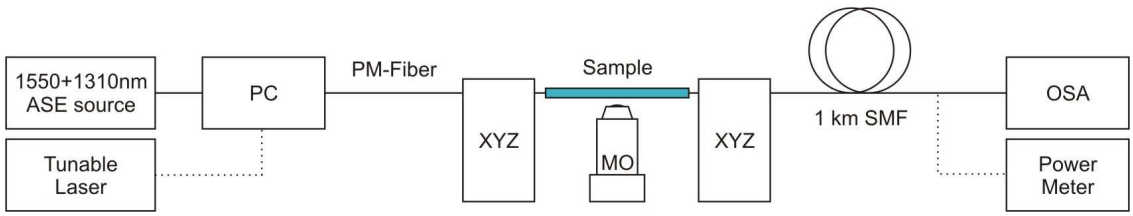

Figure 4.1 The layout of the transmission measurements setup for optical characterization of LR-SPP waveguide components (PC – polarization controller, PM – polarization maintaining, MO – microscope objective, SMF – single mode fiber, OSA – optical spectrum analyzer).

The output intensity distribution from a stripe waveguide was monitored via an infrared Vidicon camera through ×200 magnification. The PM fiber output with a known MFD was used for the calibration of the mode profile measurement system.

4.2 Straight waveguides

4.2.1 Propagation loss

Propagation loss measurements were performed for 8-µm-wide straight stripe waveguides of different thicknesses (thickness of the deposited gold layer) from approximately 9 nm to 35 nm. The propagation loss at a given wavelength was found as the slope of the linear fit to the experimental values of the total insertion loss obtained for different lengths of the LR-SPP waveguide (4, 8, and 14 mm for waveguide thicknesses up to 15 nm and 2, 3, and 4 mm for thicknesses up to 35 nm) (cut-back method). This linear fitting technique allowed the coupling loss to be estimated from the intersection point on the loss axis corresponding to zero length of the waveguide. The coupling loss for a 15-nm-thick stripe waveguide varied from approximately 0.5 dB per facet for a 10-µm-wide waveguide to ~ 1.5 dB for a 4-µm-wide stripe. Figure 4.2 shows the experimental results for the propagation loss at 1550 nm together with the LR-SPP propagation loss curve calculated for infinitely wide stripes.

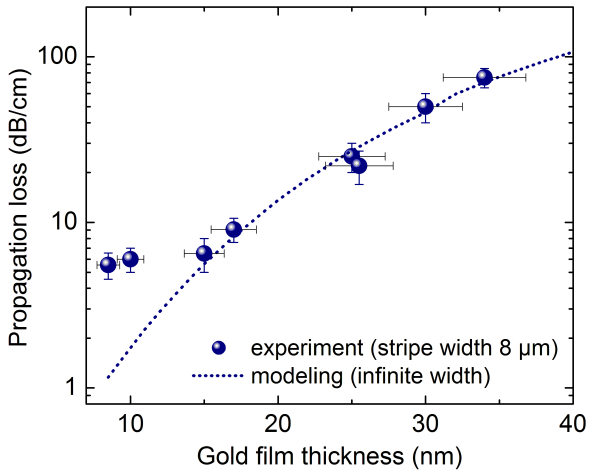

Figure 4.2 Measurements of the propagation loss dependence on the thickness of 8-µm-wide gold stripes at the wavelength of 1550 nm together with the propagation loss curve calculated for infinitely wide stripes.

Good agreement between experimental and calculated values, observed for waveguide thicknesses higher than 15 nm, clearly indicates that for thick gold films the internal damping in the

metal (Ohmic loss) is dominating. For thin waveguides, higher values of experimentally obtained propagation loss compared to the calculated values can be explained by the presence of other loss mechanisms such as scattering by inhomogeneities in the gold film and at the waveguide edges, and scattering and absorption in the polymer. By eliminating the described loss mechanisms one should, in principle, achieve the fundamental loss limit set by the internal damping in the metal, which is approximately 1.5 dB/cm for a 10-nm-thick infinitely wide stripe and decreases with the stripe width [17,50]. In the samples investigated here, a reduction of the stripe thickness (below 15 nm) did not lead to a significant decrease in the propagation loss due to fabrication difficulties in creating a very thin *homogeneous* metal layer. Furthermore, since the flatness of a nm-thin film can be strongly influenced by the substrate surface, it is the rough polymer surface that, in this case, sets a 10-15-nm limit on the film thickness. AFM measurement showed that for the fabricated samples, polymer roughness was on the order of 3-4 nm.

4.2.2 Long-range surface plasmon polariton mode profile

In order to study the LR-SPP mode profile, the output intensity distribution from a stripe waveguide was monitored using a microscope arrangement imaging the waveguide output on an infrared Vidicon camera. The intensity distribution at the output of the 15-nm-thick stripe waveguide is shown in Figure 4.3 for three different waveguide widths.

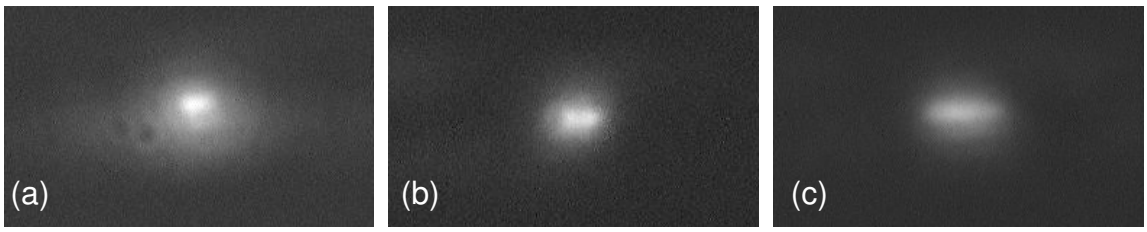

Figure 4.3 The output intensity distribution at the output of a 15-nm-thick stripe waveguide for a **(a)** 4- , **(b)** 8- and **(c)** 12-µm-wide stripe.

The vertical mode profile consists of two exponential tails with a decay length, primarily determined by the metal thickness. However, for narrow stripes (less than 6-µm-wide) the vertical MFD is expected to increase compared to the infinitely wide stripe of the same thickness [17], which is also observed from the experimentally obtained mode profiles (Figure 4.3). The vertical LR-SPP profile for an 8-µm-wide stripe together with the exponential fits is presented in Figure 4.4 showing quite good match except for the area around zero, where the intensity distribution was smoothened to a Gaussian-like shape due to the limited resolution (1-1.5 µm) of the imaging system.

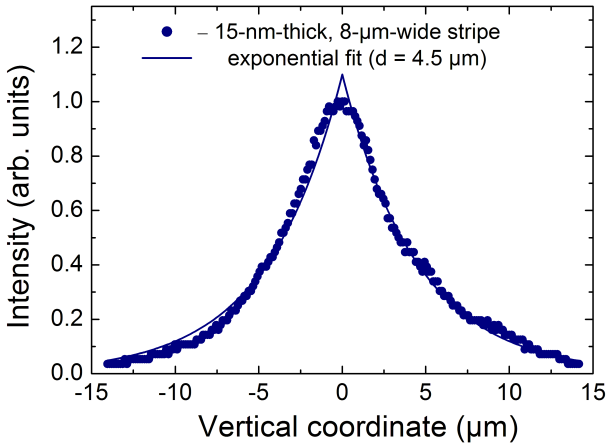

Figure 4.4 The transverse LR-SPP mode profile for a 15-nm-thick and 8-µm-wide stripe together with the exponential fit.

The lateral mode field profile was found to fit well to a Gaussian distribution. The lateral mode field diameter as a function of the stripe width is presented in Figure 4.5. The lateral MFD was found to decrease from ~ 12 µm for a stripe width of 12 µm to ~ 10 µm for 6-8-µm-wide stripes, following the decrease in waveguide width. It then start to increase again, reaching ~ 16 µm for a 2-µm-wide stripe waveguide, due to weaker light confinement [17]. This behavior is found to be in good agreement with the simulation results (Figure 3.14). The systematic error can be attributed to the difference between the dielectric constant of gold used in calculations and that of the actual structure.

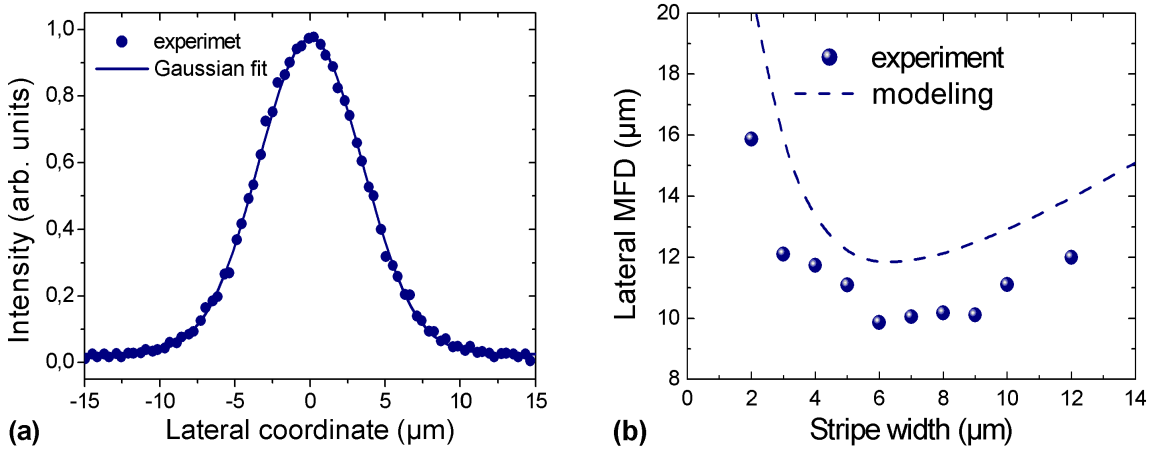

Figure 4.5 (a) An example of the lateral intensity profile fitted to a Gaussian distribution together with **(b)** the lateral mode field diameter vs. waveguide width (measurements and modeling for 15-nm-thick stripes).

The described features of the LR-SPP mode profile in the lateral and transverse directions provide the possibility to significantly reduce the coupling loss between an LR-SPP stripe waveguide and a standard single-mode fiber (down to ~ 0.1 dB) by choosing proper stripe dimensions and thus fitting the LR-SPP mode profile to that of the fiber.

4.3 Bends

The connection between two straight and parallel waveguides that are offset with respect to each other, is usually called an *S-bend*. Several approaches for the design of S-bends have been reported [18,19] aiming at low additional loss and moderate increase in device length. An intuitive bend design is a combination of two circular arcs and, although simple, it already performs better than the one composed of straight sections with sharp corners (sharp bends). Further improvements are possible by removing discontinuities, not only in the first but also in the second derivative of the bend function, thereby eliminating abrupt curvature changes at the straight-curved transitions and at the midpoint of the S-bend. This approach can be realized with simple designs based on sine and cosine curves.

In this project, sharp and cosine S-bends based on 10- and 8-µm-wide and 15-nm-thick stripe waveguides were characterized. S-bends with lengths from 2.5 to 10 mm were used to connect two straight waveguides with an offset of 200 µm (Figure 4.7).

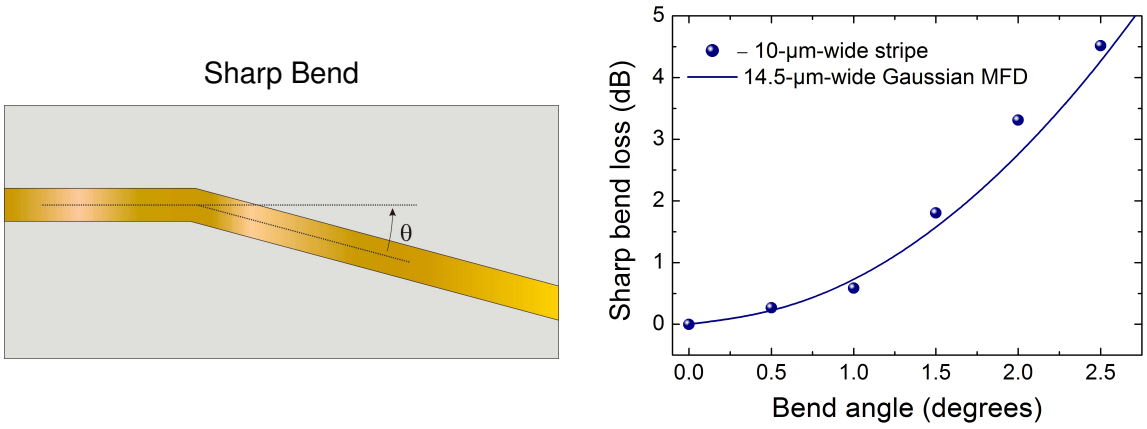

Figure 4.6 (Left) The schematic of a sharp bend and **(right)** the bend loss measured for a 10-µm-wide and 15-nm-thick waveguide in comparison with the quadratic bend loss curve [4.1] obtained for a Gaussian mode with MFD of 14.5 µm.

The bend loss for a sharp bend as a function of the bend angle was measured by normalizing the total insertion loss through the bend to the total loss for the straight waveguide of the same

length (Figure 4.6). All measurements are performed at 1550 nm. The bend loss can be estimated using the simple expression [69]:

$$Loss \cong 4.343\left(\frac{\pi n_{cl} W \theta}{2\lambda}\right)^2 \qquad [4.1]$$

where n_{cl} is the refractive index of the cladding, W is the mode field diameter and θ is the bend angle. The estimated values were found to be in a good agreement with the experimental results.

The S-bend loss as a function of curvature radius is shown in Figure 4.7 together with the calculated curve [19]. The flat plateau starting from a bend radius of approximately 40 mm gives the lower limit for the bend radius of the lossless bend. The bends contribute with an additional loss of ~ 2 dB when the bend radius is about 20-25 mm (corresponding to a 200-µm-offset and a S-bend length of 4.5 mm). For S-bend lengths shorter than 4 mm (bend radius smaller than 16 mm), the bend loss increases drastically, making these bends unsuitable for practical applications.

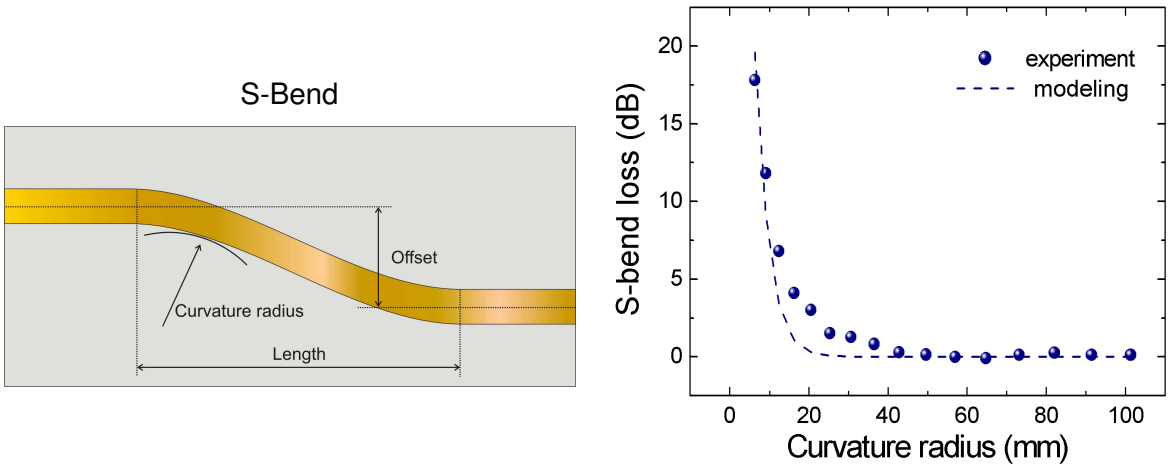

Figure 4.7 (Left) The schematic of an S-bend and **(right)** the S-bend loss as a function of minimum curvature radius along with the calculated curve [19].

Preliminary investigations showed that further (minor) improvements of the S-bend performance are possible by choosing other S-bend types, for example, sin$x$-x bends, which give slightly lower bend loss for the same waveguide offset and bend length. Some reduction in the bend loss can also be achieved by optimizing the stripe dimensions so as to increase the lateral mode confinement (in general, however, the propagation loss is larger for LR-SPP modes with better confinement).

4.4 Multi-mode interference waveguides

MMI-based devices [22], as previously mentioned, can be realized with LR-SPP-based technology. To demonstrate an LR-SPP-based MMI device that performs power splitting, 40- and 60-µm-wide LR-SPP stripe waveguides (waveguide thickness is 15 nm) were fabricated. The samples contained waveguides of different length. The width of the LR-SPP waveguides was chosen so that the waveguides were multimode, which in this case of 15-nm-thick waveguides corresponds to stripe widths of more than 12 µm (the cutoff width for the second mode).

The output intensity distributions for MMI-based devices of different widths and lengths (Figure 4.8 and Figure 4.9) were analyzed and compared to the intensity distribution pattern expected from the modeling.

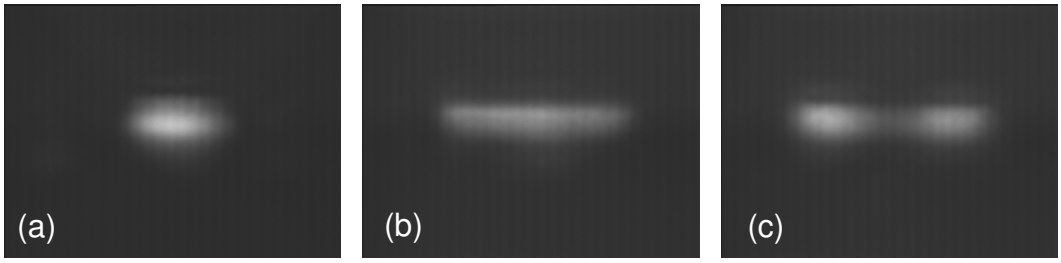

Figure 4.8 The output intensity distributions for 40-µm-wide MMIs of different lengths: **(a)** 2.3-mm-long; **(b)** 2.8-mm-long; **(c)** 3.3-mm-long.

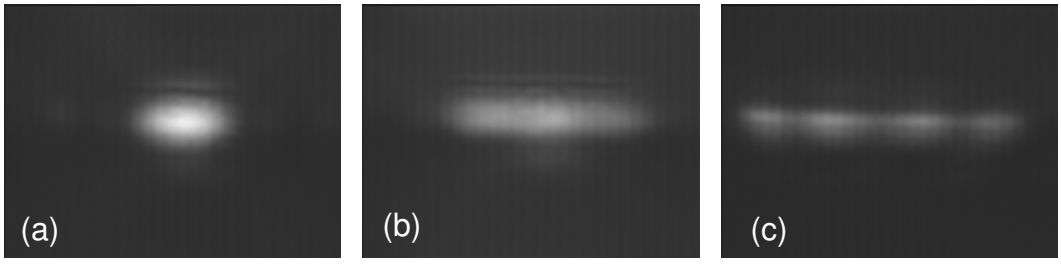

Figure 4.9 The output intensity distributions for 60-µm-wide MMIs of different lengths: **(a)** 4.6-mm-long; **(b)** 5.0-mm-long; **(c)** 5.5-mm-long.

For a 40-µm-wide waveguide, the distance from the input plane to the two-fold image plane was estimated from modeling to be 3.49 mm, which agrees very well with the output intensity distribution of the 40-µm-wide waveguide of 3.3 mm length. The experimentally observed 4-fold image for the 60-µm-wide and 5.5-mm-long waveguide was also found to be in excellent agreement with the simulations that predicted the 4-fold image plane to be 5.59 mm from the input plane.

4.5 Y-splitters

The simplest power splitter, often called a Y-splitter, consists of an input waveguide branching out to two arms using S-bends, as shown in Figure 4.10. Since single-mode Y-branch waveguides are key elements in the realization of power dividers, optical switches and Mach-Zehnder modulators, Y-splitters were fabricated and optically characterized in the wavelength range from 1475 to 1625 nm. Y-branches consisted of 15-nm-thick and 8-µm-wide LR-SPP stripe waveguides, with an arm separation of 250 µm, which corresponds to the standard pitch of a fiber array, and different splitting lengths from 5 to 10 mm.

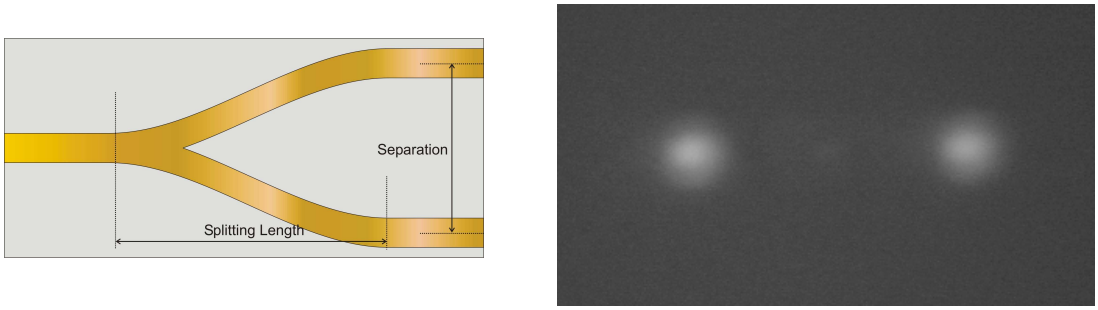

Figure 4.10 (Left) The schematic of a Y-splitter and **(right)** the output intensity distribution for the Y-splitter based on 10-µm-wide stripes. The arm separation is 250 µm.

Typical transmission spectra for both arms of the Y-splitters together with the transmission through a straight waveguide of the same length are shown in Figure 4.11 (a). For the straight waveguide, the total insertion loss of about 5.5-7 dB includes the propagation loss over 13 mm and the coupling losses (coupling to the in- and output fibers). The irregular shape of the curve is due to absorption in the polymer. By normalizing the transmission through the Y-splitter to the transmission through the straight waveguide, the loss induced by the Y-splitter was estimated for each arm of the Y-branch. For a splitting length of 10 mm, a 3 dB Y-splitter without additional loss was demonstrated, while a 5-mm-long Y-splitter was found to induce additional 0.5 dB loss for each arm (Figure 4.11 (b)). The difference in the transmission level for the two arms of the investigated Y-splitters was found to be within 0.3 dB, implying that such a device can be used in practice as a symmetrical power divider or 3-dB coupler.

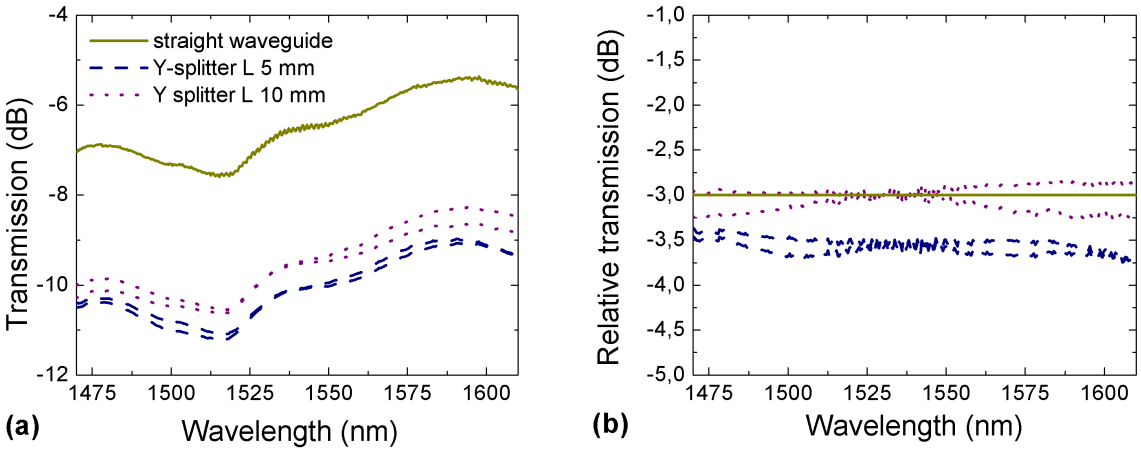

Figure 4.11 (a) Transmission spectra for both arms of the 5- and 10-mm-long Y-splitters with 250-µm-arm-separation together with the transmission through a straight waveguide of the same length, **(b)** relative transmission spectra.

4.6 Directional couplers

Directional couplers (DCs) based on 8-µm-wide stripe waveguides with different separation distances between waveguides (edge-to-edge) were investigated (Figure 4.12). DCs with the interaction length, L, varying from 0.1 to 1.5 mm in 0.1 mm steps, were investigated. For spectrally resolved measurements, devices with large interaction length (L = 8 mm) were used.

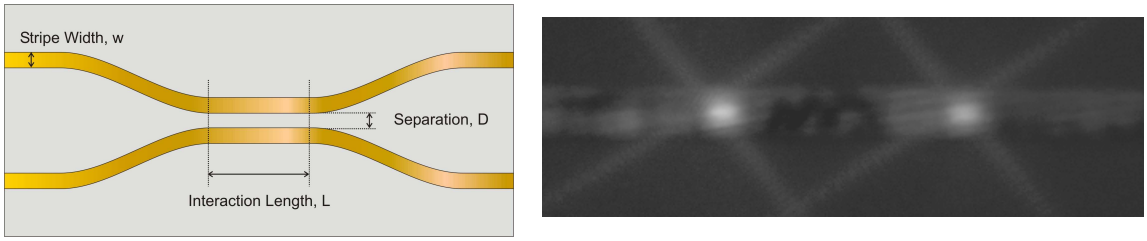

Figure 4.12 (Left) Schematic of the directional coupler (DC) constructed from straight waveguides and S-bends together with **(right)** an example of the DC output for the waveguide widths 8 µm, 0-µm-separation, and 0.9-mm-interaction-length. The output arms separation is 112 µm.

Typical transmission spectra for the direct and coupled arms of the DC based on 8-µm-wide waveguides with 6-µm separation (interaction length of 8 mm) are presented in Figure 4.13, showing efficient power transfer from one arm to another. An example of the output modes from the two DC arms is shown in Figure 4.12 (right), demonstrating a well-defined output mode from both arms and low level of background light in the polymer cladding.

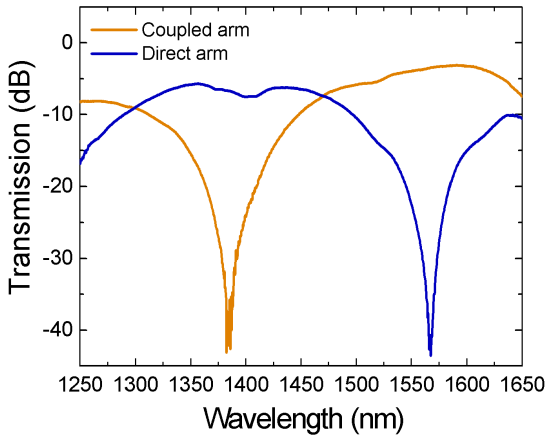

Figure 4.13 Typical transmission spectra for the direct and coupled arms of the DC based on 8-µm-wide waveguides with a separation of 6 µm and an interaction length of 8 mm.

Using a laser at 1570 nm, the transmission through the direct and coupled arm was measured for DCs with the interaction length changing from 0.1 to 1.5 mm with 0.1 mm step. The dependence of the transmitted power through one of the arms on interaction length was fitted using Eq. [3.11] (Figure 4.14) allowing estimation of the value of the coupling length and the offset, which gives a correction to the nominal interaction length due to the interaction of the modes in the S-bend region. For 8-µm-wide waveguides, the coupling length $L_{\pi/2}$ was estimated to be around 0.8 mm and 1.9 mm for a separation distances of 0 and 4 µm, respectively.

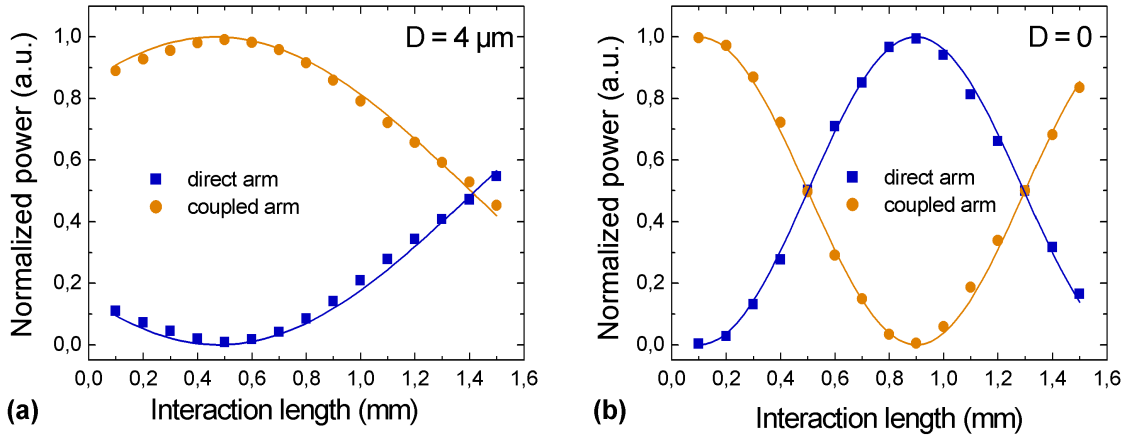

Figure 4.14 Transmitted power through the direct and coupled arms vs. the interaction length for DCs based on 8-µm-wide waveguides with **(a)** 4- and **(b)** 0-µm-separation, *D*. Lines indicate the $\sin^2$ and $\cos^2$ fits (Eq. [3.11]).

Using the effective-refractive-index approach, described in section 3.2, the coupling length for a DC with 0-µm-separated waveguides was estimated by calculating the beat length between the first two (lowest-order) modes (Eq. [3.9]) of the composite waveguide structure. For a 15-nm-thick and 16-µm-wide waveguide, which corresponds to the DC based on 8-µm-wide stripes with 0-µm-separation, the beat length was calculated to be 0.91 mm. This is close to the experimentally obtained value of 0.8 mm. For the first two modes of the structure, consisting of two 8-µm-wide waveguides with 4-µm separation, the beat (coupling) length was found to be 1.93 mm matching the experimental value of 1.9 mm.

At the nominal-zero-interaction length, power at the coupled arm was higher than in the direct arm (Figure 4.14). The offset value shows that the interaction between two waveguides also occurs outside the parallel section. In the case of 0-µm-separation between the waveguides, the offset value obtained from the sin^2 fit was 1.3 mm, while for the 8-µm-separated waveguides, this distance was about 0.7 mm (Figure 4.14). These DCs were composed of 2.5-mm-long cosine-bends with an offset of 48 µm. The results for the offsets showed that the interaction of the modes started in the area of the S-bend when the distance between the waveguide centers was approximately twice as large as that in the nominal interaction region. This effect has to be taking into account when designing waveguide components containing directional coupler devices.

4.7 Conclusions

"Would you tell me, please, which way I ought to
go from here?" "That depends a good deal on
where you want to get to," said the Cat.
Lewis Carroll, "Alice's Adventures in Wonderland"

Polymer-based LR-SPP stripe waveguide components constitute a new alternative for integrated optical circuits. In this work, efficient guiding of light along thin gold stripes embedded in polymer via excitation of LR-SPPs has been demonstrated at telecom wavelengths. A propagation loss of ~ 6 dB/cm and a coupling loss of ~ 0.5 dB (per facet) have been obtained for 15-nm-thick *stripe waveguides* of 8 mm width at ~ 1550 nm.

The performance of *S-bends* has been studied and S-bend loss of less than 3 dB has been obtained for a 4.5-mm-long S-bend with a 200-µm-offset. A *Y-splitter* that can be used as a symmetrical power divider or 3-dB coupler has also been realized. *MMI devices* based on LR-SPP stripe waveguides have been demonstrated opening up the possibility of designing different routing and coupling components as well as wavelength demultiplexing elements based on LR-SPP MMIs.

Directional couplers based on 15-nm-thick and 8-µm-wide stripe waveguides have also been investigated, and coupling lengths of 1.9 and 0.8 mm have been found for directional couplers with 4- and 0-µm-separated waveguides, respectively, implying that quite short (a few mm) functional components (splitters, couplers, etc.) can be realized. All LR-SPP waveguide components have been modeled using the effective-refractive-index approach, and good agreement with the experimental results has been obtained.

Further investigations in the area of waveguide devices utilizing LR-SPP propagation are to be conducted, aiming at demonstrating the advantages in exploitation of the LR-SPP stripe waveguide components in specific areas of integrated optics.

5 Propagation of Long-Range Surface Plasmon Polaritons in Photonic Crystal Structures

Alice laughed. "There's no use trying," she said: "one CAN'T believe impossible things." "I dare say you haven't had much practice," said the Queen. "When I was your age, I always did it for half-an-hour a day. Why, sometimes I've believed as many as six impossible things before breakfast."

Lewis Carroll, "Through the Looking Glass"

This chapter aims at presenting the general concept of photonic crystals and its implementation for guiding of long-range surface plasmon polaritons. The chapter starts by an introduction where the origin of the photonic band gap as well as different types of photonic crystals are described. Then planar photonic crystals are presented as an example of a successful approach to photonic crystal realization. Thereafter, a promising idea of combining photonic crystal and surface-plasmon-polaritons is discussed.

The chapter continues with a short overview of different manufacturing techniques for making photonic crystals. Then the fabrication steps for creating photonic crystals in metal-polymer structures, supporting long-range surface plasmon polariton propagation, are described.

In the next section, the experimental arrangements along with the structures of the investigated samples are described. The experimental findings from optical characterization of the LR-SPP guiding in 2D periodic structures are described in sections 5.4-5.7 for different photonic crystal structures without and with linear defects. Experimental investigations of the LR-SPP transmission through and reflection from the PC structures of different lengths, lattice periods and orientations as well as the LR-SPP guiding along line defects in these structures are reported.

The possibilities of achieving a full band gap (in the surface plane) for LR-SPPs as well as usage of weak multiple-scattering effect are discussed in the last section.

5.1 Introduction to photonic crystals

"You may call it 'nonsense' if you like" she said,
"but I've heard nonsense, compared to which that
would be as sensible as a dictionary!"
Lewis Carroll, "Through the Looking Glass"

Today, the term *Photonic Crystal (PC)* or *Photonic Band Gap (PBG)* structure is used to describe a material with periodic modulation of the dielectric constant in one, two or three dimensions. Here, one may argue that structures with a periodicity in one dimension (1D) have been known for ages and that there is nothing special and new about those mirrors and gratings. Furthermore, there is nothing new about making two- (2D) and three-dimensional (3D) periodic structures – these structures can even be found in nature. Then, what is the reason for introducing them again using somewhat strange naming; and what was so revolutionary new in the original ideas of Yablonovitch and John [70,71] in 1987 that boosted this area of research tremendously?

5.1.1 What is a photonic crystal?

Many research groups within advanced optics are eager to find a way to control light propagation on a tiny scale as this would allow dimensions of many waveguide components to shrink considerably, possibly leading to increased fabrication yield and reduced cost as well as new functionalities.

What kind of system could offer control over light propagation? One way is to scale down a conventional index-guiding waveguide and use higher index contrast between waveguide core and cladding. This leads to *photonic wires* that can efficiently guide light around μm-scale bends [72,73].

Another way is quite unusual and arises from the analogy with electronics, where reduction in size of basic components led to massive down-scaling. A typical semiconductor represents a crystal with a periodic arrangement of atoms or molecules. An electron, propagating through the crystal, therefore experiences a periodic potential, which gives rise to the specific conduction properties of the material. In particular, the crystal lattice may introduce gaps in the energy band structure of the crystal, where electrons with certain energies are forbidden to propagate in certain directions due to *Bragg*-like diffraction from the atoms. If the lattice potential is strong enough, the gap might extend to all directions, resulting in a complete band gap (e.g., a gap between conduction and valence energy bands in semiconductors).

Using the semiconductor analogy, one should try to create an optical material that does to photons what semiconductor crystals do to electrons. This means that the new material has to have a periodic structure that would influence the propagation of a photon. The way to create such material is to introduce a periodic modulation of the dielectric constant. In this case, the photonic crystal is build up of dielectric blocks instead of atoms. Here the term *Photonic Crystal (PC)* arises, reflecting the fact that the material is composed of a small, basic building blocks of some dielectric media repeated in space – just like a semiconductor *crystal* – and designed to act on *photons* (now, a common misunderstanding that photonic crystals are necessarily composed of some crystalline material has hopefully been cleared up).

When properly designed, photonic crystals may have *photonic band gaps* – when photons in a certain energy range cannot travel through the crystal in certain directions. For some frequency range, a photonic crystal may reflect light of *any* polarization and at *any* incident angle. In this case the crystal has a *complete photonic band gap*, which means that no light modes at that frequency range can propagate through the crystal. Once one has such a medium, light can be manipulated in many ways, for example, by introducing a channel (tunnel) or a cavity in such structures. Such a channel will guide the light without any deviations, while the cavity will trap the light into a cage, from which the light cannot escape. These possibilities of manipulating light have many potential applications from novel light sources and high-efficiency lasers to optical communications and computing.

In order to develop the photonic band gap concept, one has to go back in time and have look at the well-known 1D periodic structures – standard dielectric mirrors [42]. How do they relate to photonic crystals? For the familiar quarter-wave stack, composed of alternating dielectric layers, there is a certain wavelength at which the incident light is completely reflected. The reason is that for the proper spacing between layers, the light scattering at the multiple interfaces results in destructive interference inside the material. By the photonic-crystal-definition, such multi-layer dielectric structures are 1D photonic crystals. Even though such mirrors are extremely useful, they cannot have a complete band gap. If one imagines a cavity inside such a multi-layered stack, light will always have a possibility to escape perpendicular to the scattering axis. This means that in order to create a 3D material with a complete band gap, one has to arrange (somehow) contrasting dielectrics in a crystal periodic along all three axes.

Even though it seems relatively easy to understand the mechanism that opens up a photonic band gap in the 1D case, it is far from trivial to arrive at the conclusion that the same cancellations could happen for light propagating in *any* directions in a 3D periodic crystal. This effect was first described by Yablonovitch and John [70,71] in 1987, where a 3D photonic crystal was suggested to produce an omni-directional photonic band gap. It is not enough to realize that it is possible – one has to design 3D photonic crystals, which is an even more difficult task. The 3D periodicity of the crystal is not the only one requirement for a complete band gap: The lattice period of the structure,

which has to be of the order of the wavelength, must be chosen properly as well as the contrast in dielectric constants [34].

For those interested in general aspects of photonic crystals, the excellent textbook by Joannopoulos *et al.* [34] might be worth studying. An overview of the photonic-crystal field can also be found in various papers[6] [73-85].

5.1.2 The world of photonic crystals

…"and what is the use of a book,"
thought Alice, "without pictures or conversation?"
Lewis Carroll, "Alice's Adventures in Wonderland"

As it has already been mentioned, the simplest photonic crystals are represented by materials with periodic modulation of the dielectric constant in only one dimension. A general example of a 1D photonic crystal is a structure consisting of alternating dielectric layers with different dielectric constants (Figure 5.1).

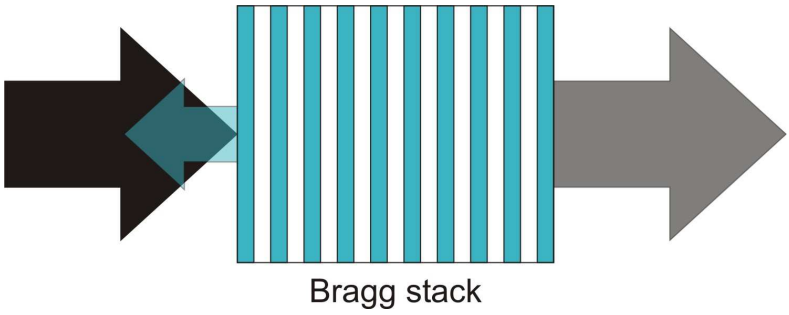

Figure 5.1 Schematic of a one-dimensional photonic crystal: alternating dielectric layers (the Bragg stack).

It is well known that such a layered structure reflects light at certain frequencies and transmits all others – the *Bragg effect* [42]. This effect has been known for a long time and is widely used in many devices, including dielectric mirrors, reflective coatings, fiber Bragg grating and distributed feedback (DFB) lasers, and new applications emerge constantly (Figure 5.2). One of the most frequent examples of 1D photonic crystals is the Bragg grating (or Bragg stack), where the maximum reflection occurs when the optical thickness of the layers equals a quarter of the

[6] Photonic crystals fans are also pointed to the following links http://www.pbglink.com and http://www.elec.gla.ac.uk/groups/opto/photoniccrystal, containing a lot of information about this wide research field. Have a nice around-the-photonic-crystals-world journey.

wavelength. This type of 1D PCs, developed for the LR-SPP-supporting configuration, is described in Chapter 6.

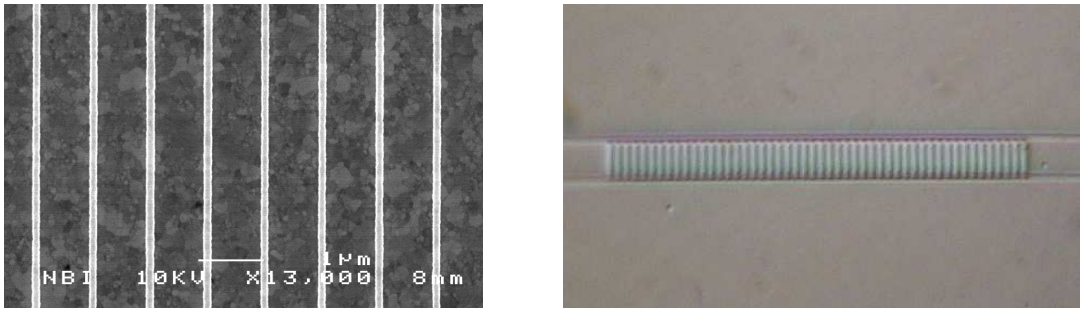

Figure 5.2 Two examples of a one-dimensional photonic crystal (1D PC): **(left)** metallic grating on a gold-on-glass surface supporting surface plasmon polariton propagation and **(right)** AlGaAs-based 1D PC, designed for wavelength conversion, introduced in the slab waveguide.

Although one of the requirements for obtaining a complete band gap is periodicity in all three dimensions, two-dimensional photonic crystals still exhibit photonic band-gap effect and moreover, they offer an easier way to design and fabrication of photonic crystals. 2D PCs are quite easy to derive from the 1D photonic crystal concept – they represent superimposed 1D PCs and form a finite-thickness slab with a 2D periodic pattern (Figure 5.3). Fabricated two-dimensional photonic crystals are shown in Figure 5.4.

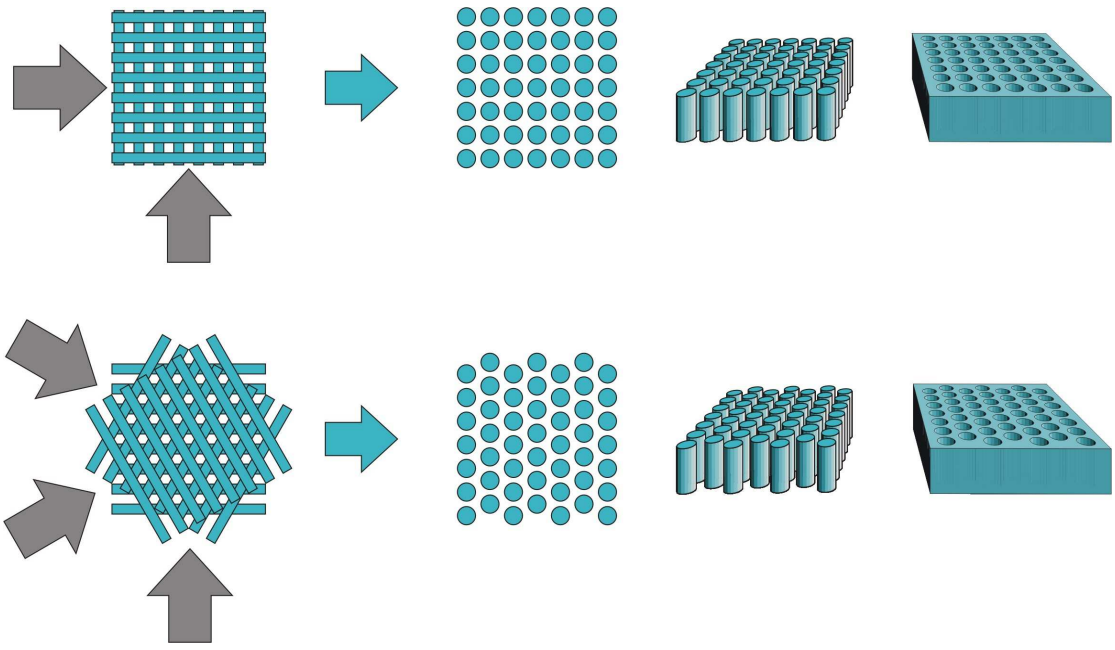

Figure 5.3 Schematic of two-dimensional (2D) photonic crystals: Superimposed gratings leading to 2D PC; and dielectric slabs of a finite thickness with 2D periodic pattern of pillars or holes, arranged in a **(top)** square and **(bottom)** triangular lattice.

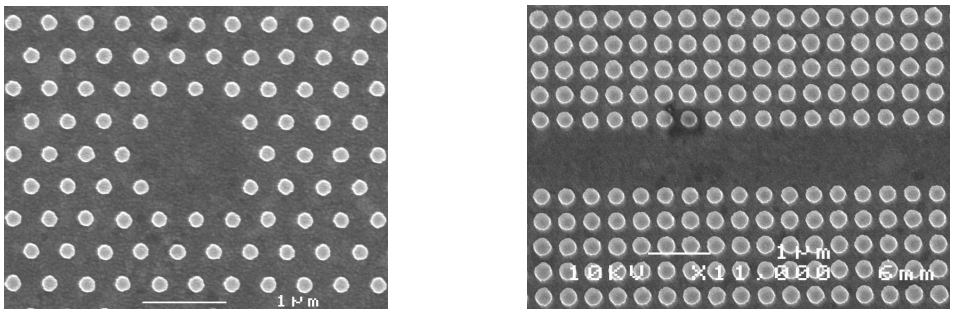

Figure 5.4 Two dimensional (2D) photonic crystals composed of periodic arrays of 50-nm-high gold bumps on a glass substrate covered with 50 nm of gold: **(left)** Triangular lattice with point defect (cavity) and **(right)** square lattice with linear defect (waveguide).

Another example of a 2D photonic crystal can be found among advanced microstructured silica fibers with a periodic array of air holes (2D pattern!) running down the whole fiber length. Unlike all other fibers, which operation is based on index-guidance, such microstructured fiber, when properly designed, can guide light primarily in air by using the PBG effect [82]. An example of a PBG fiber, designed and fabricated at Crystal Fibre A/S, is shown in Figure 5.5.

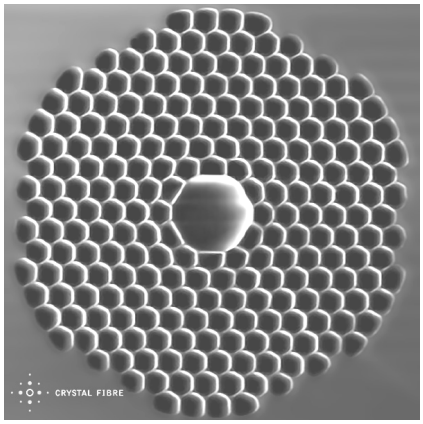

Figure 5.5 SEM picture of a commercially available photonic crystal fiber, which guides light primarily in air by the photonic band gap effect (design, fabrication and scanning electron microscopy by Crystal Fibre A/S).

Even though it is not trivial to fabricate a 3D photonic crystal, impressive progress has been made in the 3D PC field and many interesting designs and realizations have been reported. A detailed overview of different types of 3D photonic crystals may be obtained by studying various papers [78-81,84,86-90]. An example of a 3D photonic crystal, shown in Figure 5.6, again, represents an intuitive design based on 1D PC analogy and looks like a woodpile.

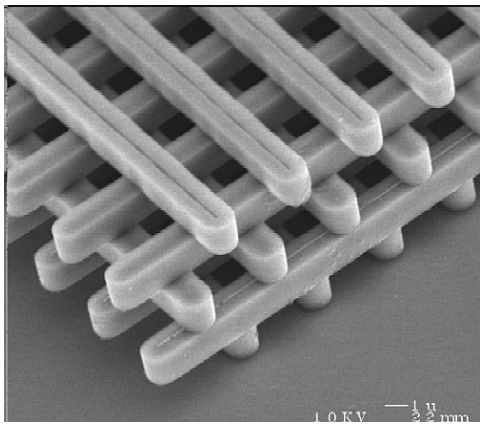

Figure 5.6 Three dimensional (3D) photonic crystal (a woodpile structure) created using a combination of advanced silicon-processing techniques [85].

In relation to photonic crystals and fancy designs, it must be admitted – nature was first. It is a photonic crystal that gives rise to the amazing and beautiful colors of some seashells, butterfly wings, and some minerals. The periodic structures found in those natural systems reflect a specific color resulting in a nice tint, which changes if we look at the object at different angles.

5.1.3 Planar photonic crystal structures

A two-dimensional photonic-crystal can be considered as a single layer or *planar* slice of some hard-to-make 3D periodic structure and is one of the most popular types of 2D PCs. The properties of planar PCs are mainly determined by the refractive index contrast and the fraction of high and low index materials in the lattice as well as the arrangement of the lattice elements. Generally, in order to obtain a large band gap refractive index contrast as high as possible is required; and many different approaches have been suggested for designing planar 2D photonic crystals [75,91-93].

Planar photonic crystals are very attractive both to the theoreticians and engineers due to the simplicity compared to the 3D case, but they also pose a problem – how to keep the light confined inside this slab? There are two possibilities: either the structure is large (compared to the size of the light beam) approaching an infinite 2D structure, or the light is confined to the slab in order to obtain overlap between the propagating mode and the area of periodic lattice. Most of the planar PC structures reported so far utilize *index guiding* as the vertical confinement mechanism (Figure 5.7). Due to the vertical confinement realized in such structures, photonic crystal slabs are sometimes called 2.5-dimensional structures [94].

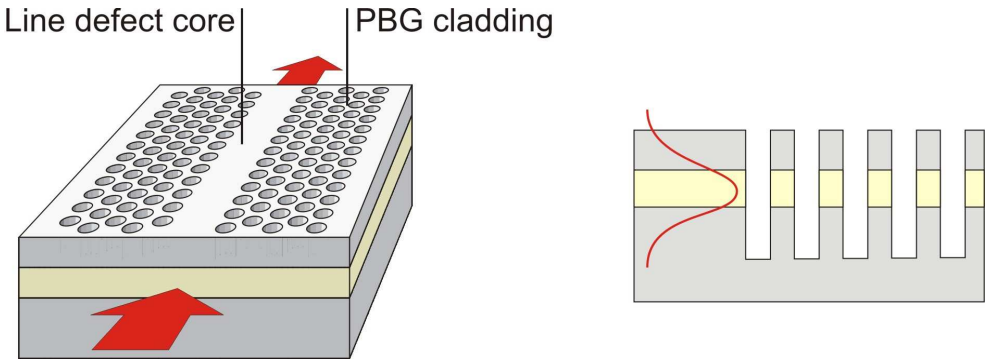

Figure 5.7 (Left) Schematic of the silicon-on-insulator-based planar photonic crystal waveguide, **(right)** utilizing index guiding for the vertical light confinement.

Two widely used types of 2.5D photonic crystals are based on two different material systems, namely, III-V semiconductors (GaAs, InP) and silicon-on-insulator (SOI). Semiconductor materials have the advantage of being an active medium, and, for example, GaAs-based PCs can, in principle, be integrated with light sources. This explains the intense interest in GaAs-based photonic crystals during the last years [77,92,93]. The SOI system offers its natural high refractive index contrast, leading to tighter light confinement in the vertical direction, and its easy integration with the conventional silicon-based microelectronics.

The main activities in this area involve design and realization of SOI-based planar photonic crystal waveguides, schematically shown in Figure 5.7. The 2D photonic crystal in this case is formed by arranging air holes in a triangular lattice in silicon. For a properly chosen ratio between the hole diameter, D, and the lattice constant, Λ, this structure exhibits a photonic band gap for one or both polarizations of the light. Introducing a line defect in such a structure simply by removing a row of air holes and adjusting the width of the waveguide leads to propagating modes with frequencies within the band-gap that are allowed to exist only in the line-defect region [91].

To achieve the vertical confinement, a slab of the 2D silicon-air PC waveguide is surrounded by silica, which has a lower refractive index. Since the propagating mode extends into the silica cladding, the air holes typically continue into the surrounding silica in order to obtain a large overlap between the propagating mode and the area with the refractive index modulation. This was proved to have a positive effect on the waveguiding in photonic crystals [73,92]. Even though a thin silicon membrane suspended in free space would give better light confinement in the vertical direction due to the higher refractive index contrast, silica layer makes the whole structure much more robust and still provides high enough index contrast to ensure efficient index guiding (at least, for proper chosen parameters of the waveguide) [95]. The fabrication procedure for SOI-based planar photonic-crystal structures can be found in Appendix B.

Despite of the fact that one can design 2D photonic crystals and confine the light in the vertical direction by index contrast, light guided in PC waveguide unavoidably sustains *losses*. There are several important loss mechanisms for planar PC waveguides. One of them is the *coupling loss* between a PC area and a conventional waveguide or fiber – depending on what is used to couple light in and out of the PC structure. This includes mode mismatch between modes of the PC waveguide and those of the ridge waveguide (or fiber), which leads to the reflection from the PC area. The coupling loss can be reduced by using tapered waveguides or fibers for in- and out-coupling as well as proper design of the coupling area inside the photonic crystal. *Out-of-plane scattering* losses play an important role even in a perfect photonic crystal – light is scattered out of the plane because there is no vertical confinement inside the holes. Therefore, keeping out-of-plane scattering losses low is a very important issue when designing a photonic crystal. Another mechanism is *scattering* on inhomogeneities, boundary imperfections and surface roughness. To reduce the scattering losses, design and fabrication steps have to be optimized in order to ensure high-quality structures. *Absorption* in the material may also introduce loss. Luckily, both silica and silicon are transparent at the telecom wavelengths of 1.3 μm and 1.55 μm. Another important fact is that, in reality, a photonic crystal is neither perfect nor infinitely wide (typically tens of rows of hole on each side of the waveguide). This may lead to *mode conversion*, which also contributes to the propagation loss inside a PC waveguide. This occurs when a weakly confined mode couples into slab modes, escaping the PC area. The asymmetry of the structure in the vertical direction may lead to additional loss due to the interaction of the TE and TM modes [96]. The processes of mode conversion can, in principle, be controlled both by the design and the fabrication processes.

Since loss is one of the most important characteristics when studying light propagating in photonic crystals, experimental estimation of losses inside a PC area is an essential part of all PC research [92,97-99]. But, due to the inherent small size, it is quite difficult to perform optical characterization of planar photonic crystals [100]. Spectrally resolved transmission and reflection measurements are widely used techniques for optical characterization of PC structures. But since the PC section is short, the contribution from the loss inside the PC area to the total insertion loss can be very small, making data analysis and interpretation of the results quite difficult [97]. Another possibility is to use scanning near-field microscopy to map the propagation of light inside the PC area directly and estimate the loss in straight and bent waveguides [99].

The research area of 2D PC is developing very fast, and at the time of writing, the lowest values for the propagation loss in SOI-based photonic crystal waveguides were reported to be ~ 15 dB/cm [76] while for silicon-membrane-based PC waveguides (membrane suspended in air) a propagation loss of 6 dB/cm was obtained [76].

5.1.4 Photonic crystal structures for surface plasmon polaritons

Due to the inherent vertical confinement of SPPs, it is tempting to try to employ the PC-concept to control the SPP propagation in the surface plane.

For a number of years, surface plasmon polaritons, while interesting in their nature, have to some extent been disregarded as a good waveguiding system due to the small propagation length. However, given the rapid progress in integrated optics, dimensions of future optical components might shrink down to a few hundred micrometers, meaning that the overall SPP propagation loss will be acceptable. From the standpoint of future miniaturization of all-optical components, SPPs may become competitive.

SPPs can be scattered *in the surface plane* through *elastic scattering* by surface defects, meaning that a surface defect can scatter the incident SPP into other SPPs rather than into other modes (Figure 5.8). This in-plane scattering process gives a possibility of employing the photonic crystal concept for these surface waves.

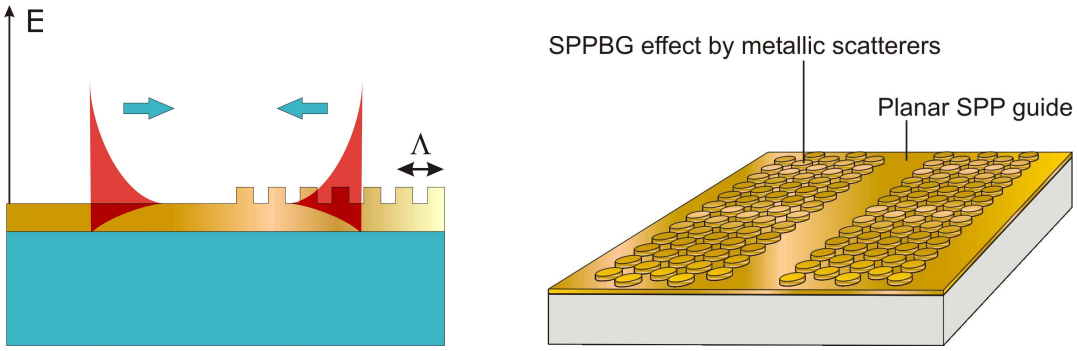

Figure 5.8 (Left) Schematic of the incident and scattered surface plasmon polaritons propagating in **(right)** photonic crystal structure composed of a periodic array of scatterers.

In order to construct a photonic crystal for surface plasmon polaritons, one should arrange surface scatterers in a periodic structure in analogy with the periodic modulation in a PC. When the period of the structure is half that of the effective wavelength of the SPP, scattering may lead to the formation of a standing SPP wave and thus create a band gap (Figure 5.9). For a properly chosen 2D periodic modulation of the surface, SPPs may be prohibited to propagate in any in-plane directions along such corrugated metal surface within a certain interval of wavelengths. In photonic-crystal terminology, the *surface plasmon polariton band gap (SPPBG)* opens up [9,31,36,101].

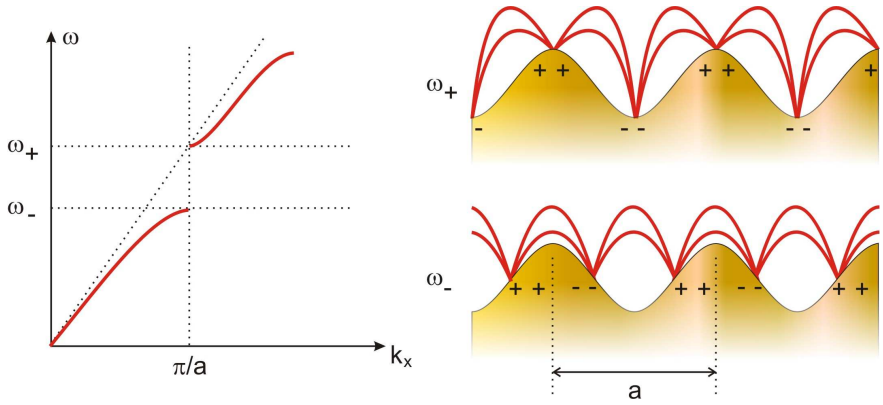

Figure 5.9 (Left) Surface plasmon polariton dispersion diagram showing a band gap where no SPP modes can propagate [9]. **(Right)** The two band edges ω_- and ω_+ correspond to two standing wave solutions for an SPPBG structure with the period a [9].

In order to have an efficient *in-plane* scattering, which should lead to the PBG effect, it is not enough just to place scatterers close to the surface. One should also make sure that the SPP interacts with many scatterers on its way so that coherent scattering takes place. If the scatterers are too strong, then the propagating SPP will only interact with few of them making the effect of the coherent scattering unattainable. The strength of a scatterer is mostly determined by the frequency (or rather how close it is to the plasmon-resonance frequency) and the scatterer itself (its size, shape and material). However, to estimate, how efficient the SPP-scatterer interaction is and what the main parameters to consider are, is not a very easy task [38,39,102].

Even though one deals with 2D surface waves, there is no way to get the pure-2D-world for free – there are some things to remember when designing efficient SPPBG structures. Although the most important task is to ensure efficient in-plane scattering, one should keep in mind that two scattering processes, namely elastic and *inelastic*, always occur at the same time. Inelastic scattering, when the scattered *out-of-plane* wave propagates in air away from the surface, is, unfortunately, always present and may, at some point, become dominating, effectively introducing additional loss to the SPP propagation.

The SPPBG effect was first observed by performing angular and wavelength resolved measurements of the reflectivity of metal films periodically corrugated in one [35] and two [36] dimensions. Experimental investigations of the SPPBG structures [31-33] stimulated theoretical considerations of the SPPBG effect [37,103] and the corresponding waveguiding characteristics [38,39] that confirmed the feasibility of efficient SPP manipulation using periodic arrays of surface scatterers.

The results reported by Bozhevolnyi *et al.* [31] can be mentioned as an example of a successful SPP photonic-crystal system. The SPPBG effect as well as efficient guiding along straight and bent line defects in a periodically corrugated gold film surface with 40~50-nm-high

gold scatterers with a diameter from 150 to 200 nm arranged on a 400~500-nm-period triangular lattice were successfully demonstrated by using scanning near-field optical microscopy [31-33,101].

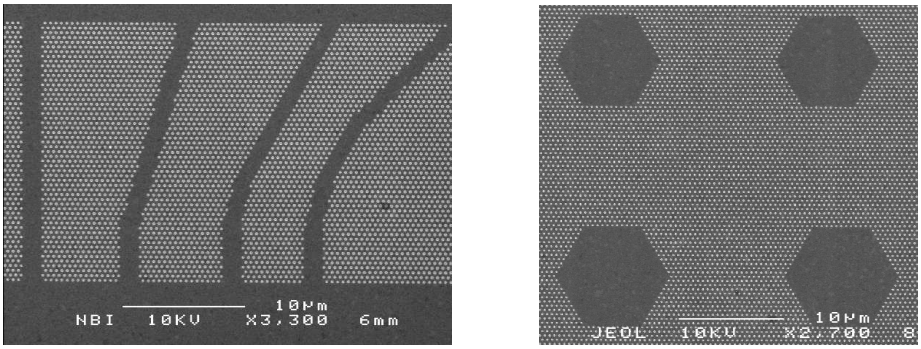

Figure 5.10 SEM images of photonic crystals (PCs) for surface plasmon polaritons with **(left)** linear (waveguides) and **(right)** point (cavities) defects. PCs are composed of periodic arrays of 50-nm-high gold bumps on a glass substrate covered with 50 nm of gold.

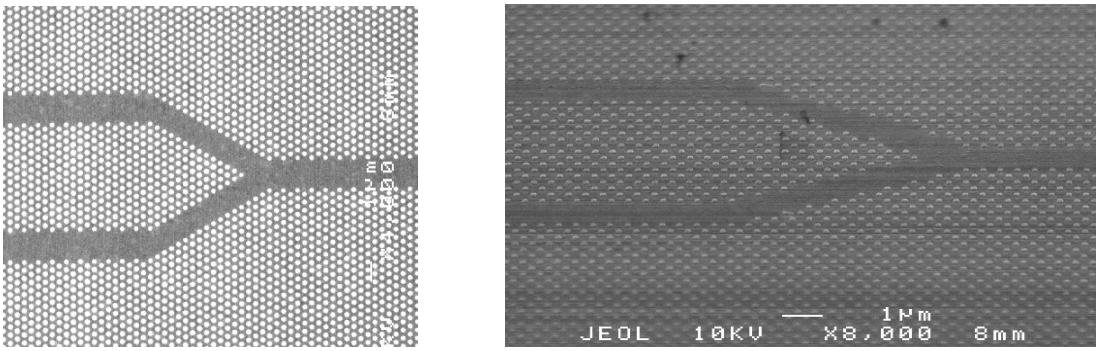

Figure 5.11 (Left) Top and **(right)** 30-degree SEM images of a Y-splitter in the photonic crystal for surface plasmon polaritons. PC is composed of periodic arrays of 45-nm-high gold bumps on a glass substrate covered with 50 nm of gold.

A few examples of photonic crystals for SPPs, including straight and bent waveguides, cavities and Y-splitters, are shown in Figure 5.10 and Figure 5.11. For those interested in fabrication processes, the procedure for making SPPBG structures can be found in Appendix C. Using scanning near-field microscopy, SPP propagation in fabricated SPPBG structures was investigated in the wavelengths range of 720-830 nm [31]. At 740 nm the bend loss was estimated to be below 2 and 10 dB for bend angles 15° and 30° respectively [32]. Efficient splitting and combining of two SPPBG line-defects modes were also demonstrated for a 20-μm-long Y-splitter [32,101].

5.1.5 Photonic crystal structures for long-range surface plasmon polaritons

Long-range surface plasmon polaritons, being a subset of SPPs, offer some advantages compared to normal SPPs, including low propagation loss and compatibility with standard fiber optics. Therefore, it seems natural to try to extend the approach used in realization of the SPPBG structures for the configurations supporting the LR-SPP propagation, e.g. to realize photonic crystal structures for LR-SPPs.

The configuration studied is based on a periodic array of metal bumps (cylinders) protruding symmetrically above and below a metal film supporting the LR-SPP propagation (Figure 5.12). The expectation is that symmetric (with respect to the metal film) bumps should scatter the incident LR-SPP back into LR-SPPs rather than into asymmetric and high-loss (short-range) SPP modes. Furthermore, it is the assumption that the out-of-plane scattering should be small compared to the in-plane scattering.

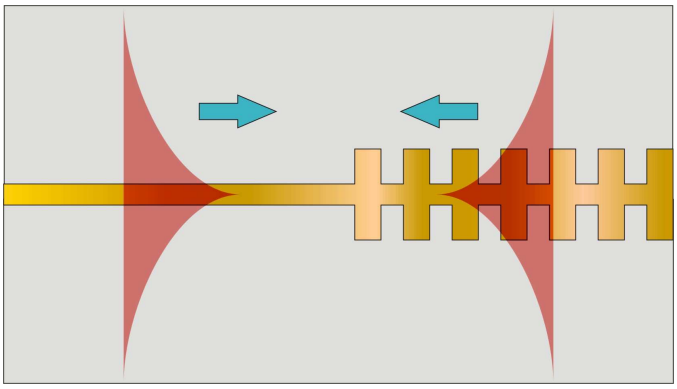

Figure 5.12 Schematic of the photonic crystal in configuration supporting long-range surface plasmon-polariton propagation.

Propagation of long-range surface plasmon polaritons in photonic crystals has never been investigated before. While this work presents the first experimental observation of LR-SPPs propagation in periodic structures [104,105], full theoretical modeling of photonic crystals structures for LR-SPPs will be published elsewhere [104-106].

5.2 Fabrication of photonic crystals for LR-SPPs

5.2.1 An overview of photonic-crystal-fabrication methods

Everything one man can imagine
another man can make it real.
Jules Verne

There is a vast variety of photonic crystals fabrication methods ranging from fabrication procedures adopted from the silicon-based microelectronics industry to self-organized photonic crystals [75]. An impressive progress has been made with photonic crystals created using lithographical and etching techniques [77,83,93,107,108], electrochemistry [107], membranes [109], oxidation, growth [110] and embossing techniques [111], the fiber stack-and-pull process [82] and self-organization (especially for so-called synthetic opals) [81].

Methods for fabricating photonic crystals that are periodic in only one direction have been known and improving for many decades. Different techniques such as standard and deep-UV lithography, crystal growth, sputtering, and UV-writing have been exploited [112].

For 2D photonic crystal realization, a great number of manufacturing methods are being investigated, mainly based on lithography-etching techniques for planar photonic crystal fabrication [77,93,108] and fiber drawing technology for photonic crystal fiber production [82].

Nowadays, patterning of planar 2D photonic crystals is mainly realized by lithographic means. Considering the resolution of the standard UV photolithography of the order of 1 μm, this technique cannot be employed for fabricating photonic crystals with a lattice constant ranging from 150 to 800 nm. Depending on the desirable smallest-feature size, many different lithographic techniques have been exploited such as deep UV lithography [108], X-ray lithography [113], electron-beam lithography [77,114] and holography [115].

Electron-beam lithography is one of the most popular alternatives, which is today used by many research groups for realization of a variety of patterns. However, this technique is a serial process, where each part of the pattern is written sequentially, and it is, therefore, time consuming. On the other hand, it is a very useful technique at the development stage since every time, a new or modified pattern can be generated. Electron-beam lithography was also exploited in this work and is briefly discussed in Appendix A.

Compared to electron-beam lithography, deep UV or X-ray lithography has the advantage of being a parallel process, as it allows the whole structure to be written simultaneously, and lots of identical patterns can be created over a short time after the mask has been fabricated. However, a

new mask has to be fabricated every time one needs to make changes to the design. Considering a future commercialized manufacture of 2D photonic crystals, deep UV lithography most likely holds the first place as a possible commercial fabrication technique. Today, deep UV lithography has proven to be a viable technique for the manufacturing of photonic crystal structures and components [108], but the fabrication procedure is still to be developed and optimized.

Holography is also a well-established technique for generating patterns in polymers and has been employed successfully in the realization of 2D PC structures. This technique, in fact, has been used for quite some time to generate 2D periodic patterns in different structures. However, holography has severe limitation when intentional defects have to be introduced into the regular lattice, making it difficult to fabricate, e.g., PC waveguides and microcavities using this technique. Three-dimensional photonic crystals, while theoretically appealing, are very hard to make. Nevertheless, quite a number of different fabrication methods for 3D PC structures have been proposed and successfully realized. The first 3D photonic crystal at microwave frequencies, *Yablonovite* [86], was fabricated by drilling specially arranged air channels in a slab of dielectric. However, this structure turned out to be quite difficult to realize for 1.5µm operating wavelength [79]. Among other promising methods for making 3D PC, there are micromechanical fabrication of layer-by-layer periodic structures [78,84,90], made by stacking thin silicon pieces, and synthetic self-organized photonic crystals, notably opals [81,88]. Other new approaches exploited by different research groups are 3D metallodielectric photonic crystals [80] and photonic crystals with self-aligned sputtered Si and SiO_2 layers [87].

5.2.2 Fabrication of photonic crystal structures for LR-SPPs

The processing steps for manufacturing of photonic crystals for LR-SPPs are presented in Figure 5.13.

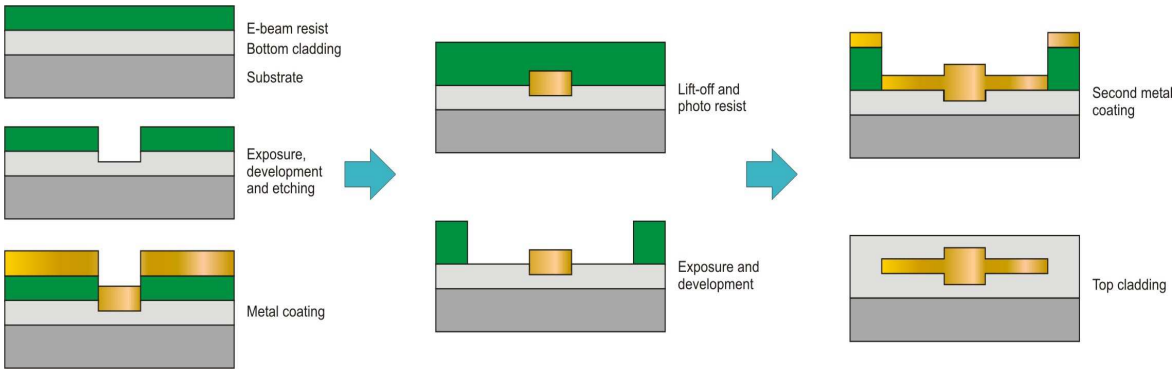

Figure 5.13 Schematics of the processing steps for photonic crystals for long-range surface plasmon polaritons.

To fabricate periodic structures, a silicon substrate (4" or 6") was first spin-coated with a 15-µm-thick BCB polymer layer followed by soft baking of the polymer. Prior to the electron-beam lithography, which was performed at Chalmers University, the wafer with polymer cladding was coated with positive electron-beam ZEP-520 resist following by resist pre-baking. The resist thickness was approximately 300 nm. Then the designed hole pattern was transferred into the resist by EBL exposure and development processes.

In order to transfer the pattern into the BCB layer, a reactive ion etching technique was used. After RIE of the BCB layer with the electron-beam resist as a mask, bumps were formed by metal (gold) deposition and lift-off. Since vertical symmetry of the structure is very important for the LR-SPP propagation [13] and scattering, the etch depth was carefully measured using an atomic force microscope. This allowed to choose the appropriate gold thickness to obtain bumps placed symmetrically above and below the LR-SPP propagation plane (Figure 5.14). The bumps, with a diameter of 200~300 nm, were arranged in a triangular lattice with periods from 500 nm to 600 nm. The lift-off process after the metal deposition forming gold bumps turned out to be the most crucial processing step – in cases where the initial resist thickness was too low, the lift-off process was quite difficult and time consuming and resulted in some of the deposited gold bumps being removed (Figure 5.14).

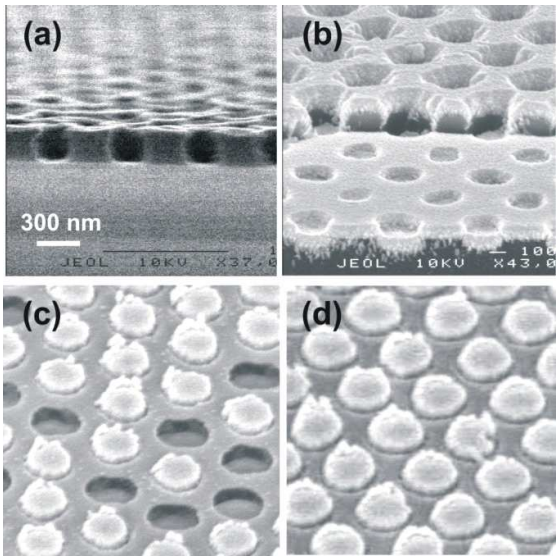

Figure 5.14 SEM pictures of step-by-step processing of photonic crystal: **(a)** pattern in the electron-beam resist deposited on the polymer (BCB) layer, **(b)** holes in BCB made by RIE using the resist as a mask (the resist is not removed further away on the picture) and covered with a thick gold film, surface after lift-off: **(c)** gold bumps at and holes in BCB, the latter are in places where bumps have fallen off during lift-off; **(d)** a successfully fabricated photonic crystal structure (before deposition of a thin gold layer supporting LR-SPPs and the top BCB layer). Fabrication and scanning electron microscopy by Kristjan Leosson.

After fabricating periodic structures of bumps, LR-SPP stripe waveguides, aligned with respect to the PC structures, were patterned using standard UV lithography. A second metallization

and lift-off was used to pattern gold stripes, being 10-15 nm in thickness and, typically, 8 µm in width, which ensured low-loss LR-SPP propagation and efficient radiation (in/out) coupling with single-mode fibers [16]. The last processing step consisted of spin-coating the wafer with another 15-µm-thick BCB layer. After final polymer curing, the wafer was cut into individual samples.

The investigated samples contained blocks of periodic structures having different lattices (triangular and square), lattice constants and lengths. In case of the triangular lattice, structures with both ΓK and ΓM direction of the irreducible Brillouin zone of the lattice [8] (directions along which the excited LR-SPP is supposed to propagate) were fabricated (Figure 5.15). The bump height for different samples varied from 80 nm to 200 nm on each side of the film.

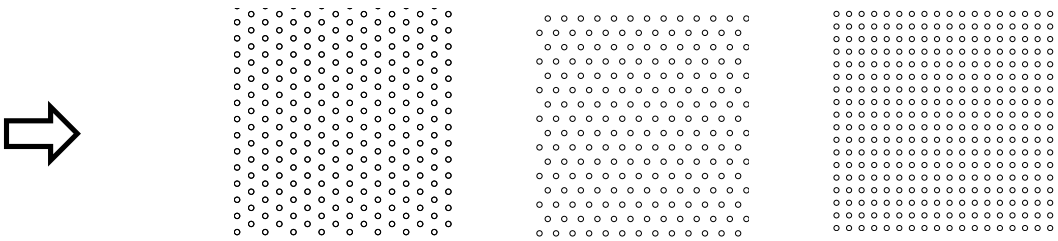

Figure 5.15 Schematic of different crystal lattices and orientations: triangular lattice having **(left)** ΓK and **(center)** ΓM orientations and **(right)** square lattice.

The channels in periodic structures (Figure 5.16) were introduced by missing rows of bumps and had different widths (from approximately 1 µm to 8 µm) and lengths (~ 30, 150, 300, and 600 µm). PC blocks without line defects (channels) were placed so that the 8-µm-wide LR-SPP waveguides crossed the blocks approximately in the middle. For the channels, the width of the gold stripes was increased to 50 µm in the area of the PC structure, in order to exclude the influence of stripe width on the in-plane confinement of the LR-SPP within the line defect.

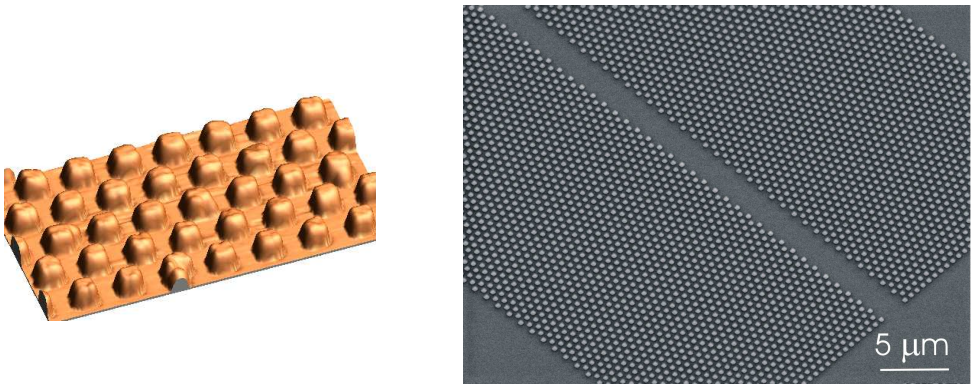

Figure 5.16 **(Left)** AFM scan of metal bumps together with **(right)** SEM picture of a PC waveguide created by removing 7 rows of bumps in a 570-nm-period structure. The bump height is ~ 150 nm on each side of the waveguide plane. Fabrication, atomic force microscopy and scanning electron microscopy by Kristjan Leosson.

5.3 Experimental arrangement

For optical characterization of the fabricated periodic structures, standard spectrally resolved transmission and reflection measurements were performed. The schematic of the experimental setup is shown in Figure 5.17. The light from a broadband source consisting of two multiplexed EE-LED diodes (1310 nm and 1550 nm) was sent through a polarization controller and launched into the LR-SPP waveguide via butt-coupling from a polarization-maintaining fiber. LR-SPP stripe waveguides were aligned with the channels so that LR-SPPs were coupled directly from a stripe waveguide to a PC area and back to a stripe waveguide after propagating through the PC structure (Figure 5.18). 1 km of coiled standard single mode fiber was used as output-coupling fiber in order to strip off all light coupled into the fiber cladding. Index matching gel was used to decrease the reflection at the sample edges. The output signal was detected by an optical spectrum analyzer.

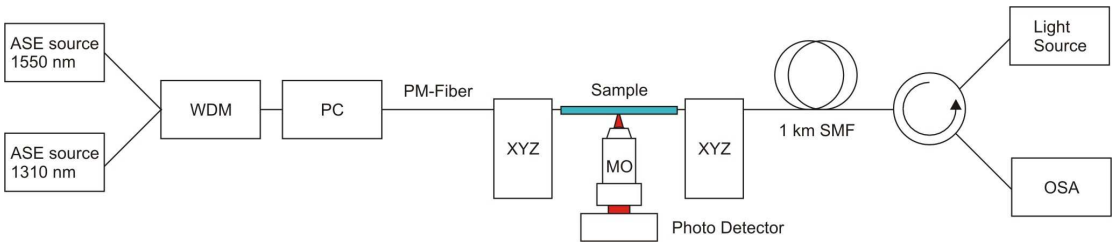

Figure 5.17 The layout of the transmission measurements setup for optical characterization of PC structures.

Alignment was a very critical issue for the optical characterization of the structures. The transmission through long blocks or channels could, in principle, be lower or at the same level as the background light propagating in the cladding, making the conventional active alignment unsuitable. Instead, an alignment was realized using the fact that the amount of light scattered out of the plane while propagating through the PC structure is much larger than the light scattered out from the cladding light. By maximizing the amount of scattered light in the direction perpendicular to the waveguide plane it was possible to achieve good alignment of the fibres with the waveguide containing the PC structure. In experiments, the adjustment of the input- and output-coupling fibers with respect to the waveguide was accomplished separately (with the use of a circulator for the output fiber alignment) by maximizing the amount of light scattered by the PC structure in the direction perpendicular to the waveguide plane with the help of a microscope arrangement. A typical image corresponding to the condition when the input fiber was aligned to the stripe waveguide is presented in Figure 5.19, featuring the scattered light from the PC structure.

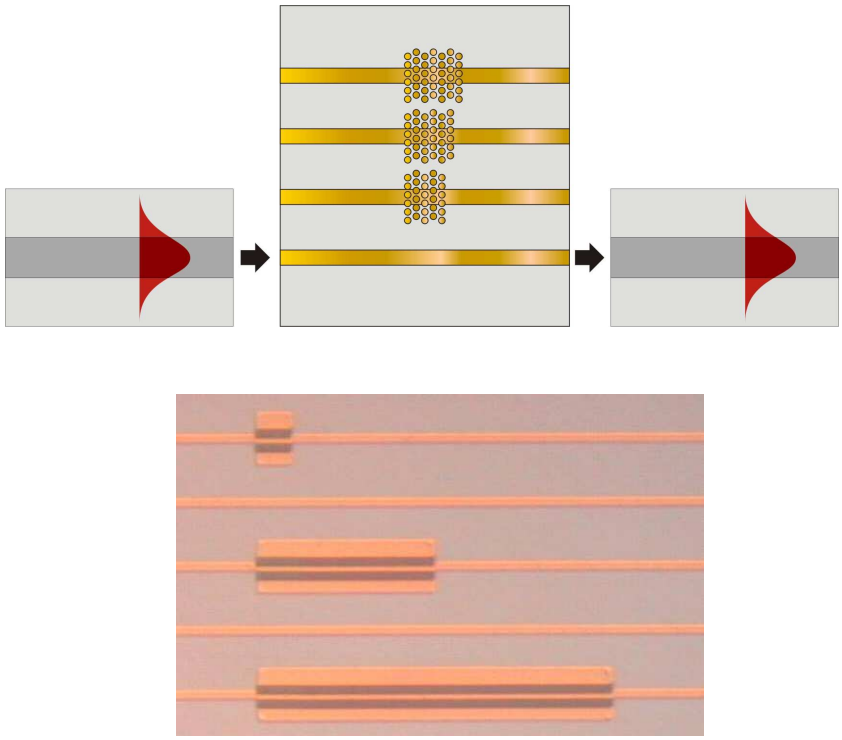

Figure 5.18 (Top) Schematic of the sample structure together with **(bottom)** a microscope image of the PC waveguides of different lengths aligned with stripe waveguides.

Having the input and output fibers aligned to a stripe waveguide, the transmission spectrum was recorded in the wavelength range from 1225 to 1675 nm with a resolution of 5-10 nm and high sensitivity (-80 dBm). All measured transmission spectra through PC structures were normalized to the transmission through a straight stripe waveguide that did not contain a PC area, yielding a loss spectrum including only the insertion loss of the PC structure. For the reflection measurements the resolution was set to 1-0.5 nm to resolve a back-reflection peak from the PC structure and all reflection spectra from the investigated structures were normalized to the reflection from the silicon substrate.

Images obtained by placing a high-resolution microscope (×40 and ×100 magnification) and an infrared camera over the top of the sample allowed the out-of-plane scattering to be visualized at different wavelengths for the LR-SPPs propagating through PC structures. Mode profile measurements on truncated channels were also performed as part of the optical characterization of the PC structures. The intensity distributions were imaged on an infrared camera and compared with an output mode from a standard single mode fiber with a known mode size.

5.4 Propagation through photonic crystals

I couldn't reduce it to the freshman level.
That means we really don't understand it.
Richard Feynman

5.4.1 Transmission and reflection

An optical microscope image showing a top view of a short PC block together with a section of the corresponding mask design is presented in Figure 5.19. The detail of the mask design shows a stripe waveguide entering a PC area formed by an array of bumps arranged in a *triangular lattice* with a period of 570 nm (ΓK orientation). Microscope images of an 8-µm-wide stripe waveguide "running through" a 12-µm-long and approximately 50-µm-wide block along with images taken with the camera positioned over the top of the sample, at the resonance wavelength 1512 nm and at the wavelength 1600 nm away from the resonance are shown in Figure 5.19 (c) and (d). At the resonance wavelength 1512 nm, light propagating inside the PC blocks makes the structure "light up" all the way to the end. For the wavelength outside the resonance (1600 nm) the light scattering mainly occurs at the entrance of the PC area. Similar wavelength-dependent scattering was also shown by theoretical modeling [104].

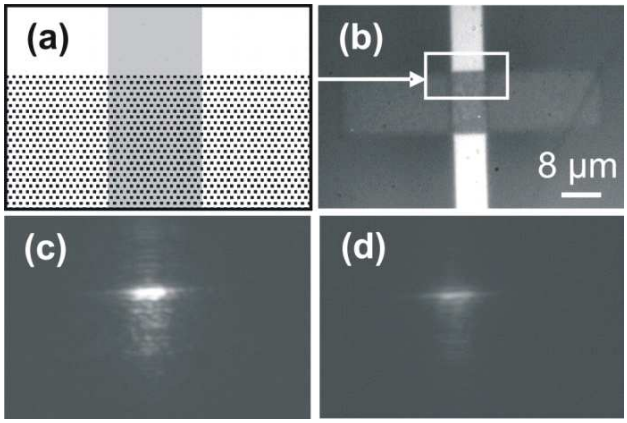

Figure 5.19 (a) Detail of the mask design showing a 8-µm-wide stripe waveguide entering a PC area in the ΓK direction of the 570-nm-period triangular lattice along with **(b)** optical microscope image showing the top view of a 12-µm-long and 50-µm-wide PC block together with the 8-µm-wide stripe waveguide. Lower figures show the same top view (without external illumination) when the LR-SPP is excited **(c)** at the resonance wavelength 1512 nm and **(d)** at 1600 nm. Total bump height is 300 nm.

Samples containing blocks of different lengths and lattice periods were characterized by measuring transmission and reflection spectra. Typical transmission spectra for blocks of different

lengths are presented in Figure 5.20 (left graphs) exhibiting relatively high transmission through a 192-μm-long PC block (around -10 dB at 1550 nm) indicating a large penetration depth into the PC structure. All transmission spectra featured characteristic reproducible peaks (at a resonance wavelength) and lower transmission levels for shorter wavelengths. This can be partly explained by the increase of the out-of-plane scattering.

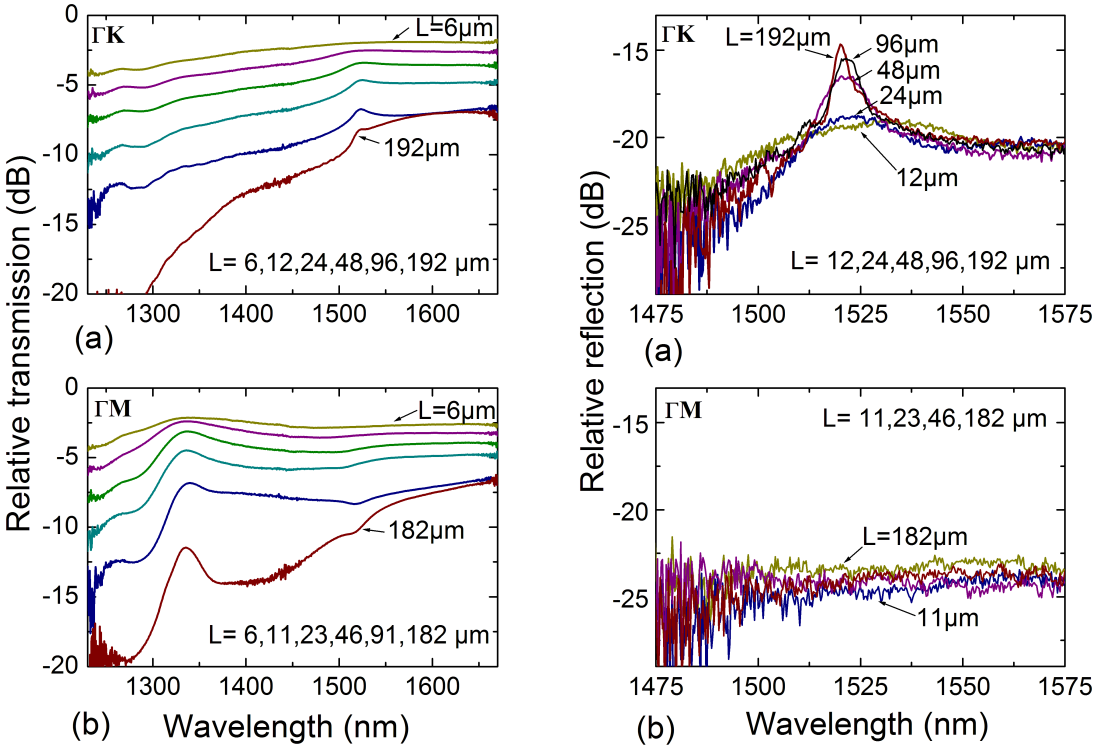

Figure 5.20 Typical **(left)** transmission and **(right)** reflection spectra for PC blocks of different lengths for **(a)** ΓK and **(b)** ΓM orientations of 570-nm-period triangular lattice. Total bump height is 300 nm.

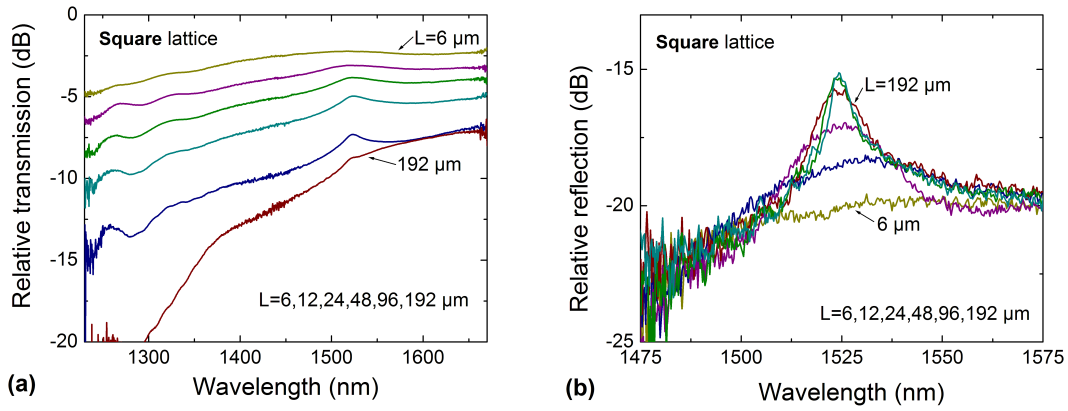

Figure 5.21 Typical **(a)** transmission through and **(b)** reflection from PC blocks of different lengths for 500-nm-period lattice. Total bump height is 300 nm.

Samples containing PC areas formed by an array of bumps arranged in a *square lattice*, were also characterized and exhibited almost the same behavior in transmission measurements (Figure 5.21 (a)).

The peak in the transmission was found to scale in accordance with the lattice constant as presented in Figure 5.22 (a) showing the results for the ΓK orientation.

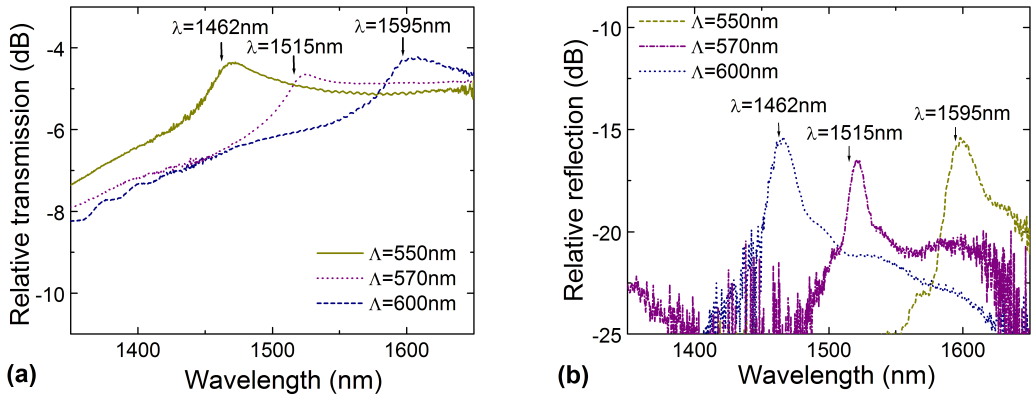

Figure 5.22 (a) Transmission spectra through a 24-μm-long block and **(b)** reflection spectra for a 192-μm-long block for triangular lattices of different periods, Λ, (ΓK orientation) together with the positions of the peaks estimated from the Bragg grating arguments. Total bump height is 200 nm.

Reflection measurements were performed for the blocks of different lengths in order to estimate the penetration depth of the LR-SPPs into the PC structures. Typical reflection spectra from the PC blocks are presented in Figure 5.20 (right graphs). A strong back-reflection from the PC structure is observed for the ΓK orientation at the wavelength corresponding to the Bragg condition (Eq. [4.1]) indicating a high cross-section for the LR-SPP-to-LR-SPP scattering for this orientation.

The positions of the reflection peaks can be estimated from the Bragg grating arguments [34] (see Chapter 6) giving the peak position λ_{max} at wavelengths:

$$\lambda_{max} = \sqrt{3} \cdot n \cdot \Lambda \quad \text{for the triangular lattice of ΓK orientation} \qquad [4.1]$$

$$\lambda_{max} = 1.5 \cdot n \cdot \Lambda \quad \text{for the triangular lattice of ΓM orientation} \qquad [4.2]$$

$$\lambda_{max} = 2 \cdot n \cdot \Lambda \quad \text{for the square lattice} \qquad [4.3]$$

where n = 1.535 is the refractive index of BCB polymer at 1550 nm and Λ is the lattice period. These estimations for the lattice periods 550 nm, 570 nm and 600 nm are also given in Figure 5.22 as a comparison with the actual positions of the transmission/reflection peaks.

For the ΓK orientation, the reflection spectra from the PC blocks behaved similar to normal reflecting Bragg gratings [34] in the sense that a gradual increase in strength and decrease in width of the reflection peak was observed with the increasing structure length (top left graph in Figure

5.20). Consequently, the LR-SPP penetration depth was estimated to be ~ 100 μm at the resonance wavelength. Similar investigations, based on reflection spectra analysis, were also carried out for the square lattice to study the influence of the structure on the reflection properties of PC blocks. The overall behavior was found to be the same with slightly lower penetration depth, consistent with the fact that for the square lattice the number of bumps per one "reflecting line" is larger than for the triangular lattice. The estimates of the penetration depth for triangular and square lattices are presented in Figure 5.23. In the followings, only structures based on the triangular lattice are investigated.

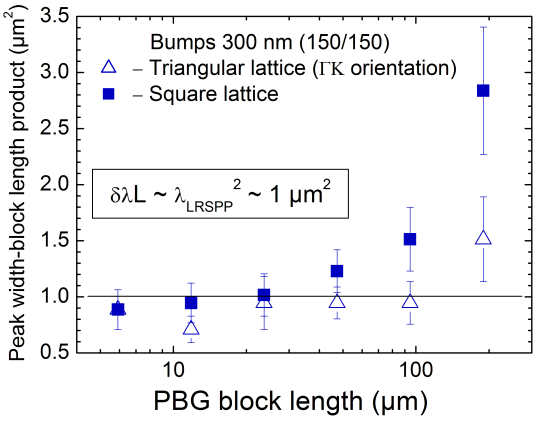

Figure 5.23 Dependence of the product between the reflection peak width and the PC block length on the PC structure length for different lattices.

For LR-SPP propagation along the ΓM orientation, reflection is in general not very strong since, in this case, most of the reflected light at the wavelength corresponding to the Bragg condition is not reflected in the back-direction and hence can not be picked up by the LR-SPP stripe waveguide [104]. Typical reflection spectra from the blocks for the ΓM orientation are presented in Figure 5.20 (low right graph), where the level of the reflected signal was lower than in the case of the reflection measurements performed for the ΓK orientation. The same behavior was found in the wavelength range from 1250 nm to 1450 nm with no back-reflection peak observed at the resonance wavelength around 1310 nm.

Attention should be drawn to the peculiar fact that for the same structure, a peak in both the transmission and reflection spectra occurred at approximately the same wavelength (Figure 5.22). This behavior is not typical for the usual Bragg-like effect – normally the position of the reflection peak coincides (more or less precisely) with the position of a dip in the transmission, confirming the intuitive notion that what-is-reflected-is-not-transmitted and what-is-transmitted-is-not-reflected. This is true in the ideal world, when only in-plane scattering takes place. In the investigated structures, out-of-plane scattering is partly responsible for the observed "counter-intuitive" behavior at the Bragg wavelength, when the effect of coherent scattering is the strongest,

only a small fraction the light is scattered out of the plane and almost all of the scattered light is going back into LR-SPPs. The situation is different in case of wavelengths away from the Bragg resonance, where larger fractions of light are lost due to out-of-plane scattering, reducing the total transmission-plus-reflection power. This means that in order to operate in the Bragg-like regime, one has to ensure the efficient in-plane scattering and weak scattering out of the plane. In this case, a dip appears in the transmission as it is reported in Chapter 6.

In a more illustrative way, the loss, measured in the experiments, has three main contributions:

- Out-of-plane scattering (that can, in principle, be coupled to the waveguide again – see the next section)
- In-plane-scattering (which is not picked up by a stripe waveguide)
- Absorption in metal

The second mechanism can be illustrated using reflection spectra for the ΓM orientation. In this case, the total measured power was found to be smaller than in the case of the ΓK orientation, which is not only due to the out-of-plane scattering but also due to the in-plane scattering into other directions than that corresponding to the propagation of LR-SPP stripe modes. Out-of-plane scattering and absorption in metal are responsible for the transmission drop toward shorter wavelengths. Even though the spectra were normalized to the transmission through a stripe waveguide (and thereby normalized to the absorption loss for a stripe waveguide), the absorption in metal still contributes to the total loss due to higher volume of metal in case of bumps.

The observed behavior for the transmission and reflection spectra is a result of the interplay of different scattering and other loss mechanisms and was fully confirmed by the theoretical modeling [104].

5.4.2 Loss dependence on the structure length

When dealing with PC structures, one should expect an exponential decay of the field into the structure, which means that the loss dependence (in dB) on the structure length should be linear. However, for all investigated structures, regardless of the structure type (lattice or orientation), the length dependence of the loss was found to be sublinear showing some "rolling off" tendency – the transmission through the structures with increasing lengths was measured to be higher than expected (Figure 5.24). This *saturation tendency* was stronger for longer wavelengths and, for example, at 1600 nm the transmission through the longest PC block (192-µm-long) was as high as for a 96-µm-long structure (Figure 5.20, Figure 5.21).

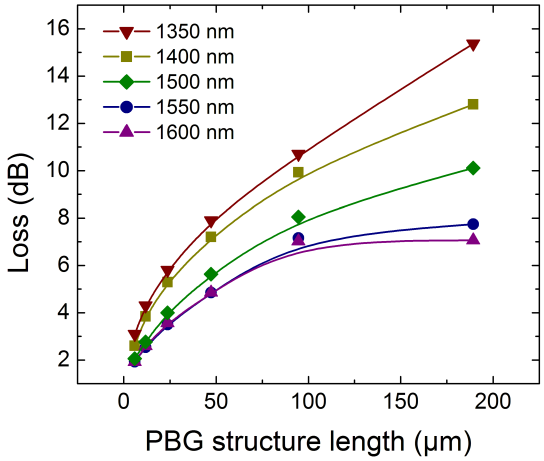

Figure 5.24 Dependence of the loss on the block length for 570-nm-period triangular lattice (ΓK direction). Total bump height is 300 nm.

This sublinear loss dependence on the structure length can be attributed to light being scattered out of plane, reflected from the silicon-BCB or the air-BCB interfaces and coupled back to the LR-SPP guided mode via the periodic structure (Figure 5.25). One of the indications supporting this hypothesis is that the effect gets stronger towards longer wavelength, when the possibility of the coherent scattering out of the plane increases.

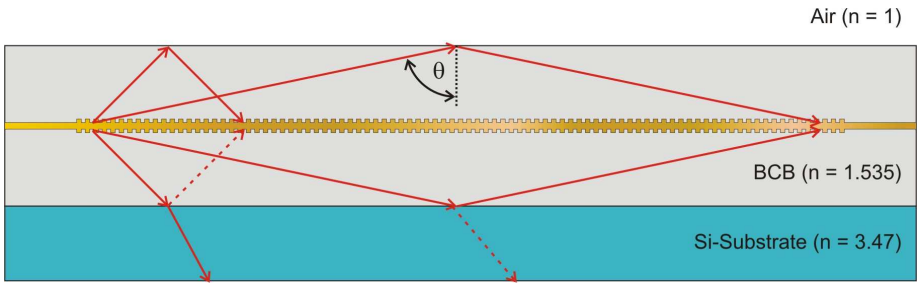

Figure 5.25 Schematic of the possible influence of the reflection from the silicon-polymer and the air-polymer interfaces on the transmission measurements.

The total internal reflection from the air-BCB interface occurs when the incident angle θ is more than 45° ($sin\theta = n_{air}/n_{BCB}$), while for the silicon-BCB interface a strong reflection is expected close to grazing incidence (angle θ more than 85°). Having BCB layers of around 15 μm thickness above and below the waveguide plane, one could expect the sublinear dependence of transmission through structures due to the reflection from the top layer for the structure lengths more than 30 μm, which corresponds very well with the results for the transmission through PC blocks. For longer structures (more than 300 μm long corresponding to the investigated channels) one should expect contributions due to back-reflection from both top and bottom interfaces.

One way to check the hypothesis is to apply a layer of index matching gel on top of the sample in order to increase the top cladding thickness and thus increase the structure length not influenced by the top reflection. To conclude on this, the transmission through PC blocks of different lengths with gel on top of the sample (refractive index 1.535 - the same as for the BCB) was measured and compared with the transmission spectra without gel. As for the general behavior, the index-matching gel on top of the sample improved the situation – the transmission peaks looked more pronounced and the transmission through the longest structures decreased (Figure 5.26).

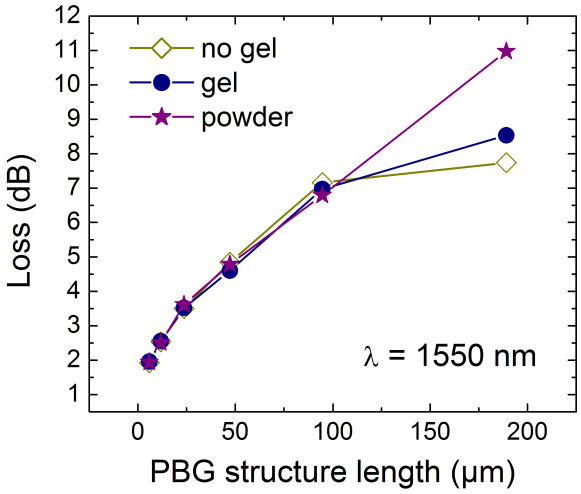

Figure 5.26 The influence of the index matching gel and scattering powder on top of the sample on the transmission loss (570-nm-period triangular lattice, ΓK orientation). Total bump height is 300 nm.

To study the influence of the BCB-Air interface further, a scattering medium (fine polishing powder) was applied on top of the sample to eliminate the influence of the top reflection completely. These measurements showed that the earlier observed sublinear dependence was now much closer to linear (Figure 5.26). However, having a scattering medium on top of the sample made the usual fiber alignments quite difficult.

In order to affect the influence from the silicon-BCB interface, the idea was to make a bottom cladding thicker than 15 μm. However, such samples were difficult to fabricate due to stress in the polymer.

In order to conclude on the influence of the structure borders on the transmission through a PC structure, samples with different widths of periodic areas were fabricated and characterized. Previously the width of the PC area was about 50 μm (depending on the lattice period). The new design contained PC areas of double width and different configurations – with or without metal in the stripe plane (Figure 5.27).

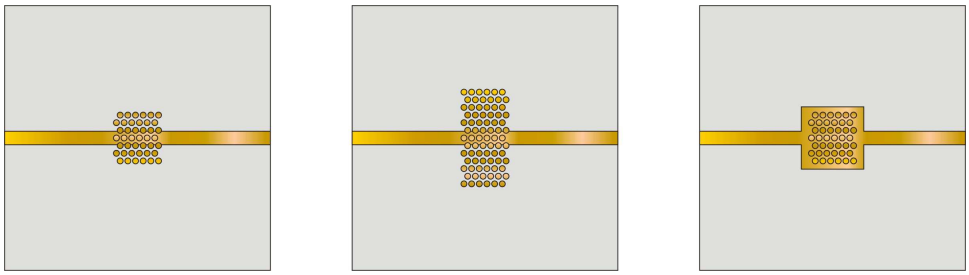

Figure 5.27 Schematic of a PC block of **(left)** normal width, **(center)** double width and **(right)** a block on a metal pad (not to scale).

The analysis of the transmission spectra through PC blocks (for both orientations) for normal width, double width and metal pad in the stripe waveguide plane showed no influence of the structure width or presence/absence of the metal pad on the transmission measurements, indicating that the LR-SPP propagating mode was not affected by the borders of the structure.

5.5 Propagation along channels in photonic crystals

5.5.1 Light confinement to the channel

In order to characterize propagation along channels, LR-SPP stripe waveguides were aligned with line defects in the PC structure and LR-SPPs were coupled directly from a stripe waveguide to the channel. An optical microscope picture of a 240-µm-long and 4.5-µm-wide channel along with an image taken with the camera positioned over the top of the sample, for the light scattered out of the plane while propagating through the channel is shown in Figure 5.28.

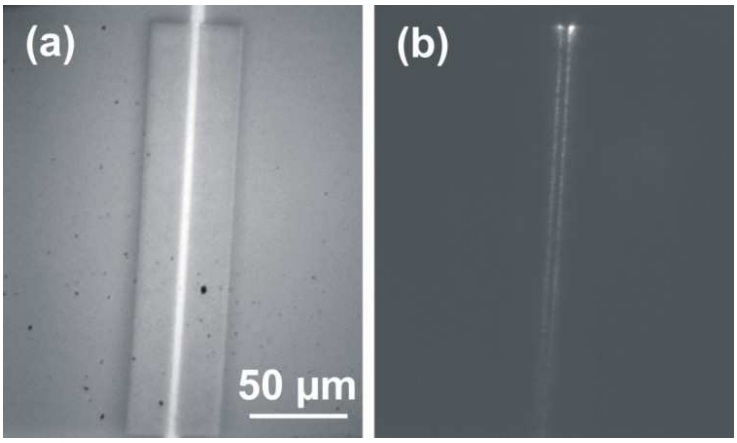

Figure 5.28 Optical microscope images showing top view of a 240-µm-long and 4.5-µm-wide (15 rows of bumps missing) line defect in a 50-µm-wide periodic structure (triangular lattice, period 570 nm, ΓK orientation) together with the 8-µm-wide stripe waveguide **(a)** without and **(b)** with the LR-SPP excitation. Total bump height is 300 nm.

Light scattering observed only at the edges of the waveguide indicates that the mode propagating along the line defect is well confined to the channel and does not penetrate into the PC structure and that it does propagate over the whole channel length.

To quantify the LR-SPP field confinement within the channel, mode profile measurements on truncated waveguides were performed as part of the optical characterization of the PC structures. The output of the truncated channel was imaged on the CCD camera and calibrated using a standard single mode fiber output with a known mode size (~ 10 μm). The output intensity distributions for the channels of different widths are presented in Figure 5.29. It is seen from the output modes of the 8-μm-wide straight LR-SPP stripe waveguide and the channel of the same width (ΓM orientation, 15 rows of bumps removed) that the mode propagating in the 8-μm-wide channel in the PC structure had a smaller size than the mode supported by the 8-μm-wide stripe waveguide indicating stronger light confinement inside the channels. The output intensity distributions for the channels with the widths of 6 μm and 4 μm showed further gradual decrease of the mode size accompanied with the increasing level of the scattered light above and below the structure demonstrating the increasing role of the out-of-plane scattering for narrow channels.

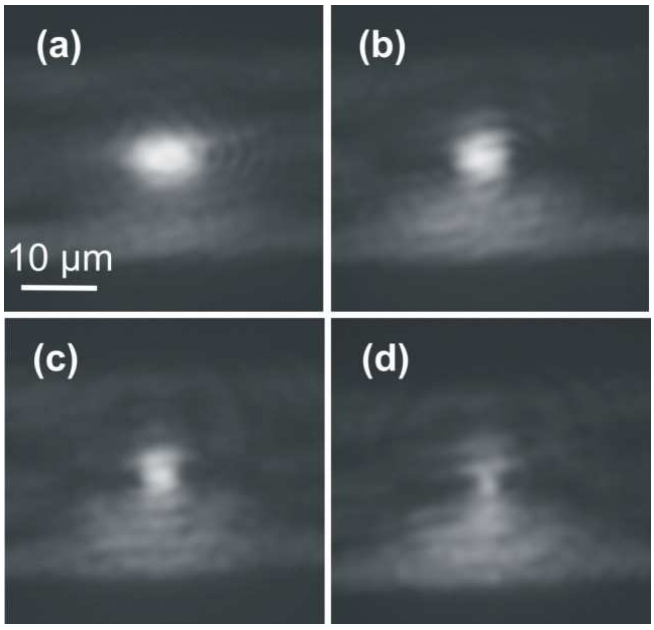

Figure 5.29 Waveguide modes at the output of the **(a)** straight stripe waveguide (8-μm-wide) and channel waveguides (ΓM-oriented structure): **(b)** 8-μm-wide, 15 rows of bumps missing, **(c)** 6-μm-wide, 11 rows of bumps missing, and **(d)** 4-μm-wide, 7 rows of bumps missing. Total bump height is 360 nm.

5.5.2 Transmission and reflection spectra

Line defects with different lengths and channel widths for both ΓK and ΓM orientations were characterized by measuring the transmission and reflection spectra that showed features similar to those described for the blocks. Typical transmission spectra for the channels of different lengths are presented in Figure 5.30 (left graphs).

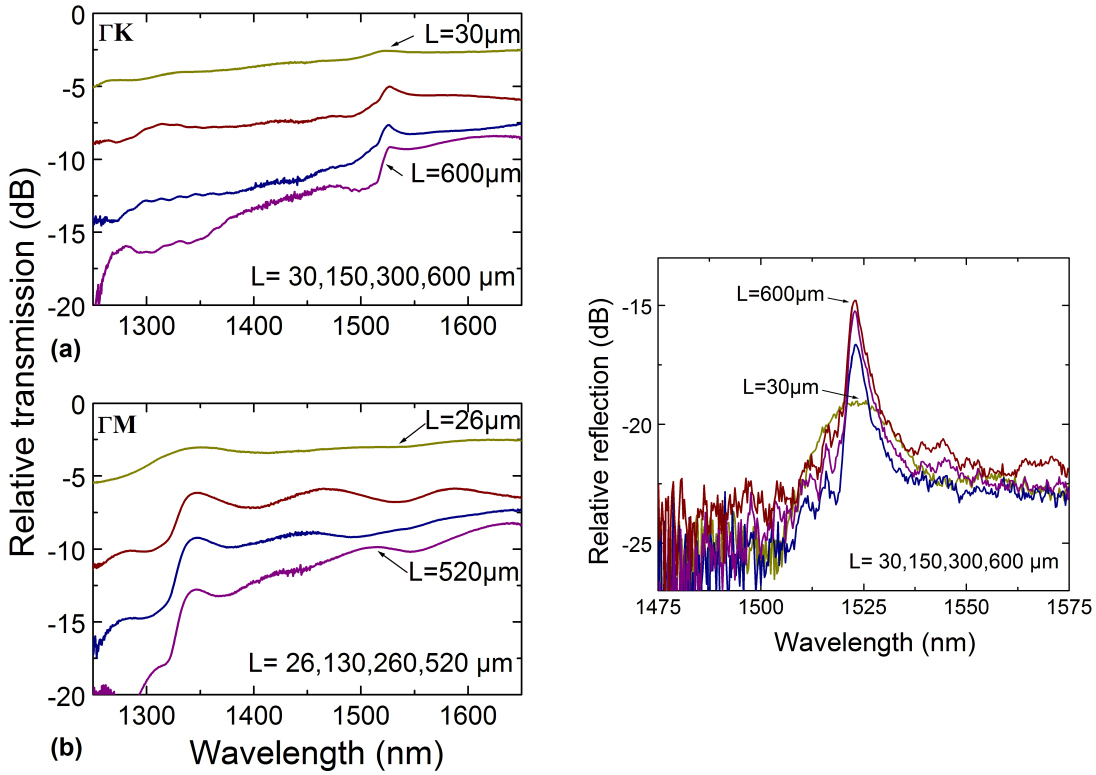

Figure 5.30 Typical **(left)** transmission spectra for channels of different lengths – **(a)** for the ΓK orientation (width approximately 4.5 μm) and **(b)** for the ΓM orientation (width approximately 4 μm) and **(right)** reflection spectra from 3.4-μm-wide channels of the same lengths (ΓK orientation) (triangular lattice, period 570 nm). Total bump height is 300 nm.

The reflection spectra for the ΓK direction (right graphs in Figure 5.30) were consistent with the experimental data for the PC blocks and indicated a large penetration depth of the LR-SPPs into the PC structure (on the order of 100 μm) at the resonance wavelength. As for the blocks, all reproducible features in the measured transmission and reflection spectra for the channels were found to scale in accordance with the lattice constant (Figure 5.31) and experimental peak positions for different lattice periods matched qualitatively with simple Bragg grating estimations (Eq. [4.1]). For the same parameters of the structure, a peak in both the transmission and reflection spectra occurred at approximately the same wavelength as it was observed in case of the blocks. The transmission/reflection peak positions for different samples are summarized in the next section.

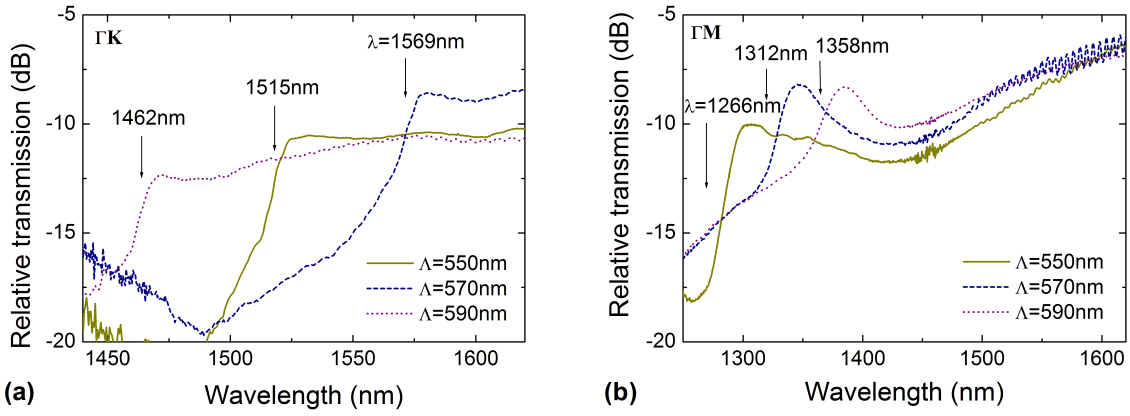

Figure 5.31 Transmission spectra through a channel made in triangular-lattice-structures of different periods (550 nm, 570 nm, 590 nm) and orientations: **(a)** ΓK orientation, length 300 μm, width 4.5 μm, **(b)** ΓM orientation, length 150 μm, width 2 μm. The positions of the transmission peaks are estimated from the Bragg grating arguments. Total bump height is 175 nm.

5.5.3 Propagation and coupling loss

In order to estimate propagation and coupling losses for channels of different widths, the length dependence of the loss for channels of different widths, lattice periods and orientations was analyzed. The "rolling off" tendency mentioned above for the PC block structures was observed primarily for the longest (600-μm-long) of the narrow channels (less than 6-μm-wide) while for wider waveguides the length dependence of the loss was linear, which allow for estimation of the propagation and coupling losses (Figure 5.32).

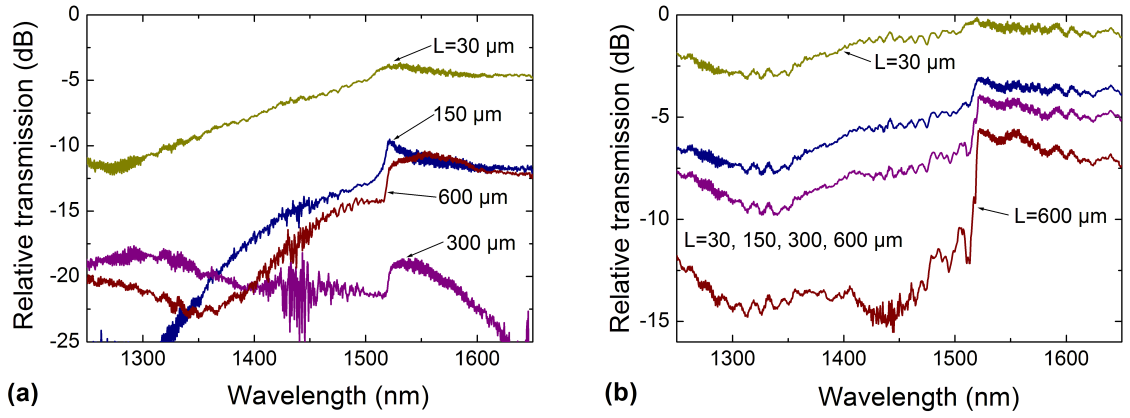

Figure 5.32 Transmission spectra for **(a)** 1- and **(b)** 8-μm-wide channels of different lengths for ΓK orientation of 570-nm-period triangular lattice. Total bump height is 175 nm.

At a given wavelength, the propagation loss was found as the slope of the linear fit to the experimental values of loss obtained for different lengths of the channel. The coupling loss was

also estimated from the cut-back method. For narrow channel widths, only shorter guides were used for the propagation loss estimations, as the loss for the longest waveguides (ca. 600 µm) were too low compared to shorter channels to be used for the cut-back method (Figure 5.32).

The dependencies of the propagation and coupling loss on the channel width for different lattice periods are presented Figure 5.33 for waveguides with ΓM orientation. The lowest propagation loss was observed for the widest channel, i.e. the waveguide formed by the 8-µm-wide line defect. The propagation loss decreased gradually with increasing width of the channel from approximately 50 dB/mm for the 1-µm-wide waveguide to approximately 7 dB/mm for the widest (8 µm) (Figure 5.33 (a)). The coupling between the channel and the 8-µm-wide stripe waveguide was studied for different channel widths and the coupling loss was found to decrease from about 3 dB for the narrowest channel to about 0.3 dB for the widest (Figure 5.33 (b)).

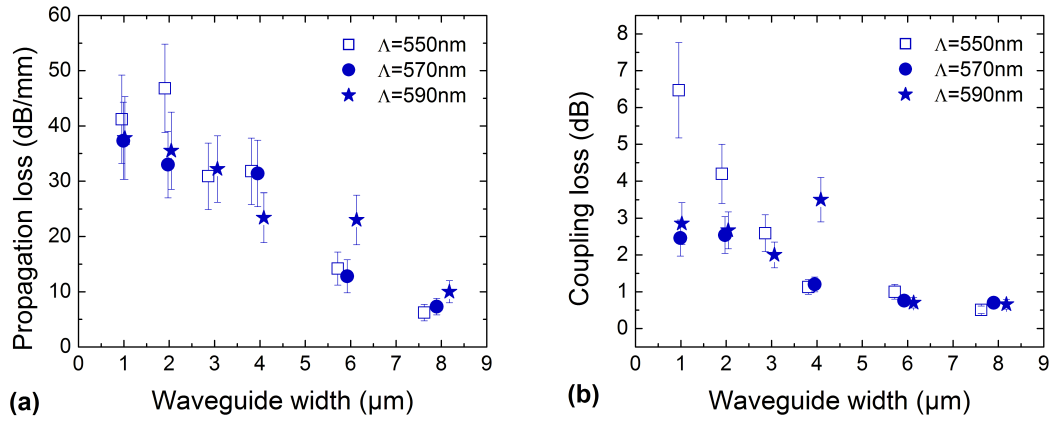

Figure 5.33 Dependence of the **(a)** propagation and **(b)** coupling loss on the waveguide width for different lattice periods for the channel in the ΓM direction. Total bump height is 360 nm. The wavelength is 1550 nm.

The estimated values for the propagation and coupling loss were found to be in the same range for all studied lattice periods and for both ΓK and ΓM orientations of the PC structures. Note that the images of the channel output (Figure 5.29) indicates that for the optimum mode match the line defect should be wider than the stripe waveguide.

5.6 Dependence of the performance on the structure parameters

As it was described in the previous sections, for all investigated periodic structures, the transmission and reflection spectra had a characteristic reproducible peak at the resonance wavelength that was found to scale in accordance with the *lattice constant* (Appendix E). The results show quite good correspondence with the Bragg estimations, taking into account that the real behavior of the system is far more complicated than the simple Bragg reflection. In reality, the

peak position depends on the height of the bumps since increasing the height of the bumps gives higher effective refractive index (Figure 5.34). Moreover, the samples had different quality in terms of bump shape, symmetry and uniformity, resulting in different performance. The exact value for the transmission/reflection peak position can be obtained from the model developed by T. Søndergaard, which was found to match the experimental position well (within the resolution used in calculations) [104].

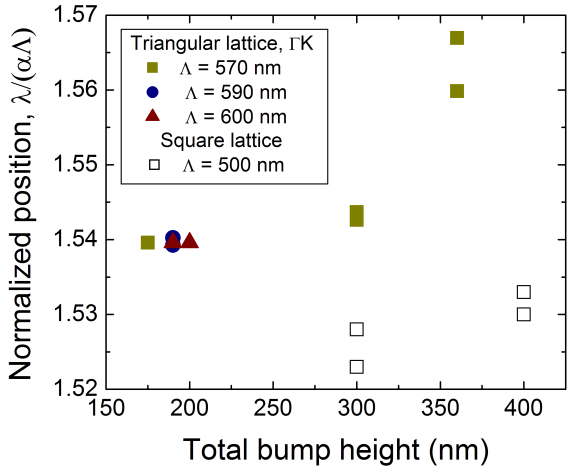

Figure 5.34 Dependence of the normalized peak position, $\lambda/(\alpha\Lambda)$, on the total bump height for a triangular lattice ΓK orientation ($\alpha = \sqrt{3}$) and square lattice ($\alpha = 2$).

The same behavior was found for three different *fill factors* (from 0.15 to 0.25). Therefore, the investigations were focused on structures with 0.2 fill factor.

The overall behavior of the samples containing PC structures with different bump *heights* (from approximately 80 nm to 200 nm on each side of the waveguide plane) was similar. The performance of the structure was more dependent on the *symmetry* than on the actual height of the bumps. Even though higher bumps were expected to increase the efficiency of the in-plane scattering and hence the coherent-scattering effect, they also induced more out-of-plane scattering than lower bumps.

As the symmetry of the system is very important for the LR-SPP propagation, the investigations were focused on symmetrical bumps (bottom height / top height ratio was equal to 1 within 10%). In general, by analyzing all fabricated samples, it was found that the symmetry of the system influenced the performance a lot (Figure 5.35). For the structures composed of symmetrical bumps all features like transmission or reflection peaks were quite clear and reproducible. For the asymmetrical bumps, period dependent features differed from structure to structure and all dependences (for example the dependence of the propagation loss on the channel width) were anomalous. This can be explained by the increasing role of the out-of-plane scattering for asymmetric bumps smearing the effects of the coherent in-plane scattering. The effect of the

asymmetry of the bumps was found to increase with the height of the bumps – slightly asymmetric structures with total bump height of approximately 200 nm behaved almost as symmetrical ones, while the difference between symmetrical and asymmetrical structures with a total bump height of 400 nm was quite noticeable. This is due to the increased scattering into asymmetric (high-loss) SPP modes and the out-of-plane scattering.

The comparison between reflection from the PC structures composed of symmetrical and asymmetrical bumps showed that in the asymmetric case the reflection peaks were much broader than in the symmetric case (Figure 5.35 (b)). This could be related to stronger scattering out of the surface plane for the asymmetrical structure leading to shorter interaction length.

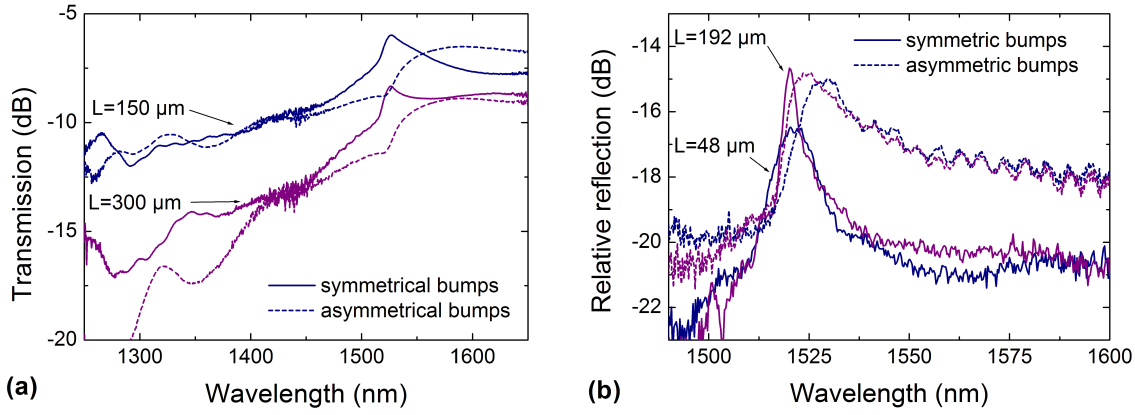

Figure 5.35 (a) Transmission through 3.5-µm-wide channels and **(b)** reflection from PC blocks for symmetrical (height up = height down = 150 nm) and asymmetrical bumps (height up = 185 nm, height down = 215 nm) (570-nm-period triangular lattice, ΓK orientation).

Another factor that could influence the properties of the investigated PC structures is the shape of the bumps, which was slightly conical (probably due to a lower sticking probability at bump edges during the metal deposition process). The influence of this shaping has not been investigated.

5.7 Splitting and bending of the light

As a natural continuation of the studies of the PC structures, PC-based Y-splitters and bent waveguides were fabricated and optically characterized. Different configurations in terms of orientation, channel width and structure length were studied, and an excessively high insertion loss for the PC bends and Y-splitters was observed (so that it was not possible to measure the level of the loss accurately). Different behavior was found for different orientations of the incoming channel demonstrating better light splitting and lower level of the out-of-plane scattering for the ΓM orientation of the channel (Figure 5.36 (a), (b)). As an example, a 20-µm-long PC-based Y-

splitter with 60° splitting angle exhibited an insertion loss of more than 10 dB even for the preferable orientation (Figure 5.36).

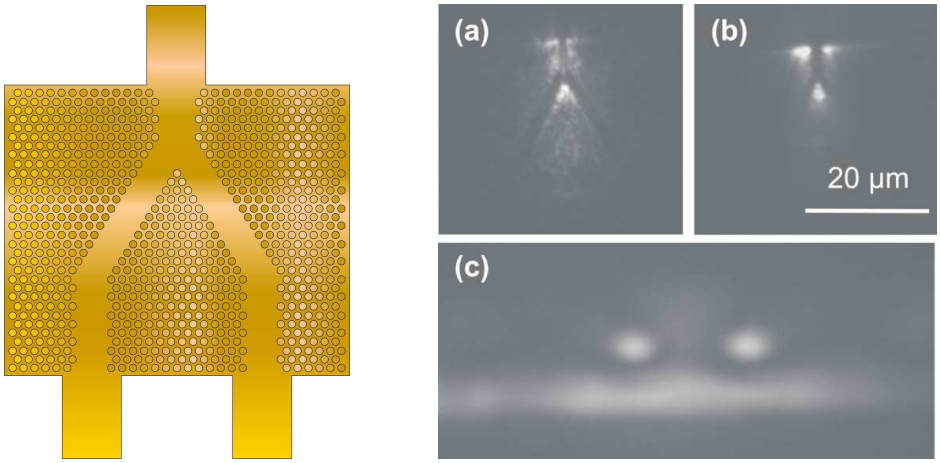

Figure 5.36 (Left) Mask design of a PC Y-splitter together with **(right)** microscope images of the fabricated Y-splitters with 20-µm arm separation when the LR-SPP stripe mode at 1550 nm is excited at its input: top view for the **(a)** ΓM and **(b)** ΓK orientations and **(c)** the output for the ΓM orientation.

For short samples, it was possible to observe the two output modes of the 20-µm-long PC-based Y-splitter (meaning that it did split the light). However, far-field images displayed strong out-of-plane scattering especially at the branching point. For longer structures (longer than 20 µm) no output modes were observed. This means that no efficient bending or splitting of the light was observed for the investigated PC structures.

5.8 Discussion and conclusions

Just because something doesn't do what
you planned it to do doesn't mean it's useless.
Thomas A. Edison

The expectation from the experimental investigation of PC structures in the LR-SPP-supporting configuration was to find a strong band gap for LR-SPPs propagating in structures obtained by symmetric arrays of scatterers placed on both sides of the stripe-waveguide plane. In the second step the hope was to manipulate the LR-SPP propagation including bending and splitting of the light.

For this purpose, full optical characterization of the LR-SPP guiding along straight channels formed by removing several rows of bumps (from 1 to 27 rows missing depending on the PC structure orientation) in the triangular lattice with periods from 550 nm to 600 nm was performed.

Even though microscope images demonstrated good light confinement inside the channel, these investigations also revealed presence of strong *out-of-plane scattering* for the LR-SPP propagation through the PC structures.

Transmission and reflection spectra for PC structures with and without linear defects were studied in a wide wavelengths range from 1250 nm to 1650 nm. From the transmission spectra for different lengths of the channels, the propagation loss was found to decrease gradually when increasing the channel width: from ~ 50 dB/mm for 1-μm-wide channels to ~ 6 dB/mm for 8-μm-wide channels. The coupling loss between a channel and a stripe waveguide was estimated to be 3 dB for 1-μm-wide channels, decreasing to approximately 0.3 dB for 8-μm-wide channels.

The investigations of the PC structures (in particular, the reflection spectra for the PC blocks and waveguides) indicated that the structures exhibited a *large LR-SPP penetration depth* (~ 100 μm) into the PC structures. However, typical features expected for the well pronounced (strong) PBG effect, e.g., a fairly large decrease in the transmission through the PC blocks within a certain wavelength interval, were not found in the transmission spectra. These observations imply that the coherent multiple LR-SPP scattering, though occurring in the investigated PC structures, is rather *weak*, so that the photonic band gap might be expected only for some particular propagation directions (e.g., ΓK) providing only poor field confinement. This conclusion is also consistent with the observed increase in the propagation loss with decrease in the channel width (Figure 5.33).

Preliminary results of the investigations of bends and splitters in the PC structures also showed that the PC waveguides bent or split at relatively large angles (30°/60°) exhibit excessively high insertion loss. On the other hand, a 20-μm-long PC-based Y-splitter with 60° splitting angle did divide the incident LR-SPP mode between two output channels with the output stripe waveguide modes being clearly observed.

5.8.1 Enhancement of the coherent-scattering effect

Since one of the main attractions of the PC structures (in the integrated-optics context) is a possibility of low-loss guiding around sharp corners, one should think of potential enhancement of the coherent (multiple) scattering of LR-SPPs. For all investigated structures, the effect of coherent scattering is present (Bragg-like phenomena observed in reflection and transmission) but too weak to provide an efficient in-plane field confinement. Here it is relevant to mention that a very strong PBG effect is predicted for two-dimensional periodic structures of metal rods [40], corresponding to the limit of infinitely high bumps. Therefore, by optimizing parameters of the PC structures such as bump height, bump shape and size it might be possible to enhance the coherent-scattering effect for LR-SPPs.

Another possibility is to try to squeeze the mode in the vertical direction, say, by using a thicker metal film. This will decrease the vertical mode size making the LR-SPP more sensitive to the lower perturbations. This will of course lead to an increase in the propagation loss, which has to be taken into account.

Alternative designs that combine the intrinsic vertical confinement of the LR-SPP with the possibility of the efficient in-plane confinement by other means, than making periodic arrays of metal bumps, are also possible.

In summary, LR-SPPs were found to behave quite differently from conventional SPPs while propagating in 2D periodic structures. For the LR-SPP, the weak confinement to the metal film, so beneficial for a stripe waveguide giving rise to low propagation and coupling losses, becomes a problem in relation to the in-plane LR-SPP manipulation. It was found that LR-SPPs, being weakly bound to the metal film, are easier scattered out of the surface plane than normal SPPs. It turned out to be problematic to utilize the PBG concept for LR-SPPs using the same approach as for the realization of SPPBG structures. Since LR-SPPs seem to be quite promising for photonic applications, the issue of efficient control of the LR-SPP propagation in the surface plane is still to be studied.

5.8.2 Usage of weak coherent-scattering effect

The advantage of using the PC structures does not include only miniaturization possibilities. Even though in the 2D case there is a threshold for the full PBG, which seems to be quite difficult to achieve, *weak coherent-scattering effect* does not mean one can't use it. For example, Bragg gratings are normally based on a weak 1D modulation of the refractive index.

Investigations of the PC structures with low bumps (50 nm on each side of the waveguide plane) indicated feasibility of applying a 1D-PC approach for LR-SPPs. The results for the transmission and reflection spectra for structure with low bumps showed a resemblance to the usual Bragg-grating behavior (discussed in the next chapter) with a dip in the transmission and a broad reflection peak including the side lobes (Figure 5.37). The side lobes, which are the characteristic feature for weak gratings, have not been observed before since for all investigated structures, the reflection was considerably stronger resulting in all side lobes being smeared out.

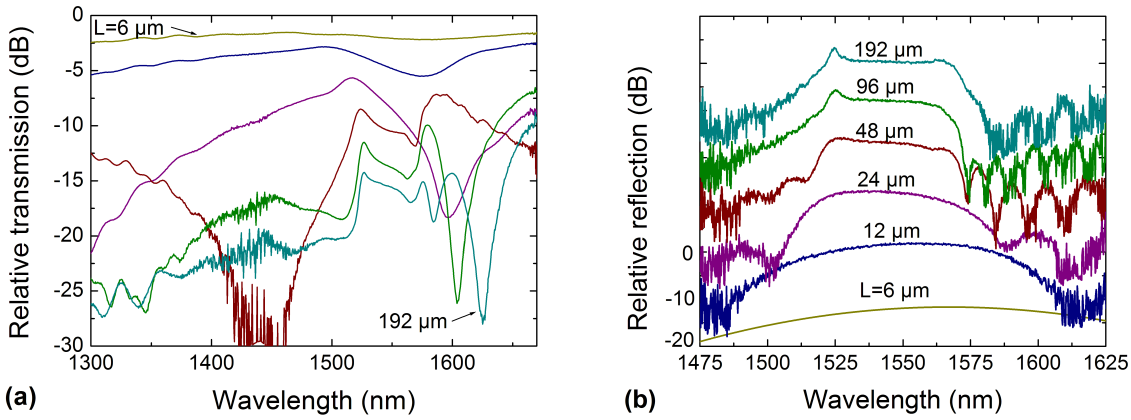

Figure 5.37 (a) Transmission through and **(b)** reflection from PC blocks of different lengths (from 6 µm to 192 µm) for a total bump height of 100 nm. 570-nm-period triangular lattice, ΓK orientation. Reflection spectra are shifted 10 dB upwards with respect to each other (starting from 12-µm-long structure) for clarity.

Even for low bumps the influence of the out-of-plane scattering is quite strong, making experimental transmission data hard to interpret. If one wants to proceed with the 1D PC structures for the LR-SPPs the amount of out-of-plane scattering and other losses (like loss in metal) should be reduced. This can be achieved by decreasing the height of the bumps (or ridges in the 1D case) further. This idea turned out to be very promising, and the analysis of the ridge gratings for LR-SPPs is presented in the next chapter.

6 Ridge Gratings for Long-Range Surface Plasmon Polaritons

The most important thing in science is not so much to obtain
new facts as to discover new ways of thinking about them.
Sir William Bragg

This chapter provides the basic Bragg grating theory and a summary of experimental results obtained for Bragg gratings for long-range surface plasmon polaritons. The chapter begins by an introduction to Bragg gratings describing the basic equations. In section 6.2, the experimental findings for LR-SPP ridge Bragg gratings are reported, including transmission and reflection spectra. Thereafter, the lossless Bragg grating model is applied to the investigated LR-SPP gratings, providing estimates for the effective refractive index modulation. The Bragg grating filter bandwidth is also estimated and compared to the experimental results. The data analysis is continued by the estimation of the grating strength for the different heights of the ridges. The chapter finishes with the conclusion section where realization of a compact wavelength add-drop filter is reported.

6.1 Introduction to Bragg gratings

The Bragg grating is analogous to the dielectric stack mirror depicted in Figure 5.1. The grating reflects light in a specific spectral range, centered at the Bragg wavelength. For one-dimensional periodic structures, the reflectivity can approach 100% even for a small refractive index modulation ($\Delta n \ll 1$), i.e., for weak gratings. The strength of the reflection increases with the number of periods (length of the grating) and is strongest for normal incidence.

Bragg gratings in integrated optical circuits consist of a periodic modulation in the refractive index of an optical waveguide. There are many ways to induce a periodic modulation into a waveguiding layer. The refractive index of the waveguide core can be modulated directly by illuminating the waveguide with UV light [116], or by means of acousto-optical or electro-optical effects [117]. A more flexible way of introducing a periodic modulation is to corrugate the

waveguide structure using lithography and pattern-transfer techniques. In this work, electron-beam lithography was utilized.

6.1.1 The Bragg condition

By introducing a periodic modulation in the waveguide, it is possible to create an interaction between the otherwise decoupled forward-traveling and backward-traveling modes of the waveguide. In other words, the Bragg grating works as a diffraction grating, which diffracts light from the forward-traveling mode into the backward-traveling mode. The requirement for efficient diffraction in the opposite direction is that the reflections from the subsequent grating planes must interfere constructively. This condition for a strong reflection from the grating is called the *Bragg condition*. This occurs when half the wavelength of the incident light equals the optical distance between the grating planes [118]:

$$\lambda_B = 2n_{eff}\Lambda \qquad [6.1]$$

where λ_B is the *Bragg wavelength* (free-space wavelength satisfying the Bragg condition), n_{eff} is the effective refractive index of the propagating mode, and Λ is the grating period.

The above expression is called the *first order* Bragg condition since the phase accumulation between reflections from adjacent grating lines is precisely one wavelength. The more general condition for constructive interference is that the phase accumulation between subsequent reflections is an integral number of wavelengths. This gives the Bragg condition for an *N*-order grating:

$$\lambda_B = 2n_{eff}\Lambda/N \qquad [6.2]$$

Typically, only first-order Bragg gratings are considered since the diffraction efficiency is generally stronger for the first diffracted order.

6.1.2 Spectral response

The most common way of analyzing Bragg gratings is to use the *coupled mode theory* [67,118-120]. In this approach, the grating is considered as a small perturbation of the optical waveguide. This perturbation produces a coupling between the forward and backward modes of an unperturbed waveguide, and the electromagnetic fields of such structure can then be expressed as a superposition of the fields of the unperturbed waveguide.

From the coupled mode theory, for a lossless uniform grating with the length *L*, the spectral dependence of the reflection can be expressed as [120]:

$$r(\delta) = \frac{\frac{\kappa^*}{\gamma}\tanh(\gamma L)}{1 + i\frac{\delta}{\gamma}\tanh(\gamma L)}, \gamma \equiv \sqrt{|\kappa|^2 - \delta^2} \quad [6.3]$$

$$\delta \equiv \beta - \frac{\pi}{\Lambda} = \frac{2\pi n_{eff}}{\lambda} - \frac{2\pi n_{eff}}{\lambda_B} \quad [6.4]$$

where δ is the deviation from the Bragg condition, λ is the wavelength, and κ is the coupling constant. The magnitude of κ describes the rate at which power transfers between the forward and backward modes. It is often represented as the *reflectivity per unit length* of the grating or the *grating strength*.

The peak reflectivity that defines the maximum reflectivity at the Bragg wavelength ($\delta = 0$) is given by:

$$R_{\max} = |r(\delta = 0)|^2 = \tanh^2(\kappa L) \quad [6.5]$$

From Eq. [6.3] zero-points in the reflection spectra can be found from the condition $r(\delta) = 0$:

$$\tanh(\gamma L) = 0 \quad [6.6]$$

$$L^2 \cdot \left(\delta^2 - |\kappa|^2\right) = (m\pi)^2, m = \pm 1, 2... \quad [6.7]$$

This gives the zeros at:

$$\delta_m = |\kappa| \cdot \sqrt{1 + \left(\frac{m\pi}{|\kappa| L}\right)^2}, m = \pm 1, 2... \quad [6.8]$$

When the product κL is small compared to 1, the spectral response of the Bragg gratings has a characteristic "sinc" shape with the bandwidth inversely proportional to the grating length. In this limit, the spectral response can be approximated as [120]:

$$r(\delta) = i\frac{\kappa^*}{\delta}\sin(\delta L) \quad [6.9]$$

In this case, the gratings are called *weak gratings* since they reflect only a fraction of the incident light. The overall behavior in this regime is determined only by the grating length, while the peak reflectivity also depends on the reflectivity per unit length, κ. The calculated reflection spectra for weak Bragg gratings (κL from 0.1 to 0.4) are presented in Figure 6.1. In this regime the spectral width (between the first minima) of the central region with the highest reflectivity is given by [6.8] for $\kappa L << 1$:

$$\Delta = 2\delta_1 = \frac{2\pi}{L} \text{ for } m = \pm 1 \quad [6.10]$$

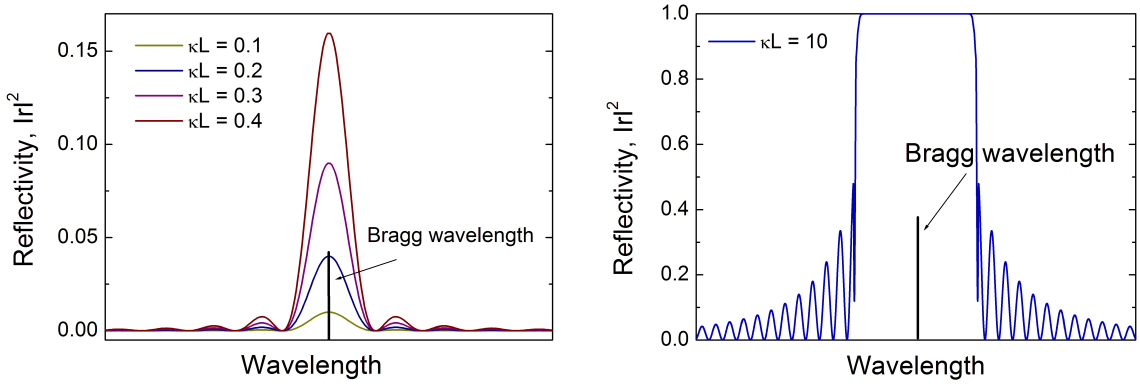

Figure 6.1 (Left) Reflection spectra for weak Bragg gratings (κL changes from 0.1 to 0.4), featuring the "sinc" shape centered around the Bragg wavelength, and **(right)** for a strong grating (κL=10), showing a plateau-like shape of the stopband – the region with very high reflectivity.

For strong gratings ($\kappa L >> 1$) the spectral response has a plateau-like shape where the reflectivity of the grating is very high (Figure 6.1). The width of the region with high reflectivity (*the stopband*) is given by [6.8] for $\kappa L >> 1$:

$$\Delta = 2\delta_1 = 2|\kappa| \quad \text{for } m = \pm 1 \qquad [6.11]$$

From Eq. [6.4], one can express the spectral width of the stopband as:

$$\Delta \approx \frac{4\pi n_{eff}}{\lambda_B^2} \cdot \Delta\lambda \qquad [6.12]$$

$$\left(\frac{2\Delta\lambda}{\lambda_B}\right)_{Bandwidth} = \frac{\kappa\lambda_B}{\pi n_{eff}} \qquad [6.13]$$

where $\Delta\lambda = (\lambda - \lambda_B)$. In this regime, the spectral width of the stopband is proportional to the grating strength. For longer gratings with the same grating strength, the width of the stopband remains the same while the maximum reflectivity increases closer to 1 (100% reflection). At the same time, the spectrum around the Bragg wavelength becomes more square and the distance between the sidelobes gets smaller.

Outside the stopband, the spectral response consists of sidelobes that decay rapidly when moving away from the Bragg condition. In the regime well outside of the stopband, the reflectivity of the grating can again be approximated by Eq. [6.9].

For typical waveguide structures, the grating strength is proportional to the effective refractive index modulation Δn [119,120]: $\kappa \propto \pi\Delta n/\lambda_B$.

6.2 LR-SPP-based Bragg grating filters

6.2.1 Sample description and experimental arrangement

In this work the Bragg gratings for LR-SPPs were investigated. A periodic modulation was created in the LR-SPP stripe waveguide by modulating the thickness of the stripe in a periodic way. The resulting configuration represents a grating of metal ridges protruding symmetrically above and below the metal film embedded in the dielectric (Figure 6.2).

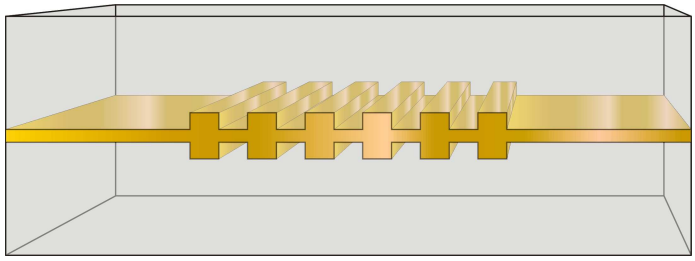

Figure 6.2 Schematic of the type of Bragg grating considered in this work. A grating is formed by corrugating both surfaces of the stripe waveguide.

The fabrication process for the Bragg gratings is similar to the one used for making PC structures for LR-SPPs. Only instead of periodic arrays of bumps, parallel ridges, forming a grating, were patterned using electron-beam lithography.

The gratings were designed to operate at 1550 nm. Gold ridges of width w, varying from 125 nm to 375 nm, were arranged in 500-nm-period (Λ=500 nm) gratings of different lengths (fill factor, w/Λ, ranging from 0.25 to 0.75). The ridges were placed symmetrically above and below the LR-SPP propagation plane creating the variation of the stripe thickness. 15-nm-thick LR-SPP stripe waveguides defined by standard UV lithography were placed in the middle of the gratings (Figure 6.3). Fabricated samples contained gratings of different length (from 20 to 160 μm), fill factors (from 0.25 to 0.75), and height of the ridges. Ridge height was from 5 to 30 nm on each side of the stripe waveguide, corresponding to the total ridge height of 10-60 nm excluding the thickness of the stripe (15 nm).

For optical characterization, spectrally resolved reflection and transmission measurements of the LR-SPP gratings were performed. The experimental setup was similar to the one used for characterization of the PC components. Transmission and reflection spectra were recorded in the wavelength range from 1500 to 1600 nm with a resolution of 0.5 nm and high sensitivity (-80 dBm). Transmission spectra through the grating structures were normalized to the transmission through a straight stripe waveguide that did not contain a grating.

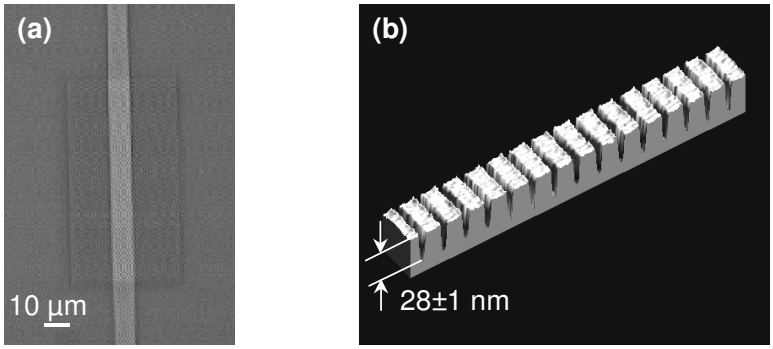

Figure 6.3 **(a)** Optical microscope image showing top view of the 40-µm-wide and 80-µm-long ridge grating placed in the middle of an 8-µm-wide stripe together with **(b)** the profile of the ridges on one side of the waveguide plane obtained using atomic force microscopy. The total height of the ridges is about 56 nm (approximately 28 nm on each side of the waveguide plane).

Reflection spectra from the gratings were normalized to the reflection from a mirror and corrected by approximate values of coupling and propagation loss for the incoming LR-SPP waveguide. The coupling loss was assumed to be ~ 0.5-0.8 per facet (obtained previously for 8-µm-wide stripe waveguides). In order to estimate the propagation loss for a particular sample, reflection from identical gratings was measured for four different distances (2, 4, 6, and 8 mm) from the input plane to the grating (Figure 6.4).

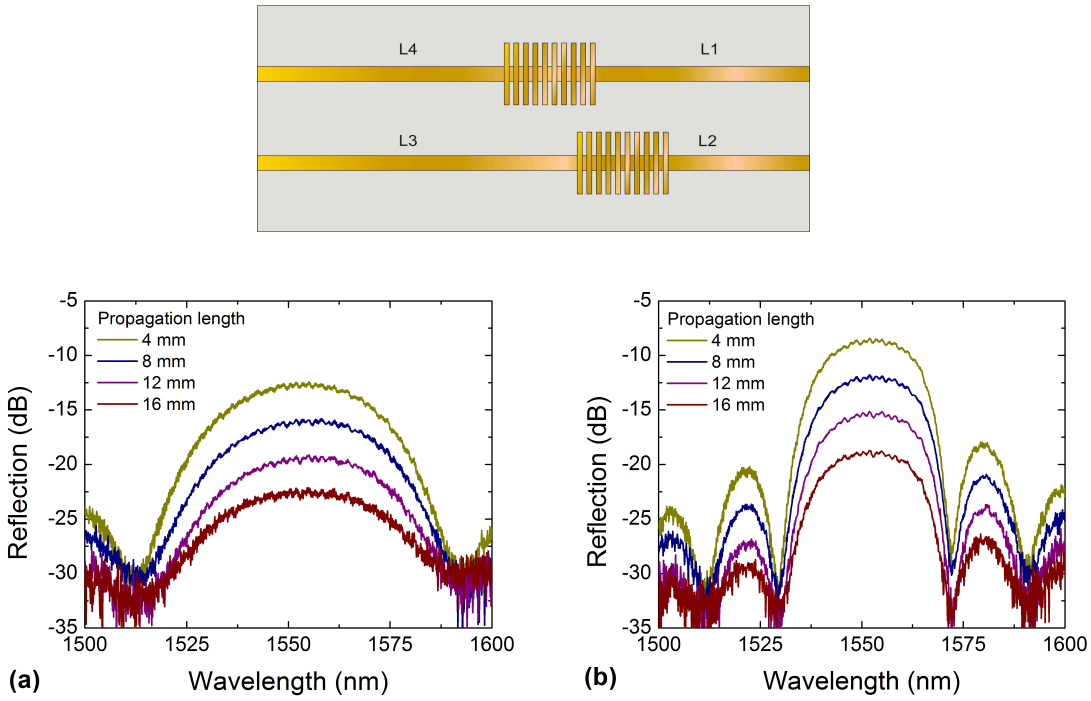

Figure 6.4 **(Top)** Sample configuration where identical gratings are placed at different distances from the input facet and **(bottom)** reflection from **(a)** 20-µm-long and **(b)** 40-µm-long gratings for 4 different distances from the input facet. Grating period 500 nm, fill factor 0. 45, total ridge height 40 nm.

In this way, a propagation loss of ~ 8.5 dB/cm was found using the cut-back method (Figure 6.5). The obtained value of the propagation loss is higher than the one reported for straight LR-SPP waveguides (section 4.2.1). This might be connected to additional fabrication steps involved, namely electron-beam lithography and related processing.

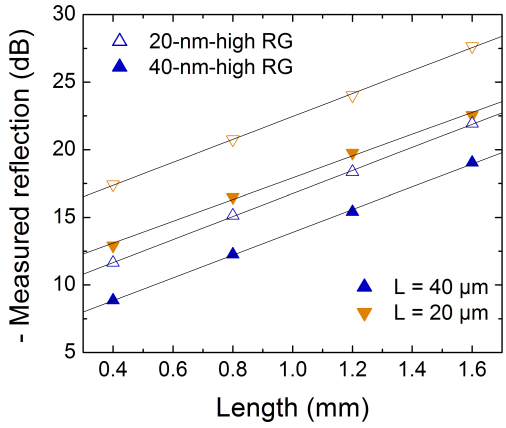

Figure 6.5 Propagation loss estimated from data obtained for different gratings (length 20 and 40 µm, total ridge height is 20 and 40 nm, fill factor is 0.45). The propagation loss for the stripe waveguides was found to be ~ 8.5 dB/cm.

6.2.2 Reflection spectra

Typical reflection from gratings of different lengths is shown in Figure 6.6 for different heights of the ridges. All measured reflection spectra showed pronounced Bragg-grating behavior, when gradual increase in strength and decrease in width of the reflection peak was observed with the increasing length of the grating from 20 to 160 µm. For example, for 500-nm-period gratings (fill factor of 0.45) with a total height of the ridges of 20 nm (approximately 10 nm on each side of the waveguide plane) the maximum reflection was found to increase from ~ 5% for the 20-µm-long grating to approximately 57% for a 160-µm-long grating while the full width at half-maximum (FWHM)[7] bandwidth of the reflection peak decreased from ~ 36 nm to ~ 10 nm, respectively.

As predicted by the theory [120], the side lobes of the spectral dependence of the reflection became narrower and denser with increasing grating length.

With increasing height of the ridges, the gratings became stronger due to the increased effective index modulation. This lead to a broadening of the reflection peak (Figure 6.7) and faster saturation. For example, for the 10-nm-high ridges (total height), a 160-µm-long grating (320 periods) showed ~ 45-50% reflection (still no saturation) while for the 60-nm-high ridges, the reflection saturation occurred around 160 periods (80-µm-long grating).

[7] In practice, the FWHM is used more often than the spectral width between the first minima.

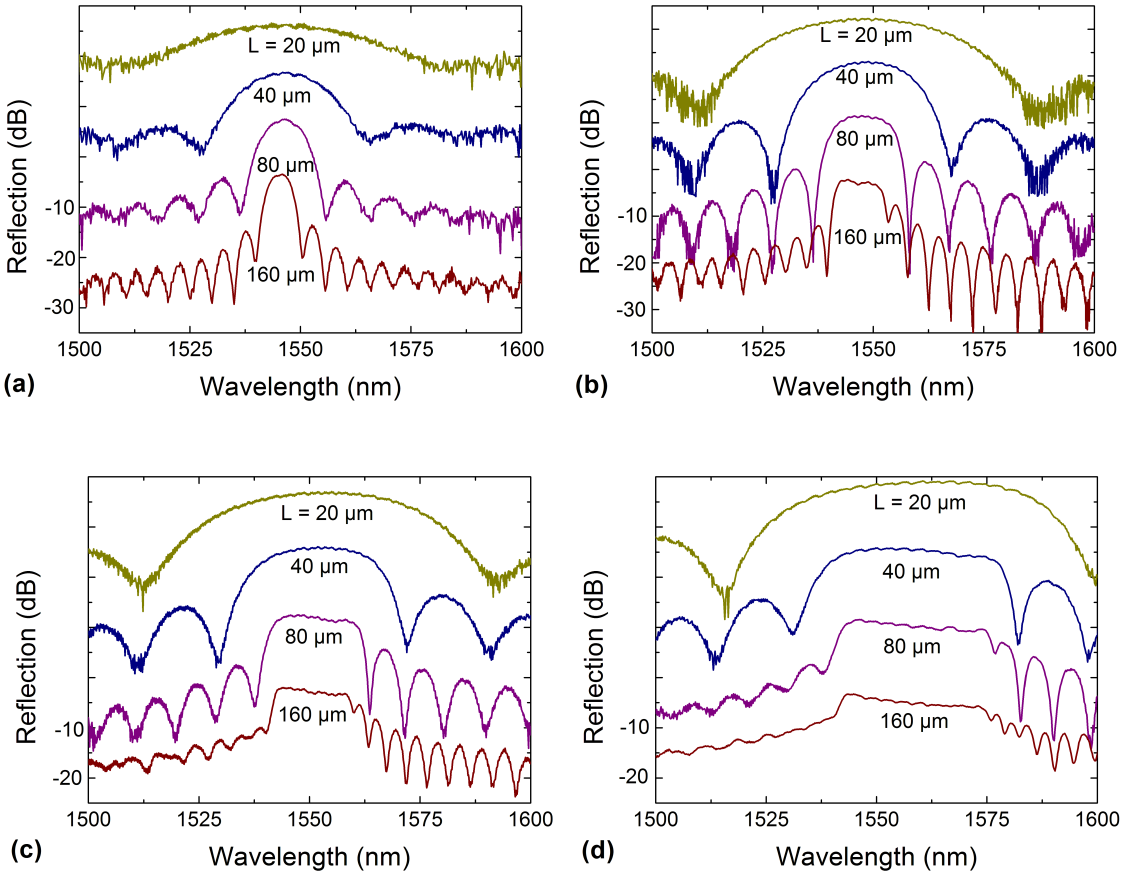

Figure 6.6 Reflection from the gratings of different lengths (20, 40, 80, and 160 µm). For clarity, the spectra are shifted 15 dB upwards with respect to each other (starting from the spectrum for an 80-µm-long grating). The heights of the ridges are ~ **(a)** 5 nm, **(b)** 10 nm, **(c)** 20 nm, and **(d)** 30 nm on each side of the waveguide plane (total ridge height from 10 to 60 nm). Period is 500 nm, fill factor is 0.45.

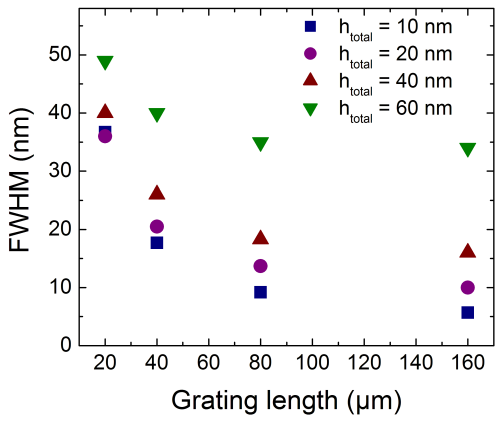

Figure 6.7 Full width at half-maximum bandwidth vs. grating length for different heights of the ridges. Period is 500 nm, fill factor is 0.45.

However, for strong gratings with high ridges (more than 10-nm-high), the maximum reflection did not approach unity even in the saturation region (160-μm-long gratings). Moreover, it was found that with the increasing volume of metal (higher ridges), the maximum reflectivity of saturated reflection decreased (Figure 6.8 (a)). For example, the maximum reflection was found to decrease from ~ 60% for a total height of the ridges of 40 nm to ~ 46% for 60-nm-high ridges (Λ=500 nm, grating length 160 μm, fill factor 0.35). This is due to the increasing loss, which includes out-of-plane scattering and absorption in metal. For high ridges (40-60 nm total height) the reflection spectra resemble those measured for PC structures with a total bump height of 100 nm (Figure 5.37).

The dependence of the maximum reflection on the fill factor is presented in Figure 6.8 (b) showing a slight increase in the reflection with the increasing fill factor.

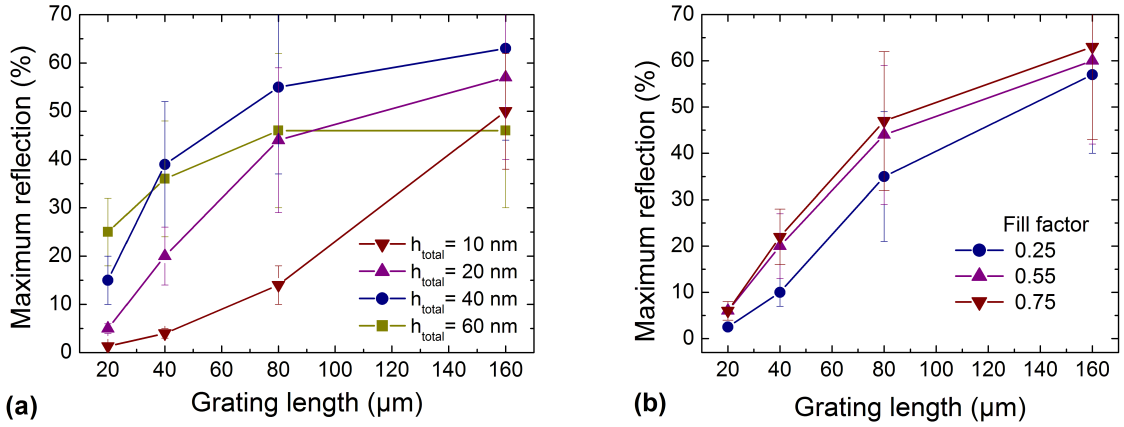

Figure 6.8 Maximum reflectivity vs. grating length **(a)** for different heights of the ridges (fill factor is 0.35) and **(b)** for different fill factors (total height of the ridges is 20 nm). Grating period is 500 nm.

The spectral shape of the reflection is rather asymmetric (Figure 6.6), which is not expected from the simple Bragg theory. The asymmetry can be related to the influence of the LR-SPP absorption in the stripe and by the ridges and, especially, to the effect of the out-of-plane scattering. The directional scattering, i.e., the LR-SPP diffraction in the direction of angle θ determined by the relation: $\lambda \cong n\Lambda(1 + \sin\theta)$, occurs only for the wavelengths above the Bragg wavelength. The out-of-plane scattering of the incident LR-SPP by ridges is also expected to increase (though gradually) towards shorter wavelengths.

Another characteristic feature, observed for strong gratings (ridges higher than 10 nm), was a flat skew top of the reflection-band spectral shape, where the central part of the reflection spectrum approached an inclined straight line with increasing grating length (Figure 6.6). The same behavior of the spectral dependence of the reflection was reported for deeply etched waveguide Bragg gratings [121].

The experimental results were found to be in excellent agreement with the calculated reflection spectra, obtained from a theoretical model developed by T. Søndergaard [105]. The model predicted very well the behavior and the value of the reflection peak as well as the sidelobe positions and asymmetry of the spectrum.

The reflection from the gratings with different periods showed very reproducible shifts in the Bragg wavelength according to the Bragg condition (Figure 6.9). The maximum-reflection level was found to be the same (within 0.5 dB) for 5 different-period-gratings of the same fill factor and length.

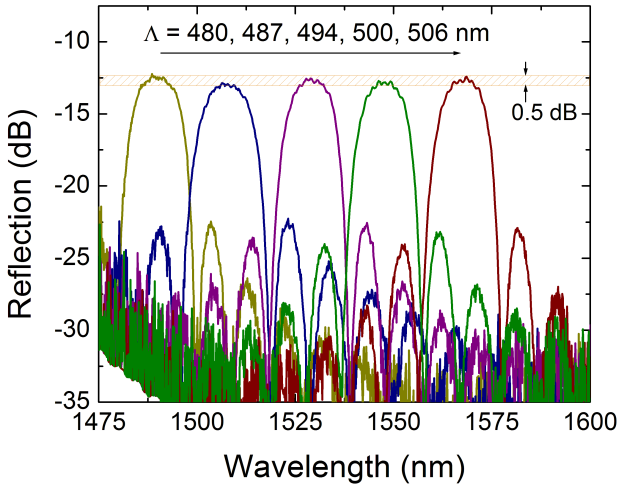

Figure 6.9 Reflection from Bragg gratings of different periods (length is 160 periods, fill factor is 0.35). The total ridge height is 20 nm.

6.2.3 Transmission spectra

Typical transmission through gratings of different lengths for different heights of the ridges is shown in Figure 6.10. For low ridges (total height of 10-20 nm), normal Bragg-grating behavior was observed, with a transmission dip at the Bragg wavelength. For a total ridge height of 10 nm, the dip in transmission was found to increase from ~ 0.3 dB for a 40-μm-long grating to ~ 3 dB for a 160-μm-long grating (Figure 6.10 (a)).

For higher ridges (total height 40-60 nm), more complicated behavior was found, when two dips appeared for long gratings. In this case, the asymmetry of the transmission spectra became more pronounced. Just like for the reflection spectra, in this regime, the behavior of the transmission through the gratings was similar to that observed for PC structures (Figure 5.37).

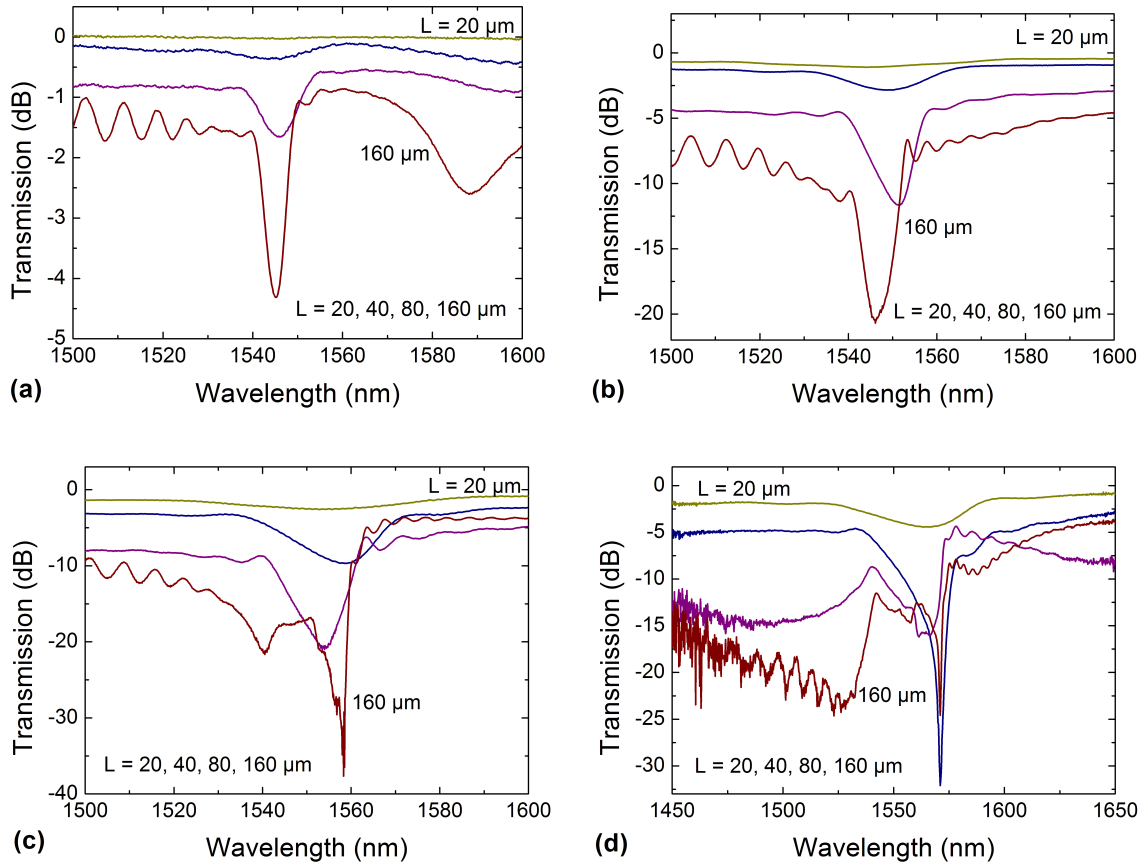

Figure 6.10 Transmission through gratings of different lengths. The heights of the ridges are ~ **(a)** 5 nm, **(b)** 10 nm, **(c)** 20 nm, and **(d)** 30 nm on each side of the waveguide plane (total ridge height from 10 to 60 nm). Period is 500 nm, fill factor is 0.45.

The characteristic features observed from the transmission spectra are asymmetry in the spectra with respect to the Bragg wavelength, the Bragg wavelength shift with the increase in the grating length and different transmission loss levels outside of the resonance. These features are again related to the influence of the LR-SPP absorption in the metal and to the effect of the out-of-plane scattering.

Just like in the case of reflection spectra, excellent correspondence between calculated and experimentally obtained data was demonstrated by using a detailed theoretical model [105]. The model predicted the shape of the spectral dependencies (including two dips in the transmission spectrum, the asymmetrical shape and the oscillations outside the band for long gratings) and provided a value for the transmission dip, which was found to be very close to experimentally obtained value.

Transmission measurements were also performed for gratings placed on a stripe at different angles. Typical dependence of the transmission on the angle between input and output waveguides is presented in Figure 6.11, showing increasing grating efficiency when approaching normal incidence.

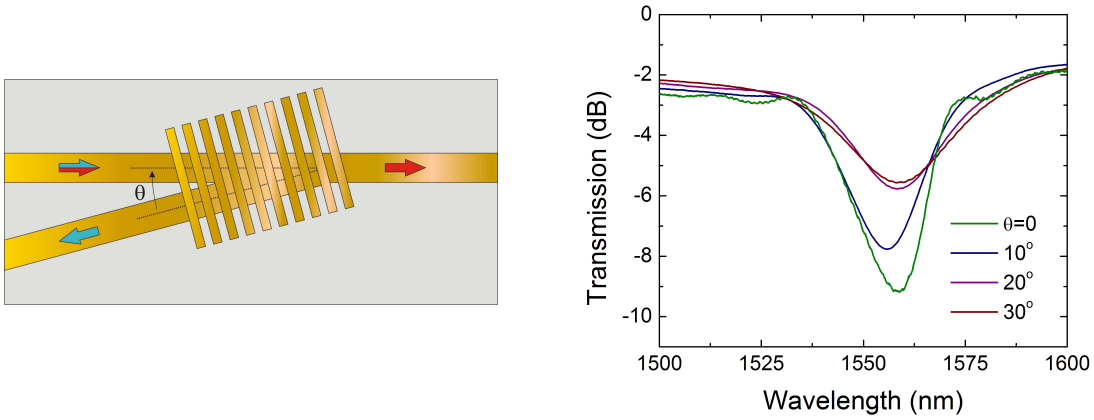

Figure 6.11 (Left) Schematic of an angled grating and **(right)** transmission through an 80-period long grating placed at different angles with respect to the input stripe. Grating period ~ 500 nm, fill factor 0.3, total ridge height is 40 nm.

6.2.4 Loss in LR-SPP gratings

In order to estimate the losses introduced by the gratings in different wavelength ranges, the sums of reflection and transmission spectra are plotted in Figure 6.12 and Figure 6.13. For the 80-µm-long grating (20-nm-high ridges, 500-nm-period, 0.45 fill factor) the in-band loss at the Bragg wavelength was estimated to be on the order of 2-2.5 dB while outside the band the loss was found to increase up to 4.5 and 3 dB in the short- and long-wavelength region, respectively. As in the case of 2D PC structures, such a pronounced decrease in the total loss at the Bragg wavelength is mainly related to the strong LR-SPP-to-LR-SPP scattering and decrease in the out-of-plane scattering at the resonance wavelength. The possible explanation for the decrease in the out-of-plane scattering could be that the standing field pattern, formed at the Bragg wavelength, matches the grating profile so that the total (incident and reflected) field at the ridge edges has its minimum.

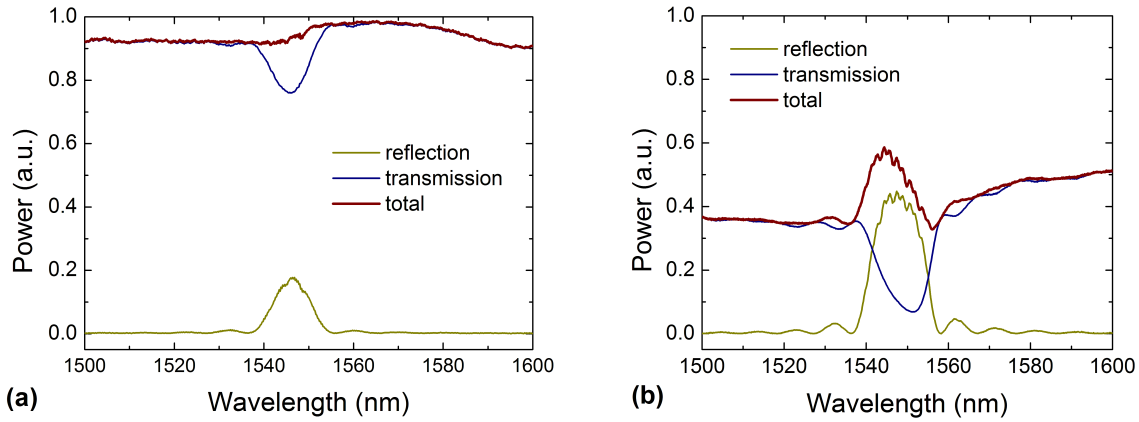

Figure 6.12 Transmission, reflection and total power spectra for 80-µm-long gratings. Heights of the ridges are ~ **(a)** 5 nm and **(b)** 10 nm on each side of the waveguide plane (total ridge height is 10 and 20 nm), period is 500 nm, fill factor is 0.45.

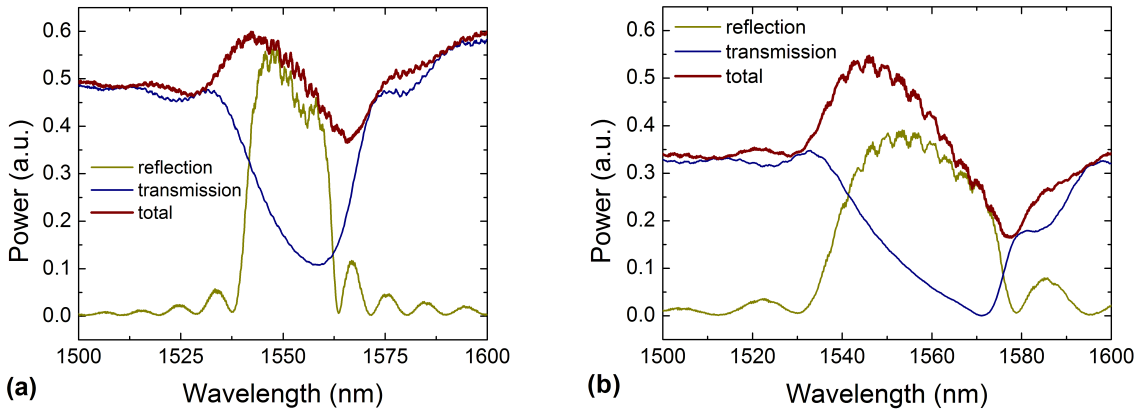

Figure 6.13 Transmission, reflection and total power spectra for 40-µm-long gratings. The heights of the ridges are ~ **(a)** 20 nm and **(b)** 30 nm on each side of the waveguide plane (total ridge height is 40 and 60 nm), period is 500 nm, fill factor is 0.45.

The loss was found to increase with the height of the ridges both at the Bragg wavelength and outside the resonance due to increasing out-of-plane scattering and absorption in metal (Figure 6.14). For example, at 1500 nm for a 40-µm-long grating (period 500 nm, fill factor 0.35) the excess loss increased from ~ 0.5 dB for a total ridge height of 10 nm to ~ 14 dB for 60-nm-high ridges.

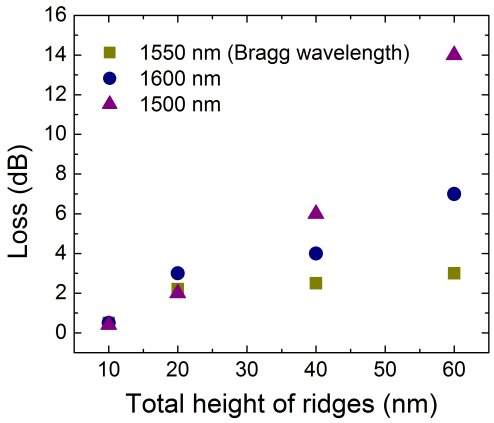

Figure 6.14 Excess loss at the Bragg wavelength and wavelengths below and above the resonance for different heights of the ridges. 40-µm-long grating, period is 500 nm, fill factor is 0.35.

The difference in the level of out-of-plane scattering at the different wavelengths can also be illustrated using microscope images. Images, taken with a camera positioned over the sample, showed much less out-of-plane scattering (in the direction perpendicular to the waveguide plane) at the wavelength close to the Bragg condition (1550 nm) than at wavelengths away from the resonance (1500 and 1600 nm) (Figure 6.15). It should be mentioned that for the visualization of the out-of-plane scattering, gratings with very high ridges were used (total height 90 nm) since for lower ridges, the level of the out-of-plane scattering was too weak for detection in the setup.

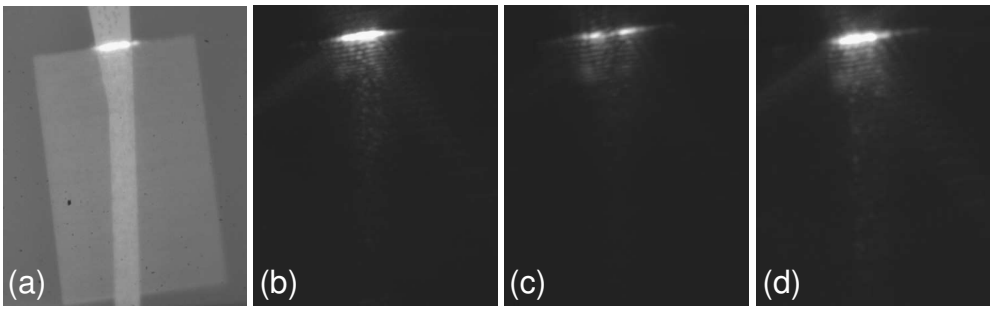

Figure 6.15 Optical microscope images showing **(a)** top view of an 80-µm-long grating (period is 500 nm, fill factor is 0.2) placed at 5° on an 8-µm-wide stripe waveguide with the LR-SPP excitation at **(b)** 1500 nm, **(c)** 1550 nm (close to the Bragg wavelength), and **(d)** 1600 nm. Total ridge height is 90 nm.

6.3 Comparison with the lossless Bragg grating

6.3.1 Effective index modulation and bandwidth

For a lossless uniform Bragg grating, the effective refractive index modulation and FWHM bandwidth can be found using the following approximations [122]:

$$R_{\max} = \tanh^2\left(\frac{\pi \Delta n \eta L}{\lambda_B}\right) \qquad [6.14]$$

$$\Delta\lambda = \alpha\lambda_B\sqrt{\left(\frac{\Delta n}{n_{eff}}\right)^2 + \left(\frac{\Lambda}{L}\right)^2} \qquad [6.15]$$

where η is a confinement factor (a measure of the overlap integral between the incoming mode and the grating, typically ~1 for normal incidence) and α is a tuning parameter: $\alpha \approx 1$ for strong gratings (maximum reflection close to 100%) and $\alpha \approx 0.5$ for weak gratings.

Using Eq. [6.14], the effective refractive index modulation, Δn, in LR-SPP gratings was estimated for different fill factors and ridge heights (Figure 6.16). The highest Δn was obtained for fill factor ~ 0.5. The effective index modulation was found to increase with the ridge height similar to one-dimensional etched Bragg gratings [118], having a dielectric contrast proportional to the ridge height until a total ridge height of ~ 20 nm. The same tendency was shown by theoretical simulations [105].

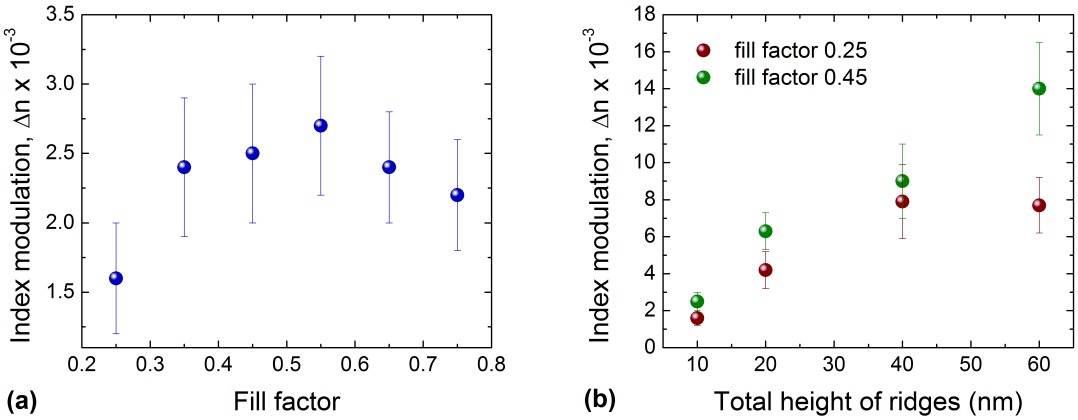

Figure 6.16 Effective index modulation vs. **(a)** fill factor (total height of the ridges is 10 nm) and **(b)** total height of the ridges (fill factors are 0.25 and 0.45).

The values for the FWHM bandwidth, calculated using [6.15], were found to be in good agreement with the values obtained experimentally (Figure 6.17).

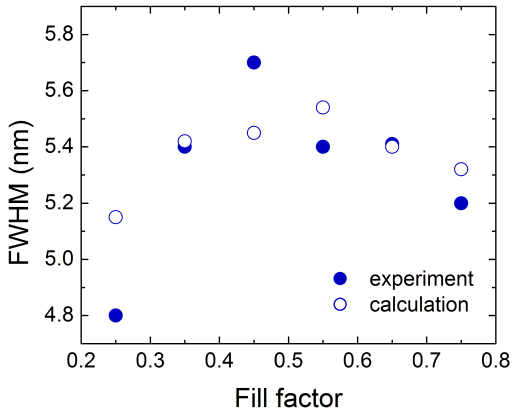

Figure 6.17 FWHM for 160-µm-long Bragg gratings. Grating period is 500 nm, total ridge height is 10 nm.

6.3.2 Estimation of the grating strength

The grating strength for strong gratings can be estimated from the reflection spectra zero-points [120,123]. The zero-condition for δ (Eq. [6.8]) yields the reflection spectrum zeros at the wavelengths:

$$\lambda_m = \lambda_B \left(1 + m \frac{\Lambda}{L} \sqrt{\left(\frac{|\kappa| L}{m\pi} \right)^2 + 1} \right) \quad m = \pm 1, 2 \ldots \qquad [6.16]$$

This expression can only be used for strong gratings ($\kappa L > 1$) since, in the weak-grating regime ($\kappa L < 1$), the position of the zero points is independent of κ and depends only on the grating length (or number of grating lines L/Λ).

For strong gratings, the grating strength can be estimated from the two first order zero points λ_{+1} ($m = +1$) and λ_{-1} ($m = -1$):

$$|\kappa| L = \pi \sqrt{\left(\frac{\lambda_{+1} - \lambda_{-1}}{\lambda_{+1} + \lambda_{-1}} \cdot \frac{L}{\Lambda} \right)^2 - 1} \qquad [6.17]$$

This analysis was performed for strong (long) gratings yielding the dependence of the reflectivity per unit length on the fill factor for different heights of the ridges (Figure 6.18). The dependence of the grating strength on the fill factor was not very pronounced showing only a slight increase for fill factors around 0.5. This agrees with the results obtained for the effective index modulation, when the values for Δn were found to be largest for fill factor around 0.5 (Figure 6.16).

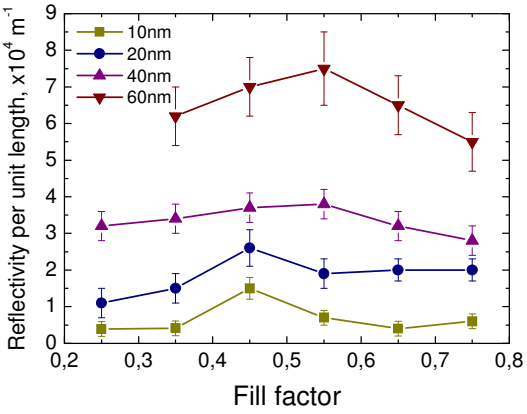

Figure 6.18 The dependence of the grating strength (reflectivity per unit length) on the fill factor for different heights of the ridges. The total height of the ridges changes from 10 nm to 60 nm (from ~ 5 to 30 nm on each side of the waveguide plane).

The grating strength was found to increase with the increasing height of the ridges. For example, for a fill factor of 0.35, the reflectivity per unit length was found to change from ~ $0.4 \cdot 10^4$ for a total ridge height of 10 nm to ~ $6 \cdot 10^4$ m^{-1} for 60-nm-high ridges.

6.4 Double-reflecting grating

To demonstrate the potential of Bragg-grating structures for LR-SPPs, a compact wavelength add-drop filter operating at ~ 1550 nm was designed and fabricated. This device consisted of two ridge gratings placed at the intersections of straight waveguides arranged in a zigzag configuration with an angle of 10˚ between the stripes (Figure 6.19).

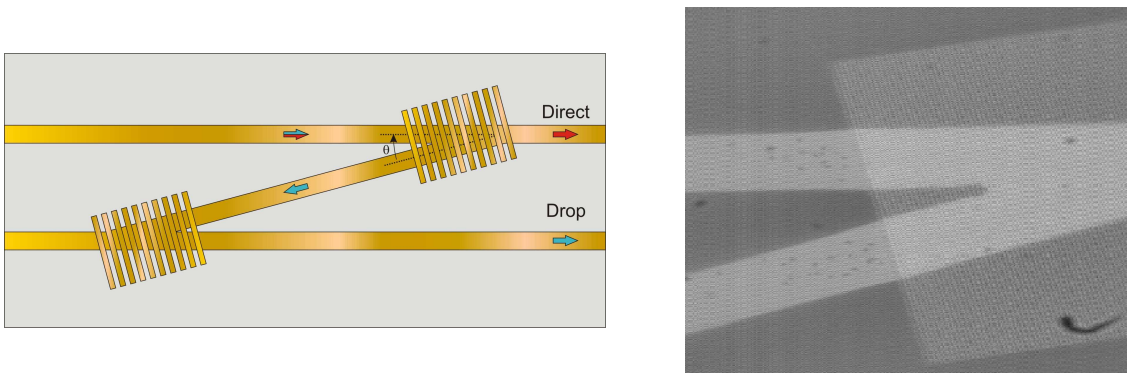

Figure 6.19 (Left) Schematic and **(right)** microscope image of the double-reflective-grating zigzag configuration, consisting of two reflective gratings placed on the intersections of straight waveguides, as an example of a simple add-drop filter. The angle between the waveguide is 20 degrees. Total height of the ridges is 40 nm.

The performance of 80-µm-long angled gratings with a total height of the ridges of 40 nm is shown in Figure 6.20. The transmission spectrum through the direct arm showed a 15-dB dip centered around 1551 nm representing transmission through one angled grating. The "drop"-signal, built up by double reflection from two angled gratings, featured a reflection peak at 1549 nm with a FWHM of approximately 13 nm.

The total power curve showed the same behavior as in the case of normal-incidence gratings. The excess loss of the device was found to be ~ 4.5 dB at the Bragg wavelength, increasing to ~ 8 and 5 dB in the short- and long-wavelength regions, respectively.

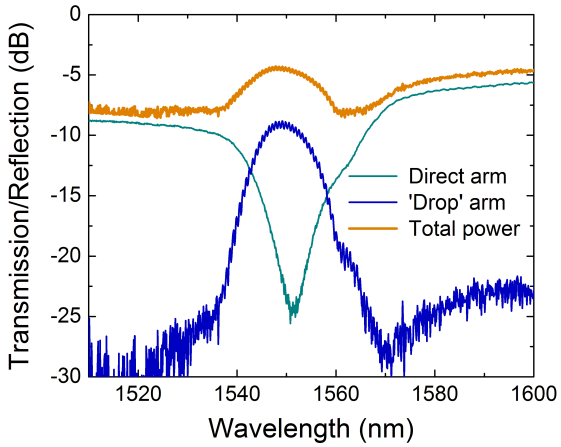

Figure 6.20 Performance of the double-reflective-grating device consisting of 80-µm-long gratings (period is 500 nm, fill factor is 0.4): Transmitted signal through the direct and drop arms together with the spectrum of the total power. The angle between the waveguides is 10 degrees. The total height of the ridges is 40 nm.

6.5 Discussion and conclusions

Things should be made as simple
as possible, but not any simpler.
Albert Einstein

The main observed tendency was that the behavior of shallow ridge gratings (total ridge height < 40 nm) is quite similar to one-dimensional Bragg gratings. In this regime, the dielectric contrast is proportional to the ridge height and the gap in transmission and the peak in reflection (both being centered at the Bragg wavelength $\lambda_B = 2n_{eff}\Lambda$) increase with the increase of the ridge height. For these gratings, the transmission and reflection spectra were found to evolve with the grating length more or less as expected [118]. For larger heights, out-of-plane scattering gradually takes over, and both transmission and reflection characteristics become progressively distorted, eventually smearing out the gap in transmission.

It should be noted that the requirement for low ridge heights limits the efficiency and (wavelength and angular) bandwidth of the LR-SPP interaction with the ridge gratings. The effective index contrast in the grating was found to be on the order of 0.01, which is large enough for realization of efficient and compact Bragg gratings for wavelength selective functions.

7 Summary and Conclusions

It's as large as life, and twice as natural!

Lewis Carroll, "Through the Looking Glass"

This thesis summarizes the work on integrated-optics components, based on the propagation of long-range surface plasmon polaritons (LR-SPPs) along metal stripes embedded in a dielectric. The main focus of the project was on fabrication and optical characterization of different LR-SPP-based waveguide components, ranging from straight and bent waveguides to integrated Bragg gratings.

The simple model for describing optical properties of metals developed by Drude as well as the fundamental properties of surface plasmon polaritons were outlined, including the dispersion relation for SPPs and different methods of SPPs excitation. The properties of long-range SPPs were described both for an infinitely wide metal film and a thin metal stripe of finite width. Using a one-dimensional mode solver, the propagation loss as well as mode profiles were studied for different thicknesses of the metal film and different properties of the cladding layers (thickness, refractive index).

At the wavelength of 1550 nm, a propagation loss of ~ 6 dB/cm and a coupling loss of ~ 0.5 dB (per facet) were obtained for 15-nm-thick stripe waveguides of 8 µm width. An S-bend loss of less than 3 dB was obtained for a 4.5-mm-long S-bend with a 200-µm-offset. The performance of a 3-dB Y-splitter was also shown as well as the realization of multimode-interference devices. Furthermore, directional couplers based on LR-SPP stripe waveguides were investigated and coupling lengths of 1.9 and 0.8 mm were found for directional couplers with 4- and 0-µm-separated waveguides, respectively. A range of LR-SPP waveguide components were modeled using the effective-refractive-index approach, and good agreement with the experimental results was obtained.

LR-SPP propagation in photonic crystal structures, formed by periodic arrays of gold bumps arranged in a triangular lattice and placed symmetrically on both sides of a thin gold film, was also studied. The LR-SPP transmission through and reflection from the PC structures of different lengths and lattice periods as well as LR-SPP propagation along line defects of different widths were investigated. For PC channels, the propagation loss was found to decrease gradually with increasing channel width: from ~ 50 dB/mm for 1-µm-wide channels to ~ 6 dB/mm for 8-µm-wide

channels. The coupling loss between a channel and a stripe waveguide was estimated to be 3 dB for 1-μm-wide channels, decreasing to approximately 0.3 dB for 8-μm-wide channels.

It was found that, in the investigated structures with current parameters (the height of the bumps was from 80 nm to 200 nm on each side and the fill factor varied from 0.15 to 0.25), the coherent multiple LR-SPP scattering is rather weak, so that the PBG effect might be expected to take place only for some particular propagation directions providing only poor field confinement. The possibilities of achieving a full band gap (in the surface plane) for LR-SPPs as well as the use of the weak coherent-scattering effect were, therefore, discussed.

The investigated metallic structures were found to be suitable for the realization of efficient and compact integrated Bragg gratings. The LR-SPP propagation along periodically thickness-modulated metal stripes embedded in a dielectric was experimentally studied in the telecom range for different grating parameters. Experimental findings for LR-SPP ridge Bragg gratings were reported and the lossless Bragg grating model was applied to the investigated LR-SPP gratings, providing estimates for the effective refractive index modulation and bandwidth. The grating strength was also estimated for different heights of the ridges. Finally, the realization of a compact wavelength add-drop filter with a bandwidth of ~ 20 nm centered at 1550 nm was reported.

7.1 Possible applications

Any sufficiently advanced technology
is indistinguishable from magic.
Arthur C. Clarke, "Technology and the Future"

LR-SPP waveguides constitute a new class of components that can provide *guiding* of light as well as *coupling* and *splitting* from/into a number of channels with reasonable insertion loss and good waveguide performance. Conventional passive circuits, including straight and bent waveguides, splitters, MMI devices, directional couplers, can be fabricated on the base of LR-SPP stripe waveguides. Although LR-SPP components support only one polarization and the loss is higher than in standard glass-based technologies, LR-SPP-technology does offer some advantages. In the first place, it is a truly *planar technology* based on a high-quality but simple and low-cost fabrication procedure involving standard photolithography and metallization processes with a high reproducibility. As in the case of standard glass-based technology, *efficient coupling with single mode fibers* (ideally as low as 0.1 dB) is achievable due to the possibility of mode shaping by choosing proper waveguide dimensions. For LR-SPP waveguides, *mode matching* can be realized much easier than, for example, for polymer waveguides, where the desirable mode size requires an exact refractive-index difference between the core and the cladding. Moreover, the design

procedure for LR-SPP waveguide components can be performed quite easily using a numerical mode solver and the effective-refractive-index approach. In addition, the propagation loss of ~ 6 dB/cm can, in principle, be reduced significantly via material and processing optimization. Another appealing feature is that any dielectric material can be used as a cladding for LR-SPP stripe waveguides, which opens up the possibility of combining LR-SPP technology with the conventional *Si-based* technology. Finally, the metal stripes that are used as waveguides can be employed as electrodes carrying signal currents influencing the waveguiding characteristics, e.g., through thermo- or electro-optic effects.

Even though the effective index contrast achieved in the investigated 2D-periodic metallic structures was not sufficient for achieving a full BG (in the surface plane) for LR-SPPs, the results presented in this work should be considered as a first step towards realization of the efficient manipulation of LR-SPPs utilizing the PBG concept and related phenomena. Further investigations within this area should be conducted aiming at eventually making it possible to use this kind of photonic crystals for highly integrated LR-SPP-based optical components.

The efficient and compact *integrated Bragg gratings* that can be realized using LR-SPP technology are becoming widely used in both optical communications [124] and sensors [125] for wavelength selective functions. The integrated Bragg gratings offer advantages over their fiber counterparts since they are not limited by the photorefractive effect and can be made stronger and more compact. A great potential in the devices based on Bragg gratings involving LR-SPPs is therefore foreseen for a variety of applications ranging from lasers with distributed feedback and wavelength filters to biosensors. Moreover, for many applications (e.g. sensors based on light interference), the fact that the LR-SPP based components transmit only one polarization may turn out to be an advantage.

All described features of the LR-SPP technology may eventually lead to numerous applications of LR-SPPs in different fields ranging from integrated circuits to laser optics and bio-sensing.

7.2 Future work

One never notices what has been done;
one can only see what remains to be done.
Marie Sklodowska-Curie

Design, fabrication, and optimization of conventional passive waveguide components, ranging from straight waveguides to couplers, as well as integrated Bragg gratings and 2D photonic crystals

is an ambitious task, which still leaves a lot to be carried out, and hopefully, this thesis can be used as a basis for the future LR-SPP-related research.

Loss mechanisms, propagation and bend loss optimization, performance of Y-splitters and directional couplers, material and processing optimization – these are only few of the many tasks that can be addressed in the "stripe waveguide"-research. In particular, realization of Si-based LR-SPP components is one of the most interesting and promising directions.

Investigation of LR-SPP propagation along periodically thickness-modulated metal stripes is also of great interest and importance both for fundamental and application-oriented research. For example, realization of combined Bragg gratings and couplers as well as development of high-performance apodized and tunable gratings should be carried out in the future.

Different structural geometries are also of interest. For example, during the project, it was observed that LR-SPPs can also be guided by metal nanowires where width and height of the metal stripe are on the same order of magnitude. Symmetrical metal nanowires were found to support LR-SPP propagation with relatively low propagation loss (slightly higher than for a stripe waveguide) combined with polarization properties, very different from those of the metal stripe.

Finally, design, realization and optimization of active LR-SPP components based on thermo- or electro-optic effects, are undoubtedly on the first-priority-list in LR-SPP-research.

It is a hope that many advances in the LR-SPP-related research are to be made in the coming years.

Closing Remarks

"Where shall I begin, please your Majesty?" the White Rabbit asked. "Begin at the beginning," the King said, very gravely, "and go on till you come to the end: then stop."

Lewis Carroll, "Alice's Adventures in Wonderland"

At the end of the thesis, I would like to express my personal feelings concerning the project and the research, which has been carried out. As for many PhD students, it was a little tough to find the right direction at the beginning, and after a while, I was truly lucky to find myself working within such an interesting area as LR-SPPs where almost nothing had been investigated before. Sometimes it felt that I had learnt a lot about long-range surface plasmon polaritons, sometimes – that I did not understand anything at all… And it still does. Up and down, raise and fall, encouraging discoveries and frustrating results – always something new. It is my feeling that this is how it should be if it is real, intriguing and fascinating research.

It was a really great experience to work with such a dynamic and motivated team at MMP! Exciting physics revealed itself in a kaleidoscope of interesting experiments, thrilling results, heated discussions and revolutionary ideas. It was a great time. It was a time, when a beautiful sunset through tender clouds on the way home reminded one of the output modes of stripe waveguides [126].

…It began at the beginning and has to go on… So it will.

Publications

This thesis is partly based on the work presented in the following publications and talks:

Journal papers:

1. S. I. Bozhevolnyi, A. Boltasseva, T. Søndergaard, T. Nikolajsen, and K. Leosson, "Photonic band gap structures for long-range surface plasmon polaritons", accepted to Optics Communications (2004)
2. A. Boltasseva, T. Nikolajsen, K. Leosson, K. Kjaer, M. S. Larsen, and S. I. Bozhevolnyi, "Integrated optical components utilizing long-range surface plasmon polaritons", accepted to Journal of Lightwave Technology (2004)
3. A. Boltasseva, T. Søndergaard, T. Nikolajsen, K. Leosson, S. I. Bozhevolnyi, and J. M. Hvam, "Propagation of long-range surface plasmon polaritons in photonic band gap structures", accepted to Journal of the Optical Society of America B (2004)
4. P. S. Carney, R. A. Frazin, S. I. Bozhevolnyi, V. S. Volkov, A. Boltasseva, and J. C. Schotland, "A computational lens for the near-field," Physical Review Letters, 92, 163903-1/4 (2004)
5. S. I. Bozhevolnyi, V. S. Volkov, A. Boltasseva and K. Leosson, "Local excitation of surface plasmon polaritons in random surface nanostructures", Optics Communications, 223, 25-29 (2003)
6. V. S. Volkov, S. I. Bozhevolnyi, K. Leosson and A. Boltasseva, "Experimental studies of surface plasmon polariton band gap effect", Journal of Microscopy, 210, 324-329 (2003)
7. S. I. Bozhevolnyi, V. S. Volkov, K. Leosson and A. Boltasseva, "Surface plasmon polariton waveguiding in random surface nanostructures", Journal of Microscopy, 209, 209-213 (2003)
8. S.I. Bozhevolnyi, V.S. Volkov, T. Søndergaard, A. Boltasseva, P.I. Borel and M. Kristensen, "Near-field imaging of light propagation in photonic crystal waveguides: Explicit role of Bloch harmonics", Physical Review B, 66, paper 235204, 1-9 (2002)

9. S. I. Bozhevolnyi, V. Volkov, J. Arentoft, A. Boltasseva, T. Søndergaard and M. Kristensen, "Direct mapping of light propagation in photonic crystal waveguides", Optics Communications, 212, 51-55 (2002)
10. J. Arentoft, T. Søndergaard, M. Kristensen, A. Boltasseva, M. Thorhauge and L. Frandsen, "Low-loss silicon-on-insulator photonic crystal waveguides", Electronics Letters, 38, 274-275 (2002)
11. S. I. Bozhevolnyi, V. Volkov, K. Leosson and A. Boltasseva, "Bend loss in surface plasmon polariton band gap structures", Applied Physics Letters, 79, 1076-1078 (2001)
12. T. Sondergaard, J. Arentoft, A. Boltasseva, A. Lavrinenko, M. Kristensen and B. Tromborg, "Planar photonic crystal waveguide", DOPS-NYT, 2, 35-39 (2001)

Conference contributions (invited):

1. M. Kristensen, A. Boltasseva, P.I. Borel, L.H. Frandsen, M. Thorhauge and B. Tromborg, "Integrated photonic crystal waveguide technology in Europe", ACOFT, Sydney, Australia, July 2002
2. J. Erland, S.I. Bozhevolnyi, V.S. Volkov, K. Leosson, J.J. Larsen, J.R. Jensen, J. Broeng, H. Simonsen, A. Bjarklev, P.M.W. Skovgaard, A. Boltasseva, and J.M. Hvam, "Photonic Bandgap Components in Optical Communication", CLEO focus meeting on "Non Linear Devices and Applications to Photonics", Munich, Germany, June 2001

Regular conference contributions:

1. A. Boltasseva, T. Nikolajsen, K. Leosson, T. Søndergaard, S. I. Bozhevolnyi, and J. M. Hvam, "Guiding of long-range surface plasmon polaritons along channels in periodic arrays of scatterers", IFC6, CLEO/QELS 2004, San Francisco, California, USA, May 2004
2. K. Leosson, T. Nikolajsen, A. Boltasseva, T. Søndergaard and S. I. Bozhevolnyi, "Photonic bandgap structures for guiding of long-range surface plasmon polaritons", ECOC-IOOC 2003 Proceedings, 5, 70-71, Rimini, Italy, September 2003
3. P.I. Borel, L.H. Frandsen, M. Thorhauge, A. Boltasseva, J. Cheng, M. Kampanis, M. Kristensen, A. Lavrinenko, K. Rechendorff, R. Shim, Y. Zhuang and H.M.H. Chong, "Very low losses for TM polarized light in photonic crystal waveguides", JWC3, CLEO/QELS 2003, Baltimore, Maryland, USA, June 2003
4. K. Leosson, S. Bozhevolnyi, V. Volkov, and A. Boltasseva, "Photonic bandgap effect in disordered arrays of scatterers: implications to broadband, low-loss waveguiding", ECOC 2002 Proceedings, P2.5, Copenhagen, Denmark, September 2002

5. M. Thorhauge, M. Kristensen, J. Arentoft, L.H. Frandsen, T. Søndergaard, A. Boltasseva and P.I. Borel, "Reduced coupling loss between fiber and planar photonic crystal waveguides", NANO7/ECOSS-21 Proceedings, Th-P-029 Malmö, Sweden, June 2002
6. A. Boltasseva, J. Arentoft, M. Thorhauge, M. Kristensen, and T. Søndergaard, "Characterization of low-loss SOI photonic crystal waveguides", Proc. 2001 Annual Meeting of the Danish Optical Society, session 4, Aarhus, Denmark, November 2001
7. T. Sondergaard, A. Bjarklev, A. Lavrinenko, B. Tromborg, J. Arentoft, M. Kristensen, and A. Boltasseva, "Theoretical analysis of finite-height planar photonic crystal waveguides", International Workshop on nonlinear Photonic Crystals Proceedings, 28, Kgs. Lyngby, Denmark, October 2001
8. J. Arentoft, M. Kristensen, T. Søndergaard, and A. Boltasseva, "Realization of robust photonic crystal waveguides designed to reduce out-of-plane scattering", ECOC 2001 Proceedings, Th.A.2.6, 592-593, Amsterdam, Netherlands, October 2001
9. J. Arentoft, M. Kristensen, A. Boltasseva, and T. Søndergaard, "Silica/silicon/silica crystal waveguides with 90 degrees bend", Workshop on Photonic and Electromagnetic Crystal Structures, St. Andrews, Scotland and 2 pages in Electromagnetic Crystal Structures, edited by Thomas F. Krauss, St. Andrews, Scotland, June 2001

Other selected contributions:

1. A. Boltasseva, T. Nikolajsen, K. Leosson, S. I. Bozhevolnyi, and J. M. Hvam, "Experimental investigation of long-range surface plasmon polariton bandgap structures", poster presentation at PhD graduate school in Nanoscience and Photonics, Ebeltoft, Denmark, October 2003
2. V. S. Volkov, A. Boltasseva, S. Bozhevolnyi, K. Leosson, J. Erland, "Periodically corrugated metal surface for control of Surface Plasmon Polaritons: Fabrication and characterization", poster presentation at NKT International Summer School in Advanced Photonics, Copenhagen, Denmark, August 2001
3. A. Boltasseva, K. Leosson, "Fabrication of Micro-Structured Metal Surfaces for Integrated Plasmon Optics", talk given at the 6th Raith Meeting on Experimental Lithography Systems, Dortmund, Germany, April 2001

Bibliography

1. Y. P. Li and C. H. Henry, "Silica-based optical integrated circuits" IEE Proceedings Optoelectronics **143**, 263 (1996).

2. R. M. de Ridder, K. Worhoff, A. Driessen, P. V. Lambeck, and H. Albers, "Silicon oxynitride planar waveguiding structures for applications in optical communication" IEEE Journal of Selected Topics in Quantum Electronics **4**, 930 (1998).

3. M. F. Grant, "Integrated optical waveguide devices on silicon for optical communications" IEE Colloquium 'Planar Silicon Hybrid Optoelectronics' **198**, 1-1/10 (1994).

4. R. Chakraborty, "Integrated optical waveguides in $LiNbO_3$: modelling and experimental analysis" Proceedings of the SPIE - The International Society for Optical Engineering **4417**, 278 (2001).

5. R. M. Almeida, "Sol-gel planar waveguides for integrated optics" Journal of Non Crystalline Solids **259**, 176 (1999).

6. L. A. Eldada, "Polymer integrated optics: promise versus practicality" Proceedings of the SPIE - The International Society for Optical Engineering 11 (2002).

7. P. Coudray, P. Etienne, and Y. Moreau, "Integrated optics based on organo-mineral materials" Material Science in Semiconductor Processing **3**, 331 (2000).

8. H. Raether, *Surface Plasmons*, (Springer, Berlin, 1988).

9. W. L. Barnes, A. Dereux, and T. W. Ebbesen, "Surface plasmon subwavelength optics" Nature **424**, 824 (2003).

10. J.-C. Weeber, A. Dereux, and C. Girard, "Plasmon polaritons of metallic nanowires for controlling submicron propagation of light" Physical Review B **60**, 9061 (1999).

11. J.-C. Weeber, J. R. Krenn, A. Dereux, B. Lamprecht, Y. Lacroute, and J.-P. Goudonnet, "Near-field observation of surface plasmon polariton propagation on thin metal stripes" Physical Review B **64**, 045411 (2001).

12. B. Lamprecht, J. R. Krenn, G. Schider, H. Ditlbacher, M. Salerno, N. Felidj, A. Leitner, F. R. Aussenegg, and J. C. Weeber, "Surface plasmon propagation in microscale metal stripes" Applied Physics Letters **79**, 51 (2001).

13. D. Sarid, "Long-range surface-plasma waves on very thin metal films" Physical Review Letters **47**, 1927 (1981).

14. J. J. Burke, G. I. Stegeman, and T. Tamir, "Surface-polariton-like waves guided by thin, lossy metal films" Physical Review B **33**, 5186 (1986).

15. R. Charbonneau, P. Berini, E. Berolo, and E. Lisicka-Skrzek, "Experimental observation of plasmon-polariton waves supported by a thin metal film of finite width" Optics Letters **25**, 844 (2000).

16. T. Nikolajsen, K. Leosson, I. Salakhutdinov, and S. I. Bozhevolnyi, "Polymer-based surface-plasmon-polariton stripe waveguides at telecommunication wavelengths" Applied Physics Letters **82**, 668 (2003).

17. P. Berini, "Plasmon-polariton waves guided by thin lossy metal films of finite width: Bound modes of symmetric structures" Physical Review B **61**, 10484 (2000).

18. Y. Y. Lu and P. L. Ho, "Beam propagation modeling of arbitrarily bent waveguides" IEEE Photonics Technology Letters **14**, 1698 (2002).

19. A. Kumar and S. Aditya, "Performance of S-bends for integrated-optic waveguides" Microwave and Optical Technology Letters **19**, 289 (1998).

20. H. v. Brug, F. H. Groen, Y. S. Oei, J. W. Pedersen, E. C. M. Pennings, D. K. Doeksen, and J. J. G. M. v. d. Tol, "Low-loss straight and curved ridge waveguides in LPE-grown GaInAsP" Electronics Letters **25**, 1330 (1989).

21. R. C. Alferness, "Guided-wave devices for optical communication" IEEE Journal of Quantum Electronics **17**, 946 (1981).

22. L. B. Soldano and E. C. M. Pennings, "Optical mulit-mode interference devices based on self-imaging: Principles and applications" Journal of Lightwave Technology **13**, 615 (1995).

23. B. Hecht, H. Bielefeld, L. Novotny, Y. Inouye, and D. W. Pohl, "Local excitation, scattering, and interference of surface plasmons" Physical Review Letters **77**, 1889 (1996).

24. I. I. Smolyaninov, D. L. Mazzoni, and C. C. Davis, "Imaging of surface plasmon scattering by lithographically created individual surface defects" Physical Review Letters **77**, 3877 (1996).

25. J. R. Krenn, R. Wolf, A. Leitner, and F. R. Aussenegg, "Near-field optical imaging the surface plasmon fields of lithographically designed nanostructures" Optics Communications **137**, 46 (1997).

26. S. I. Bozhevolnyi and F. A. Pudonin, "Two-dimensional micro-optics of surface plasmons" Physical Review Letters **78**, 2823 (1997).

27. S. I. Bozhevolnyi and V. Coello, "Elastic scattering of surface plamon polaritons: Modeling and experiment" Physical Review B **58**, 10899 (1998).

28. A. Bouhelier, Th. Huser, J. M. Freyland, H.-J. Guntherodt, and D. W. Pohl, "Plasmon transmissivity and reflectivity of narrow grooves in a silver film" Journal of Microscopy **194**, 571 (1999).

29. C. Sonnichsen, A. C. Duch, G. Steininger, M. Koch, G. v. Plessen, and J. Feldmann, "Launching surface plasmons into nanoholes in metal films" Applied Physics Letters **76**, 140 (2000).

30. H. Ditlbacher, J. R. Krenn, G. Schider, A. Leitner, and F. R. Aussenegg, "Two-dimensional optics with surface plasmon polaritons" Applied Physics Letters **81**, 1762 (2002).

31. S. I. Bozhevolnyi, J. Erland, K. Leosson, P. M. W. Skovgaard, and J. M. Hvam, "Waveguiding in surface plasmon polariton band gap structures" Physical Review Letters **86**, 3008 (2001).

32. S. I. Bozhevolnyi, V. S. Volkov, K. Leosson, and A. Boltasseva, "Bend loss in surface plasmon polariton band-gap structures" Applied Physics Letters **79**, 1076 (2001).

33. S. I. Bozhevolnyi, V. S. Volkov, K. Leosson, and J. Erland, "Observation of propagation of surface plasmon polaritons along line defects in a periodically corrugated metal surface" Optics Letters **26**, 734 (2001).

34. J. D. Joannopoulos, R. D. Meade, and J. N. Winn, *Photonic Crystals: Molding the flow of light*, (Princeton University Press, Princeton, 1995).

35. R. H. Ritchie, E. T. Arakawa, J. J. Cowan, and R. N. Hamm, "Surface-plasmon resonance effect in grating diffraction" Physical Review Letters **21**, 1530 (1968).

36. S. C. Kitson, W. L. Barnes, and J. R. Sambles, "Full photonic band gap for surface modes in the visible" Physical Review Letters **77**, 2670 (1996).

37. M. Kretschmann and A. A. Maradudin, "Band structures of two-dimensional surface-plasmon polaritonic crystals" Physical Review B **66**, 245408-245408-8 (2002).

38. S. I. Bozhevolnyi and V. S. Volkov, "Multiple-scattering dipole approach to modeling of surface plasmon polariton band gap structures" Optics Communications **198**, 241 (2001).

39. T. Søndergaard and S. I. Bozhevolnyi, "Vectorial model for multiple scattering by surface nanoparticles via surface polariton-to-polariton interactions" Physical Review B **67**, 165405-165405-8 (2003).

40. F. I. Baida, D. Van Labeke, Y. Pagani, B. Guizal, and M. Al Naboulsi, "Waveguiding through a two-dimensional metallic photonic crystal" Journal of Microscopy **213**, 144 (2004).

41. P. Drude, "Zur Elektronentheorie I" Annalen der Physik **1**, 566 (1900).

42. M. Born and E. Wolf, *Principles of Optics*, (Cambridge University Press, Cambridge, 1980).

43. M. A. Ordal, R. J. Bell, R. W. Alexander, J. L. L. Long, and M. R. Querry, "Optical properties of fourteen metals in the infrared and far infrared: Al, Co, Cu, Au, Fe, Pb, Mo, Ni, Pd, Pt, Ag, Ti, V, and W" Applied Optics **24**, 4493 (1985).

44. R. H. Ritchie, "Plasma losses by fast electrons in thin films" Physical Review **106**, 874 (1957).

45. Z. Salamon, Y. Wang, J. L. Soulages, and M. F. Brown, "Surface plasmon resonance spectroscopy studies of membrane proteins: Transducin binding and activation by rhodopsin monitored in thin membrane films" Biophysical Journal **71**, 283 (1996).

46. J. Zenneck, "Uber die Fortpflanztmg ebener elektro-magnetischer Wellen langs einer ebenen Leiterflache und ihre Beziehung zur drahtlosen Telegraphie" Annalen der Physik **23**, 846 (1907).

47. A. Sommerfeld, "Über die Ausbreitung der Wellen in der drahtlosen Telegraphie" Annalen der Physik **28**, 665 (1909).

48. C. J. Powell and J. B. Swan, "Effect of oxidation on the characteristic loss spectra of aluminum and magnesium" Physical Review **118**, 640 (1960).

49. J. R. Sambles, G. W. Bradbery, and F. Yang, "Optical excitation of surface plasmons: an introduction" Contemporary Physics **32**, 173 (1991).

50. S. J. Al-Bader, "Optical transmission on metallic wires - fundamental modes" IEEE Journal of Quantum Electronics **40**, 325 (2004).

51. E. Kretschmann and H. Raether, "Radiative decay of nonradiative surface plasmons excited by light" Z. Naturforsch. Teil A **23**, 2135 (1968).

52. A. Otto, "Excitation of nonradiative surface plasma waves in silver by the method of frustrated total reflection" Z. Physik **216**, 398 (1968).

53. J. Moreland, A. Adams, and P. K. Hansma, "Efficiency of light emission from surafce plasmons" Physical Review B **25**, 2297 (1982).

54. E. V. Alieva, G. Beitel, L. A. Kuzik, A. A. Sigarev, V. A. Yakovlev, G. N. Zhizhin, A. F. G. van der Meer, and M. J. van der Wiel, "Linear and nonlinear FEL-SEW spectroscopic characterization of nanometer-thick films" Applied Spectroscopy **51**, 584 (1997).

55. W. L. Barnes, W. A. Murray, J. Dintinger, E. Devaux, and T. W. Ebbesen, "Surface plasmon polaritons and their role in the enhanced transmission of light through periodic arrays of subwavelength holes in a metal film" Physical Review Letters **92**, 107401-4 (2004).

56. P. I. Nikitin, A. A. Beloglazov, V. E. Korchergin, M. V. Valeiko, and T. I. Ksenevich, "Surface plasmon resonance interferometry for biological and chemical sensing" Sensors and Actuators, B: Chemical **54**, 43 (1999).

57. L. Xiangang and T. Ishihara, "Sub 100 nm lithography based on plasmon polariton resonance" Digest of Papers Microprocesses and Nanotechnology 2003 139 (2003).

58. B. Moslehi, M. W. Foster, and P. Harvey, "Optical magnetic and electric field sensors based on surface plasmon polariton resonant coupling" Electronics Letters **27**, 951 (1991).

59. K. Kato, H. Tsuruta, T. Ebe, K. Shinbo, F. Kaneko, and T. Wakamatsu, "Enhancement of optical absorption and photocurrents in solar cells of merocyanine Langmuir-Blodgett films utilizing surface plasmon excitations" Materials Science and Engineering: C **22**, 251 (2002).

60. S. Kotsev, C. Dushkin, I. Ilev, and K. Nagayama, "Refractive index of transparent nanoparticle films measured by surface plasmon microscopy" Colloid and Polymer Science **281**, 343 (2003).

61. A. N. Grigorenko, P. I. Nikitin, and G. Steiner, "Dark-field surface plasmon resonance microscopy" Optics Communications **174**, 151 (2000).

62. S. M. Nie and S. R. Emery, "Probing single molecules and single nanopartickes by surface-enhanced Raman scattering" Science **275**, 1102 (1997).

63. P. Berini, "Plasmon-polariton modes guided by a metal film of finite width bounded by different dielectrics" Optics Express **7**, 329 (2000).

64. M. N. Zervas, "Surface plasmon polariton waves guided by thin metal films" Optics Letters **16**, 720 (1991).

65. E. Palik, *Handbook of optical constants of solids*, (Academic, San Diego CA, 1985).

66. H. Kogelnik, *Theory of dielectric waveguides*, T. Tamir, ed., (Springer, Berlin, 1979).

67. W.-P. Huang, "Coupled-mode theory for optical waveguides: an overview" Journal of the Optical Society of America A **11**, 963 (1994).

68. N. S. Kapany and J. J. Burke, *Optical waveguides*, (Academic press, New York and London, 1972).

69. A. Ghatak and K. Thyagarajan, *Introduction to fiber optics*, (Cambridge University Press, New York, 1998).

70. E. Yablonovitch, "Inhibited spontaneous emission in solid-state physics and electronics" Physical Review Letters **58**, 2059 (1987).

71. S. John, "Strong localization of photons in certain disordered dielectric superlattices" Physical Review Letters **58**, 2486 (1987).

72. Yu. A. Vlasov and S. J. McNab, "Losses in single-mode silicon-on-insulator strip waveguides and bends" Optics Express **12**, 1622 (2004).

73. W. Bogaerts, D. Taillaert, B. Luyssaert, P. Dumon, J. Van Campenhout, P. Bienstman, D. Van Thourhout, R. Baets, V. Wiaux, and S. Beckx, "Basic structures for photonic integrated circuits in silicon-on-insulator" Optics Express **12**, 1583 (2004).

74. E. Yablonovitch, "Photonic bang-gap structures" Journal of the Optical Society of America B **10**, 283 (1993).

75. T. F. Krauss and R. M. De La Rue, "Photonic crystals in the optical regime - past, present and future" Progress in Quantum Electronics **23**, 51 (1999).

76. M. Notomi, A. Shinya, S. Mitsugi, E. Kuramochi, and H.-Y. Ryu, "Waveguides, resonators and their coupled elements in photonic crystal slabs" Optics Express **12**, 1551 (2004).

77. T. F. Krauss, Y. P. Song, S. Thoms, C. D. W. Wilkingson, and R. M. De La Rue, "Fabrication of 2-D photonic bandgap structures in GaAs/AlGaAs" Electronics Letters **30**, 1444 (1994).

78. K. M. Ho, C. T. Chan, C. M. Soukoulis, R. Biswas, and M. Sigalas, "Photonic band-gaps in three-dimensions - new layer-by-layer periodic structures" Solid State Communications **89**, 413 (1994).

79. C. Cheng and A. Scherer, "Fabrication of photonic band gap crystals" Journal of Vacuum Science and Technology B **13**, 2696 (1995).

80. R. Brown and O. McMahon, "Large electromagnetic stop bands in metallodielectric photonic crystals" Applied Physics Letters **67**, 2138 (1995).

81. V. N. Astratov, "Photonic band structures of 3D ordered silica matrices" Superlattices and Microstructures **22**, 392 (1997).

82. J. C. Knight, J. Broeng, T. A. Birks, and P. St. Russel, "Photonic band gap guidance in optical fibers" Science **282**, 1476 (1998).

83. M. Charlton and G. Parker, "Nanofabrication of advanced waveguide structures incorporating a visible photonic band gap" Journal of Micromechanics and Microengineering **8**, 172 (1998).

84. S. Lin, J. Fleming, D. Hetherington, B. Smith, R. Biswas, K. Ho, M. Sigalas, W. Zubrzycki, S. Kurtz, and J. Bur, "A three-dimensional photonic crystal operating at infrared wavelengths" Nature **394**, 251 (1998).

85. J. G. Fleming and S.-Y. Lin, "Three-dimensional photonic crystal with a stop band from 1.35 to 1.95 μm" Optics Letters **24**, 49 (1999).

86. E. Yablonovitch, T. Gmitter, and K. Leung, "Photonic band structure: The face-centred-cubic case emloying nonscherical atoms" Physical Review Letters **67**, 2295 (1991).

87. S. Kawakami, "Fabrication of submicrometre 3D periodic structures composed of Si/SiO_2" Electronics Letters **33**, 1260 (1997).

88. A. A. Zakhidov, R. Baudhman, Z. Iqbal, C. Cui, I. Khayrullin, S. Dantas, J. Marti, and V. Ralchenko, "Carbon structures with three-dimensional periodicity at optical wavelengths" Science **5390**, 897 (1998).

89. S.-Y. Lin and J. G. Fleming, "A three-dimensional optical photonic crystal" Journal of Lightwave Technology **17**, 1944 (1999).

90. E. Ozbay, E. Michel, G. Tuttle, R. Biswas, M. Sigalas, and K.-M. Ho, "Micromachined millimeter-wave photonic band gap crystals" Applied Physics Letters **64**, 2059 (2004).

91. T. Søndergaard, J. Arentoft, A. Boltasseva, A. Lavrinenko, M. Kristensen, and B. Tromborg, "Planar photonic crystal waveguides" DOPS-NYT **16**, 35 (2001).

92. H. Benisty, D. Labilloy, C. Weisbuch, C. J. M. Smith, T. F. Krauss, D. Cassagne, A. Beraud, and C. Jouanin, "Radiation losses of waveguide-based two-dimensional photonic crystals:Positive role of the substrate" Applied Physics Letters **76**, 532 (2000).

93. T. F. Krauss, R. M. De La Rue, and S. Brand, "Two-dimensional photonic-bandgap structures operating at near-infrared wavelengths" Nature **383**, 699 (1996).

94. J. Leclercq, H. Hattori, X. Letartre, P. Regreny, P. Rojo-Romeo, C. Seassal, and P. Viktorovitch, "Surface operating photonic devices based on 2D photonic crystal: toward 2.5D microphotonics" Proceedings of SPIE, (2004), pp. 37.

95. C. Jamois, R. B. Wehrspohn, L. C. Andreani, C. Hermann, O. Hess, and U. Gösele, "Silicon-based two-dimensional photonic crystal waveguide" Photonics and Nanostructures - Fundamentals and Applications **1**, 1 (2003).

96. Bogaerts, Wim. Nanophotonic waveguides and photonic crystals in silicon-on-insulator. Ph.D. Thesis. 2003.

97. J. Arentoft, T. Søndergaard, M. Kristensen, A. Boltasseva, M. Thorhauge, and L. H. Frandsen, "Low-loss silicon-on-insulator photonic crystal waveguides" Electronics Letters **38**, 274 (2002).

98. P. Borel, L. H. Frandsen, M. Thorhauge, A. Boltasseva, J. Cheng, M. Kampanis, M. Kristensen, A. Lavrinenko, K. Rechendorff, R. Shim, Y. Zhuang, and H. M. H. Chong, "Very low losses for TM polarized light in photonic crystal waveguides" Conference on Quantum Electronics and Laser Science (QELS) - Technical Digest Series **89**, JWC3-JWC3/2 (2003).

99. S. I. Bozhevolnyi, V. S. Volkov, J. Arentoft, A. Boltasseva, T. Søndergaard, and M. Kristensen, "Direct mapping of light propagation in photonic crystal waveguides" Optics Communications **212**, 51 (2002).

100. J. Arentoft, M. Kristensen, T. Søndergaard, and A. Boltasseva, "Realization of robust photonic crystal waveguides designed to reduce out-of-plane scattering" Proceedings 27th European Conference on Optical Communication **4**, 592 (2001).

101. V. S. Volkov, S. I. Bozhevolnyi, K. Leosson, and A. Boltasseva, "Experimental studies of surface plasmon polariton band gap effect" Journal of Microscopy **210**, 324 (2003).

102. T. Søndergaard and S. I. Bozhevolnyi, "Surface plasmon polariton scattering by a small particle placed near a metal surface: an analytical study" Physical Review B **69**, 45422-45422-10 (2004).

103. M. Kretschmann, "Phase diagrams of surface plasmon polaritonic crystals" Physical Review B **68**, 125419-125419-5 (2003).

104. A. Boltasseva, T. Søndergaard, T. Nikolajsen, K. Leosson, S. I. Bozhevolnyi, and J. M. Hvam, "Propagation of long-range surface plasmon polaritons in photonic band gap structures" submitted to Physical Review B Modeling part is available in Appendix D (2004).

105. S. I. Bozhevolnyi, A. Boltasseva, T. Søndergaard, T. Nikolajsen, and K. Leosson, "Photonic band gap structures for long-range surface plasmon polaritons" submitted to Physical Review Letters (2004).

106. Søndergaard, Thomas. 2004.

107. U. Gruning, V. Lehmann, S. Ottow, and K. Busch, "Macroporous silicon with a complete two-dimensional photonic band gap centered at 5 μm" Applied Physics Letters **68**, 747 (2004).

108. W. Bogaerts, V. Wiaux, D. Taillaert, S. Beckx, B. Luyssaert, and R. Baets, "Fabrication of photonic crystals in silicon-on-insulator using 248 nm deep UV lithography" Journal of Selected Topics in Quantum Electronics **8**, 928 (2002).

109. J. S. Foresi, P. R. Villeneuve, J. Ferrera, E. R. Thoen, G. Steinmeyer, S. Fan, J. D. Joannopoulos, L. C. Kimerling, H. I. Smith, and E. P. Ippen, "Photonic-bandgap microcavities in optical waveguides" Nature **390**, 143 (1997).

110. H. Masuda, H. Yamada, M. Satoh, H. Asoh, M. Nakao, and T. Tamamura, "Highly ordered nanochannel-array architecture in anodic alumina" Applied Physics Letters **71**, 2770 (1997).

111. J. A. Rogers, Z. N. Bao, and L. Dhar, "Fabrication of patterned electroluminescent polymers that emit in geometries with feature sizes into the submicron range" Applied Physics Letters **73**, 294 (1998).

112. G. Agrawal, *Fiber-optics communication systems*, (Wiley Interscience, 1997).

113. H. I. Smith and M. L. Schattenburg, "X-ray lithography, from 500 to 30 nm: X-ray nanolithography" IBM Journal of Research and Development **37**, 319 (1993).

114. M. G. Rosenfield, "Electron-beam lithography for advanced device prototyping: process tool metrology" Journal of Vacuum Science and Technology B **11**, 2615 (1993).

115. V. Berger, O. GauthierLafaye, and E. Costard, "Fabrication of a 2D photonic bandgap by a holographic method" Electronics Letters **33**, 425 (1997).

116. G. D. Emmerson, C. B. E. Gawith, S. P. Watts, R. B. Williams, P. G. R. Smith, S. G. McMeekin, J. R. Bonar, and R. I. Laming, "All-UV-written integrated planar Bragg gratings and channel waveguides through single-step direct grating writing" IEE Proceedings: Optoelectronics **151**, 119 (2004).

117. M. Kulishov, X. Daxhelet, M. Gaidi, and M. Chaker, "Electronically reconfigurable superimposed waveguide long-period gratings" Journal of the Optical Society of America A **19**, 1632 (2002).

118. A. Yariv and P. Yeh, *Optical waves in crystals*, (Wiley, New York, 1984).

119. A. Yariv, "Coupled-mode theory for guided-wave optics" IEEE Journal of Quantum Electronics **9**, 919 (1973).

120. Murphy T.E. Design, fabrication and measurement of integrated Bragg grating optical filters. Ph.D. thesis. 59-74. 2001.

121. J. Ctyroky, S. Helfert, and R. Pregla, "Analysis of a deep waveguide Bragg grating" Optical and Quantum Electronics **30**, 343 (1998).

122. P. J. Russel, J. L. Archambault, and L. Reekie, "Fibre gratings" Phys. World 41 (1993).

123. Madsen, Peter. Private communications. 2004.

124. A. Yariv and M. Nakamura, "Periodic structures for integrated optics" Journal of Quantum Electronics **13**, 233 (1977).

125. J. Ctyroky, F. Abdelmalek, W. Ecke, and Usbeck K., "Modelling of the surface plasmon resonance waveguide sensor with Bragg grating" Optical and Quantum Electronics **31**, 927 (1999).

126. Nikolajsen, Thomas. Private communications. 2003.

127. *Handbook of Microlithography, Micromachining, and Microfabrication*, P. Rai-Choudhury, ed., (SPIE Optical Engineering Press, Washington, 1997).

128. P. S. Carney, R. A. Frazin, S. I. Bozhevolnyi, V. S. Volkov, A. Boltasseva, and J. C. Schotland, "A computational lens for the near-field" Physical Review Letters **92**, 163903-163903-4 (2004).

129. Arentoft, Jesper, Boltasseva, Alexandra, and Jensen, Jesper B. D. Fabrication and characterization of SOI based photonic crystal waveguides at COM. 2001.

130. M. V. Bazylenko and M. V. Bazylenko, "Reactive ion etching of silica structures for integrated optics applications" Journal of Vacuum Science & Technology A **14**, 2994 (1996).

131. L. Novotny, B. Hecht, and D. W. Pohl, "Interference of locally excited surface plasmons" Applied Physics Letters **81**, 1798 (1997).

132. T. Søndergaard and B. Tromborg, "Lippmann-Schwinger integral equation approach to the emission of radiation by sources located inside finite-sized dielectric structures" Physical Review B **66**, 155309-155309-13 (2002).

Appendix A – Electron-Beam Lithography

The term *Lithography* comes from two Greek words, ληθοσ (stone) and γραφω (writing), and originally meant the ink imprint into some spongy material for the purpose of pattern transfer. Today this term has been extended much further and covers all possible types of writing in almost any material.

Electron[8]-beam lithography (EBL), described in detail in Ref. [127], is widely used to fabricate masks for optical lithography and for prototyping [114] as well as nanoscale structures for advanced electronics, optics, and biosciences. This technology was derived from the early scanning electron microscopes and consists in scanning a beam of electrons across a surface covered with a resist film sensitive to those electrons, thus exposing the resist in the desired pattern. The beam of electrons is formed in the same way as inside a usual television but with three orders of magnitude better resolution. The main advantages of the EBL are very high resolution (down to few nm) and flexibility that allows to create an infinite number of different patterns in a vast variety of materials. But the speed of electron-beam writing and the high complexity of the system give the technology drawbacks – the technique is slow (one or more orders of magnitude slower than optical lithography) and expensive. Nevertheless, despite of the low throughput of EBL systems, electron-beam lithography has proven itself to be an indispensable and excellent tool for research and development purposes. This technique is now one of the most utilized methods when making photonic crystals allowing nanometer-scale periodic structures to be created in different material systems (see Figure A.1 and Figure A.2).

The electron-beam lithography system used in this work is a modified field-emission scanning electron microscope (JEOL JSM-6320F) with an external processor (ELPHY nano lithography system, Raith GmbH) that controls the movements of the electron beam. ELPHY software allows to translate mask files (GDSII format) containing the desired pattern into the sequence of exposures.

[8] After the Greek word for amber – electron, or ελεκτρον, as you may know, the earliest electrical experiments involved rubbing amber to produce static electricity

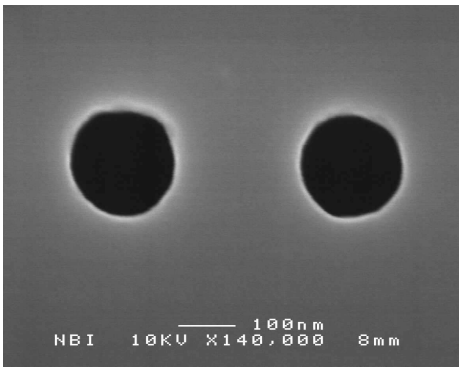

Figure A.1 Holes (approximately 300-nm-deep) etched through Si down to SiO_2 on a silicon-on-insulator wafer using electron-beam resist as a mask (electron-beam lithography was performed at Glasgow University).

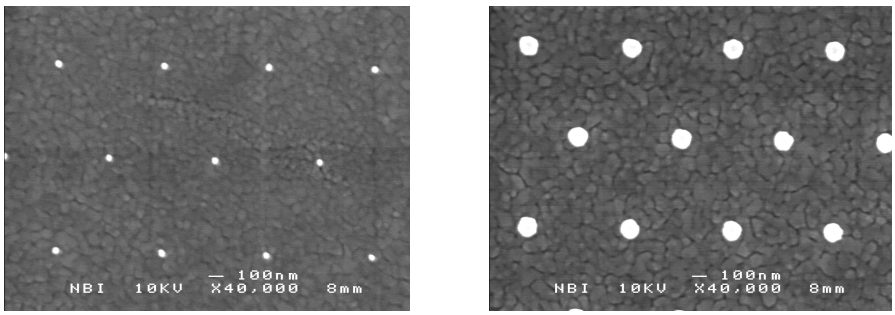

Figure A.2 50-nm-high gold bumps on a glass substrate covered with 45-nm-thick gold film. Bump diameters are approximately **(left)** 65 and **(right)** 170 nm, respectively. The granular pattern is due to the grain structure of the gold surface.

Electron-beam lithography is performed by scanning the substrate, covered with a thin layer of *resist*, with the electron beam. Due to the interaction with the electron beam in the exposed areas, the resist, which is a special type of electron sensitive polymer, undergoes some structural changes and is easily removed by the *developer* solution. The next step is transferring the resist pattern into the sample, which can be performed by different means, for example, by *etching* (notably reactive ion etching [75,93,97,100]) the sample in the areas where the resist has been removed. Another widely used method is a *lift-off* process [75]. In the first step, the surface is covered by a layer of metal and then the unexposed resist is removed in the special-strip solution. This leaves the metal coating only in the exposed areas where the resist has been removed previously in the developer solution.

In practice, there are several types of electron-beam resists that differ from each other by sensitivity (and hence writing speed), resolution and contrast. Normal, or *positive*, electron-beam resist works due to polymer bonds breaking in the exposed areas while in *negative resist* electrons induce formation of bonds between polymer chains making the resist in the exposed areas more difficult to remove by a developer (in that case ZED N50). Both reactions occur simultaneously during exposure, and which one dominates determines whether the resist is positive or negative. In

this work positive electron-beam ZEP-520 resist (Nippon Zeon Co.) was used. This resist is more sensitive (and hence provides faster exposure process) than standard PMMA (polymethyl methacrylate) resist and more resistant to dry etching.

The key parameters of the electron source are the size of the source that determine how small the spot at the target can be, brightness of the source (that can be compared to the intensity in light optics) and the energy spread of the emitted electrons. A large spread in electron energy is undesirable – just like polychromatic light is undesirable in standard lithography, because it makes focusing and other beam operations difficult.

The acceleration voltage defines the penetration depth of electrons into the sample. For low acceleration voltages, the resist generally receives a higher portion of the electron dose and lower sensitivity value is required. It also makes it possible to work with a lower working distance. The value of the acceleration voltage will also affect the degree of proximity effects in the exposure. In all cases, the detailed behavior depends on the substrate type and exposures should be tested at different acceleration voltages when optimizing a given exposure process.

The resolution of the EBL system is mainly determined by a beam diameter and highly depends on the focusing conditions. Magnetic lenses used to focus the electron beam are, of course, not free of *aberrations*, and the two critical aberrations are spherical aberrations and chromatic aberrations. Both of them limit the resolution of the system. In the EBL system used in this project the resolution is approximately 10 nm. Spherical aberrations result from tendency of the outer zones of the lenses to focus more strongly than the center of the lens while chromatic aberrations result from lower energy electrons being focused more strongly than higher energy electrons. Furthermore, although the beam can be focused down to 10-nm spot, it is always a larger area that is exposed by electrons due to electrons being scattered on their way. *Forward scattering* of the electrons, which penetrate the resist, tend to broaden the initial beam diameter. As electrons penetrate through the resist into the substrate, they occasionally undergo large angle scattering events, or *backscattering*, and return back through the resist following a different path, and hereby increase the exposed area. This effect, when the dose received by the pattern feature is affected by electrons scattering from adjacent pattern elements, is called the *proximity effect* and leads to variations in patterns. For example, a narrow line between two large exposed areas may receive so many scattered electrons that it can actually develop away while a small isolated feature may lose so much of its dose due to scattering that it develop incompletely. In that way, in practice, the resolution of the EBL process is not that much determined by the actual resolution of the electron microscope itself – it is rather defined by the type and thickness of the resist and proximity effect as well as the following processing steps. All this has to be taken into consideration when designing structures with very small features.

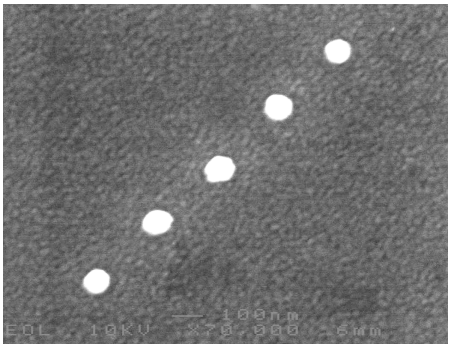

Figure A.3 80-nm-high and gold bumps (diameter ~ 80 nm) on a glass substrate covered with 50-nm-thick gold film. Submicron-pattering procedure developed for a computational lens for the near-field [128]. Granular pattern is due to the grain structure of the gold surface.

Over the years, electron-beam lithography has offered a possibility of manufacturing extremely small structures required by the modern optics and electronics industry for integrated circuits as well as fabrication of nanoscale-patterned samples used for scientific research in different fields [25,114,128] (Figure A.3).

Appendix B – Fabrication of Silicon-on-Insulator-Based Planar Photonic Crystals

The fabrication procedure for making SOI-based photonic crystals waveguides and components has been developed at COM by Arentoft *et. al.* [97,129] within the European IST project "Photonic Integrated Circuits using Photonic Crystal Optics" (PICCO).

Samples, containing planar photonic crystal waveguides and components, consisted of a perforated SiO_2/Si/SiO_2 trilayer film that was manufactured using electron-beam lithography to generate a photonic crystal pattern on top of a SOI wafer (340 nm of Si/1000 nm of SiO_2/Si substrate from SOITEC). Next, holes defined by the exposure were etched into the silicon and after stripping of the resist further down into the silica. As a final processing step, the silicon was thermally oxidized. The whole fabrication procedure is demonstrated in Figure B.1 showing the sequence of processing steps.

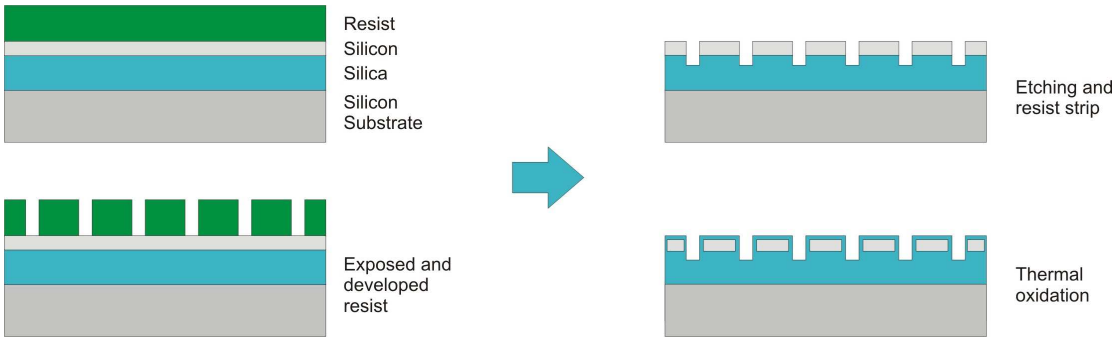

Figure B.1 Schematics of the processing steps for silicon-on-insulator-based planar photonic crystals.

Electron-beam lithography was initially performed at the Niels Bohr Institute (University of Copenhagen) and later on at Glasgow University. First, SOI samples were spin-coated with approximately 100-nm-thick positive electron-beam ZEP-520 resist following by resist pre-baking. Then the designed hole pattern was transferred into the resist by EBL exposure and development processes (Figure B.2). The choice of the resist thickness was based on tests with different resist thicknesses and doses of electron-beam exposure resulting in different hole sizes.

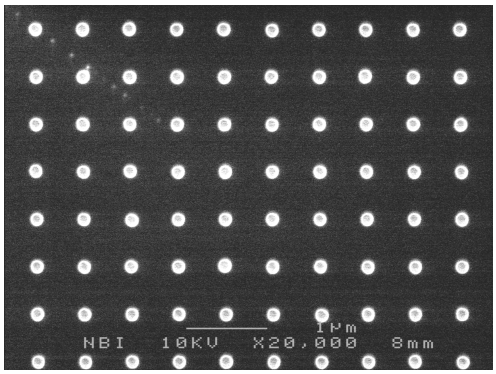

Figure B.2 SEM image of the photonic crystal pattern in 100-nm-thick electron-beam resist, spun on the silicon-on-insulator-wafer, after exposure and development. Hole size is 150 nm.

In order to transfer the pattern into the SOI structure, the reactive ion etching (RIE) technique was used. Compared to other dry-etching methods, RIE allows to obtain very high selectivity over masking material, large etching depths, reduced roughness of etched sidewalls and high degree of anisotropy [130].

For RIE etching of silicon, the electron-beam resist, which was hardened beforehand by post-baking, was used as a mask. The sample was placed into the RIE chamber with a gas mixture of SF_6 and O_2 that etched away the 340-μm-thick silicon layer in the exposed holes in the resist pattern. During the RIE process the resist surface was bombarded by ions. Therefore, some of the resist was also removed, and this should also be taken into account when choosing a proper resist thickness. The rest of the resist was removed by RIE stripping process, which is a pure sputtering process using N_2 and O_2.

Since the propagating mode extends into the silica cladding, the next step after removal of the resist was to transfer photonic crystal pattern further down into the silica substrate. This was again performed by RIE using CHF_3 plasma with patterned silicon layer as an etch mask. As a result of this processing step, the sample was etched approximately 100 nm down into the silica layer.

Finally, the sample was thermally oxidized to introduce a top cladding layer and a glass layer on the inner walls of the air holes. The thickness of thermally grown silica was approximately 60 nm. In addition to the softening of the index step and making the structure more symmetrical, this glass layer might act to reduce scattering losses as during the oxidation process the surfaces of the silicon slab layer become smoother.

An example of a fabricated photonic crystal is shown in Figure B.3 where a PC waveguide was created by removing one row of holes in the PC structure.

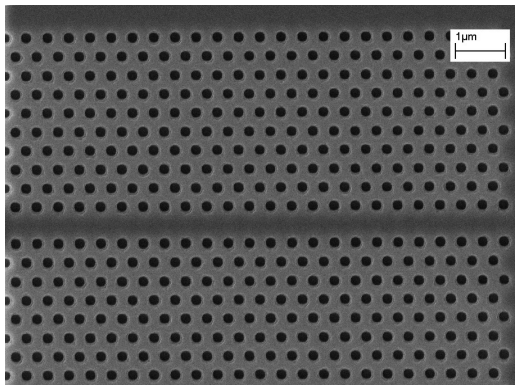

Figure B.3 SEM image of a silicon-on-insulator-based photonic crystal waveguide [98]. Hole size is ~180 nm (scanning electron microscopy performed at COM, Danish Technical University, electron-beam lithography - at Glasgow University).

During the project a lot of samples have been made using facilities at different universities. The decision about transferring electron-beam lithography to Glasgow University was based on the fact that due to instabilities in the EBL system at Ørsted Laboratory of Niels Bohr Institute (University of Copenhagen), the size of the writing field was limited to 40 µm by 40 µm. Even though one could fabricate good quality structures, optical characterization of such tiny photonic crystals was a challenge [97]. Writing a large photonic crystal pattern required a serial process involving aligning different writing fields to each other and using different resolutions, which resulted in poor quality structures due to instabilities in the writing system and stitching errors between adjacent fields. The EBL system in Glasgow University had a maximum writing field of 160 µm and was more advanced in terms of alignment procedure allowing larger photonic crystals to be fabricated without significant writing errors. However, it was indeed difficult to find the right parameters in order to obtain good quality structures with the desirable hole sizes. Quite often due to wrong resist thickness or electron-beam dose, holes were under- or overexposed, resulting in too small holes or the whole photonic crystal area being exposed. Moreover, instabilities and non-uniformities of EBL procedure resulted in poor quality of holes making them non-circular and quite rough (Figure B.4). In order to fabricate PC structures with good performance proximity corrections together with the right parameters for the resist thickness and electron-beam dose are necessary.

According to theoretical predictions, photonic crystals are very sensitive to the structural parameters like dimensions and uniformity, and even small deviations in lattice period or hole size may change the performance quite drastically. It is important to optimize all processes involved starting from electron-beam lithography to thermal oxidation in order to achieve reproducible and high quality structures. This means that the influence of the process tolerances on the properties of photonic crystals has to be fully investigated.

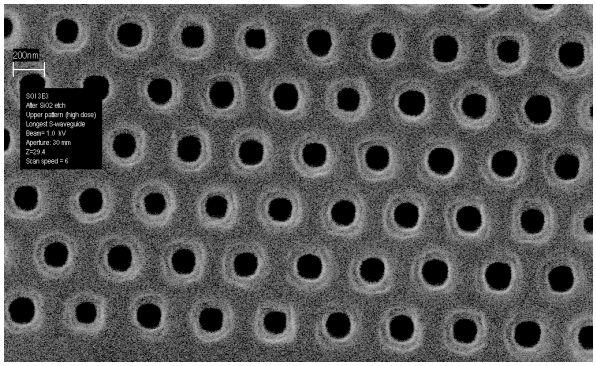

Figure B.4 SEM image of an SOI-based photonic crystal after silica etch. Hole size is ~160 nm. The quality of holes is somewhat poor due to instabilities in EBL procedure (scanning electron microscopy performed at COM, Danish Technical University, electron-beam lithography - at Glasgow University).

Appendix C – Fabrication of Photonic Crystals for Surface Plasmon Polaritons

The fabrication procedure is schematically shown in Figure C.1. For fabricating SPPBG structures, a glass substrate was used as a substrate. First, the glass surface was covered with a thin gold layer with thickness from 40 to 50 nm using thermal evaporation.

In the second step samples were spin-coated with approximately 100-nm-thick positive electron-beam ZEP-520 resist following by resist pre-baking. Then a periodic pattern with a lattice period of approximately 400 nm was transferred into the resist by EBL exposure and development processes. It should be noted that the gold layer should not be much thinner than 50 nm since glass, being a non-conducting material, accumulate charge during exposure, which deflects the electron beam and makes focusing impossible.

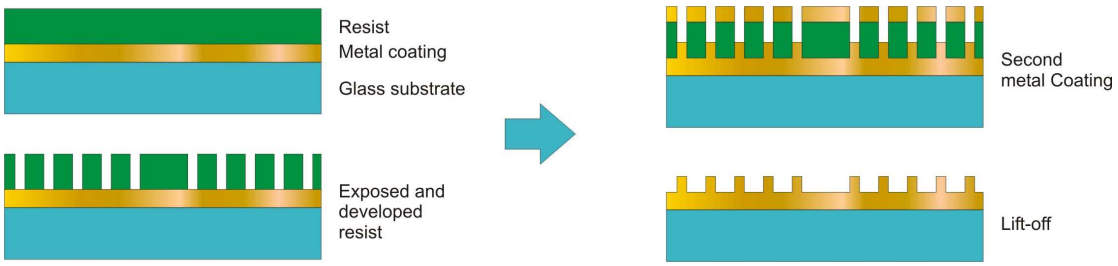

Figure C.1 Schematics of the processing steps for a surface plasmon polariton photonic crystal.

Post-exposure processing of samples involved the second metal coating and lift-off, forming a 2D crystal of gold bumps on the metal surface (Figure 5.4). The diameter of 45-nm-high gold bumps was of the order of 150-200 nm.

Different PC structures for surface plasmon polaritons were fabricated based on triangular or square lattices – straight waveguides of different widths, bent waveguides, double bends, splitters, Z-bending devices, and cavities, in order to study the SPP propagation in 2D PC structures. Few examples of fabricated SPPBG structures with straight and bent linear defects (waveguides) and cavities are shown in the section 5.1.4.

Appendix D – Modeling of Photonic Crystal Structures for Long-Range Surface Plasmon Polaritons

Performed by T. Søndergaard

Scattering of a long-range surface-plasmon-polariton wave by a PC structure can be modeled via the Lippmann-Schwinger integral equation for the electric field

$$\mathbf{E}(\mathbf{r}) = \mathbf{E}^0(\mathbf{r}) + \int \mathbf{G}(\mathbf{r},\mathbf{r}') \cdot k_0^2 \left(\varepsilon(\mathbf{r}') - \varepsilon_{ref}(\mathbf{r}')\right)\mathbf{E}(\mathbf{r}')d^3r' \qquad [6.1]$$

where **r, r'** are spatial positions, $\mathbf{E}^0$ is the incident wave (in our case an LR-SPP wave), k_0 is the free-space wave-number, **G** is the Green's tensor for a reference structure consisting of a thin metal film embedded in a dielectric (the film that supports LR-SPPs), ε_{ref} is the dielectric constant of the reference structure, ε is the dielectric constant of the total structure including the surface particles (bumps), and **E** is the resulting total field, i.e. incident field plus scattered field. The exact Green's tensor **G** is obtained numerically from Sommerfeld integrals [131]. When solving [6.1] by spatial discretization and point-matching, we assume that the external field incident on a particle ($\mathbf{E}^0$ + fields scattered by other particles) is constant across the particle. This approximation, which can be used for sufficiently small particles, is a much better approximation than the frequently employed assumption of the total (self-consistent) field being constant inside (small spherical) particles [38,39,102], as the field inside a small metal particle may vary much faster than the external field.

PC structures with finite-size particles are modeled in two steps. The first step is to calculate the scattered field in the case of a single particle being exposed to various orientations of the incident field. In order to reduce the numerical task of this problem we consider a cylindrically symmetric particle (actually two particles, one at the surface on each side of the metal film). Specifically the gold particle has height 100 nm and radius 150 nm. A procedure for taking advantage of cylindrical symmetry when solving [6.1] has been given in Ref. [132]. Once the field distribution inside the two symmetrically placed particles is known, the total field outside the particles resulting from the scattering process can be calculated by using [6.1]. Since the magnitude of the metal dielectric constant is relatively large it is necessary to apply a gradual transition of the dielectric constant near interfaces to obtain stable convergence. The next step in our method is to solve [6.1] for an array of several hundred particles using the results of scattering for the case of a

single particle. As constant external field across each particle we take the field at the center of the particle due to $\mathbf{E}^0$ and scattering from other particles.

BLOCKS

An example of calculated reflection from and transmission through a 30x30 PC structure with GK orientation for the three lattice constants 550 nm, 570 nm and 600 nm, is shown in Figure D.1. The wavelength step used in the calculation is 3 nm. The agreement between the calculated and experimentally measured wavelength positions of transmission and reflection maxima (cf. Figure 5.22 with Figure D.1) is excellent considering that some differences must be expected because of fabrication tolerances. Furthermore, the size of the PC structure considered in the simulations is smaller than that used in the experiment, and, in the calculation, the thin metal film extends over the whole plane instead of having a finite width metal stripe guiding the LR-SPP to and from the PC structure. However, in this model, the incident beam $\mathbf{E}^0$ is an LRSPP field with a Gaussian field profile (half-width is 4 μm) across the propagation direction, reflecting the confined nature of the real incident LR-SPP modes in stripe waveguides. Reflection and transmission are obtained by evaluating the scattered field and total field, respectively, in the far field (close to the surface but far from the surface scatterers) where the total field is not influenced by non-LR-SPP waves.

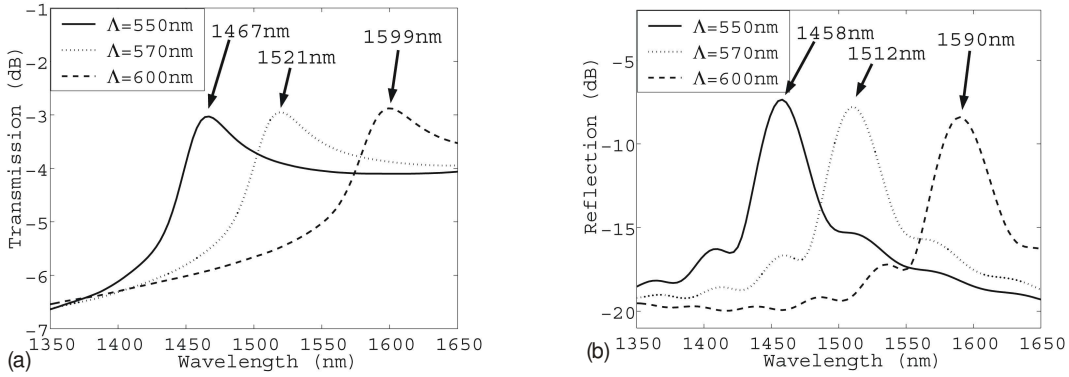

Figure D.1 Calculated transmission **(a)** and reflection **(b)** for a Gaussian LR-SPP incident on a ΓK-oriented array of 30x30 gold scatterers arranged on a triangular lattice on both sides of a 15-nm-thick gold film for three lattice constants Λ. The gold film and particles are surrounded by a material with refractive index 1.5309 (BCB).

Field intensity distributions in the plane located 300 nm above the metal film surface were calculated for different wavelengths showing the pronounced difference between the distribution at the wavelength of 1512 nm (transmission/reflection peak) and those at other wavelengths (Figure D.2). Although these simulations cannot be directly compared to the far-field experimental images shown in Figure 5.19, one can still make the same conjecture from both the numerical and

experimental images, viz., that the LR-SPP field penetrates further into the PC structure when the wavelength matches the Bragg wavelength of 1512 nm.

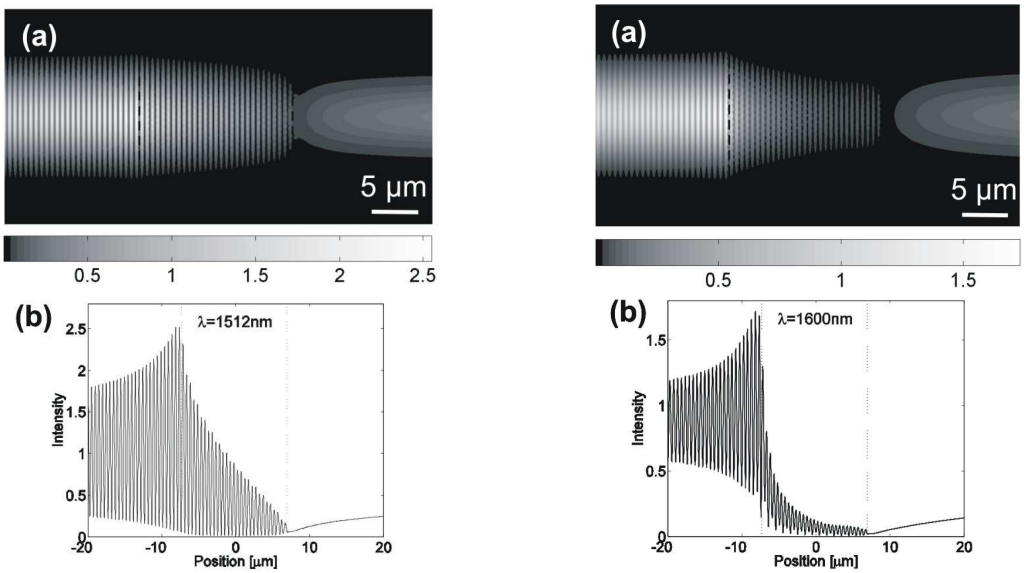

Figure D.2 (a) Electric field intensity calculated 300 nm above the metal film surface for a LR-SPP incident on a 570-nm-period ΓK-oriented array of 30x30 gold scatterers, together with **(b)** its cross section. The wavelength is **(left)** 1512 nm and **(right)** 1600 nm.

Simulation results for the transmission and reflection in the case of GM orientation are shown in Figure D.3.

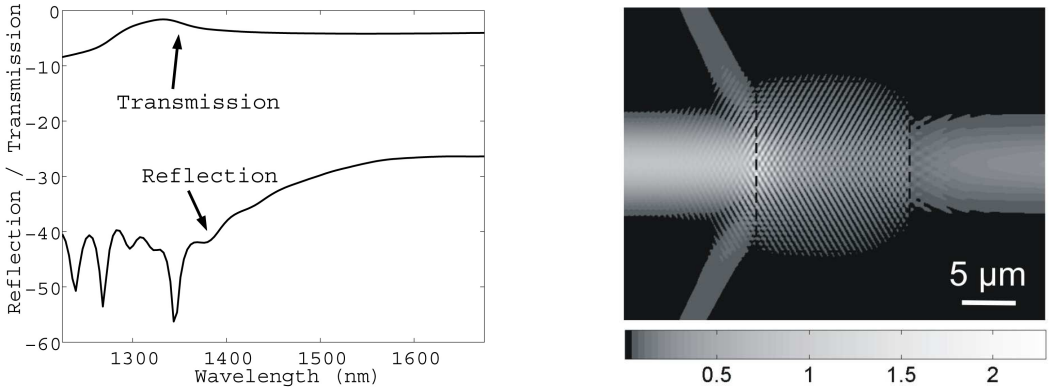

Figure D.3 (Left) Calculated transmission and reflection for a Gaussian LR-SPP incident on a 570-nm-period ΓM-oriented array of 34x26 gold scatterers together with **(right)** the electric field intensity distribution calculated 300 nm above the metal film surface for a LR-SPP incident on a ΓM-oriented array of 30x30 gold scatterers (the wavelength is 1310 nm).

The transmission has a broad maximum centered at the peak wavelength given by [4.2]. The comparison of the calculated and measured spectra indicates that the agreement is reasonably good only for the transmission [cf. Figure 5.20 with Figure D.3]. Note that the reflection is very small in

both cases, but the simulation is not troubled by noise as is the case with the experiment. It is interesting to note that, contrary to the previously considered orientation, the reflection does not increase at the peak transmission wavelength of ~ 1310 nm. The calculated (at 1310 nm) field intensity distribution in the plane located 300 nm above the metal film surface (Figure D.3) clarifies the origin of this difference. One notices that the incident LR-SPP is reflected backwards at angles that deviate 60 degrees from the direction in which the reflection is evaluated (and measured), and this explains the small reflection near the resonance wavelength.

CHANNELS

Simulation results for the transmission and reflection are shown in Figure D.4 for two widths of channels in differently oriented arrays of 30x30 scatterers arranged on a triangular (hexagonal) lattice with lattice constant 570 nm. It is seen that the transmission increases and the reflection decreases as the waveguide is made wider, but the overall shape of the spectra is similar for different widths but different for different orientations. For ΓK orientation, a peak in both the transmission and reflection is seen around the wavelength 1512 nm similar to the case with the PC blocks. For ΓM orientation, the reflection is very small, and the transmission peak around 1310 nm is noticeable, again similarly to the PC structures without waveguides. Note that these similarities agree with those observed in the experimental investigations of the PC blocks and waveguides reported above.

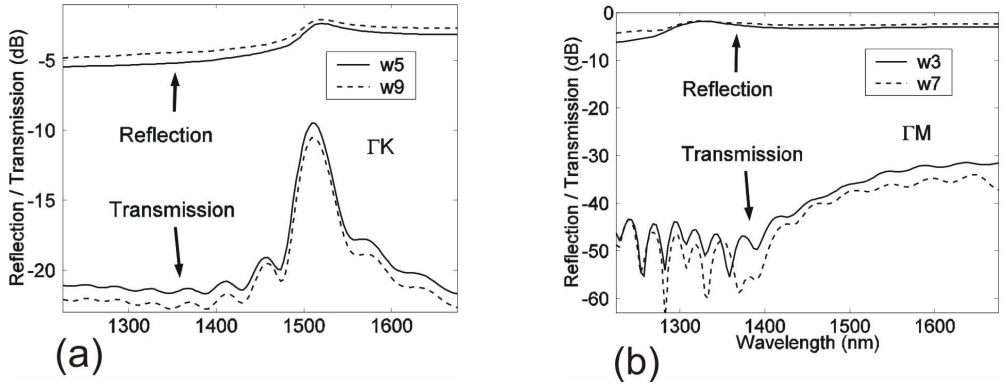

Figure D.4 Calculated transmission and reflection for a Gaussian LR-SPP incident on waveguides created by removing **(a)** 5 (w5) / 9 (w9) rows of scatterers in a ΓK-oriented and **(b)** 3 (w3) / 7 (w7) rows of scatterers in a ΓM-oriented array of 30x30 gold scatterers. The lattice constant is Λ=570 nm.

Modeling allows to investigate the LR-SPP field intensity confinement inside the PC channels for different wavelengths. It turned out that the field confinement is practically absent at the resonance wavelengths given in [4.1] and [4.2]. This feature is illustrated in Figure D.5 ((a) left) for a waveguide of ΓK orientation. At wavelengths away from the resonance, the field confinement

within the waveguide channel can be quite good for both ΓK and ΓM orientations (Figure D.5). The field confinement is further illustrated in Figure D.6 showing the corresponding cross sections of the field intensity distributions with vertical bars that indicate the positions of the first rows of scatterers on each side of the waveguide channels.

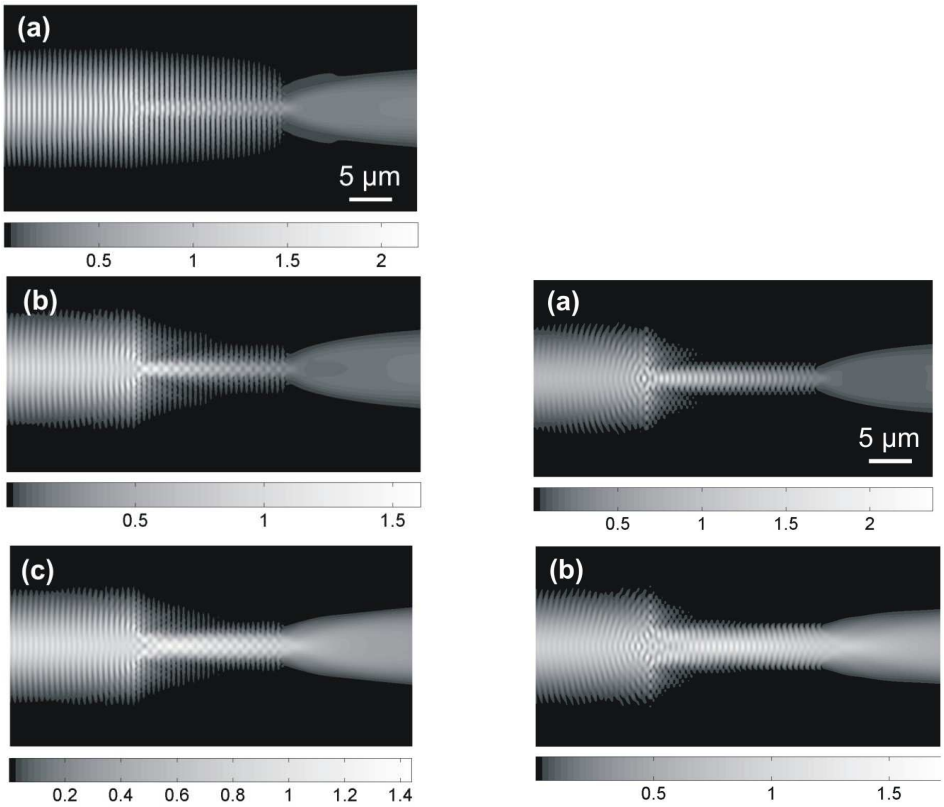

Figure D.5 Calculated field intensity 300 nm above the metal film for a Gaussian LR-SPP incident on **(left)** a waveguide created by removing **(a,b)** 5 or **(c)** 9 rows of scatterers in a ΓK-oriented array (the wavelengths are **(a)** 1512 nm and **(b,c)** 1650 nm) and **(right)** a waveguide created by removing **(a)** 3 or **(b)** 7 rows of scatterers in a ΓM-oriented array of 30x30 gold scatterers (the wavelength is 1650 nm). The lattice constant is Λ=570 nm.

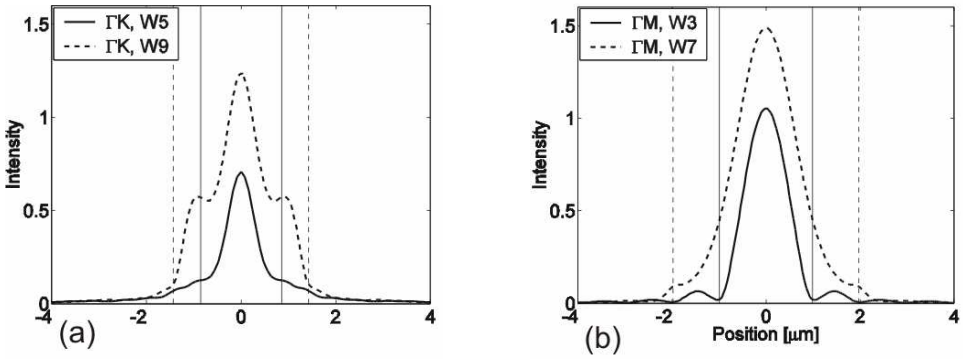

Figure D.6 Cross section of field intensity through the center of the waveguides for the situations in Figure D.5. Cross sections have been chosen with maximum field in the center of the waveguide. The vertical bars show the position of the first row of scatterers on each side of the waveguide region.

Appendix E

Lattice and orientation	Lattice period, nm									
	500		550		570		590		600	
	Est.	Experim.	Est.	Experim.	Est.	Experim.	Est.	Experim.	Est.	Experim.
Triang. ΓK	**1330**	**1335**/1334 (190)	**1462**	**1489**/1480 **1489** (175) **1467**/1467 **1467** (190) **1470**/1466 **1470** (200)	**1515**	**1523**/1524 **1527**/1523 (300) **1540**/1540 **1522**/1547 (360) **1545**/1538 **1521**/1520 (175) **1534** **1524** (165)	**1569**	**1574**/1573 (190)	**1595**	**1600**/1598 (200) **1600** (190)
Triang. ΓM	**1151**		**1266**	**1313** **1311** (175) **1300** (360)	**1312**	**1336** **1344** (300) **1348** **1345** (400) **1350** **1347** (175) **1305** (360)	**1358**	**1385** (360) **1405** (175)	**1381**	
Square	**1535**	**1523**/1520 **1528**/1524 (300) **1530** **1533** (400)								

Table 1 Position of the **(bold)** transmission and **(normal)** reflection peaks for different lattices and periods observed for PC **(black)** blocks and **(blue)** waveguides together with **(red)** the estimations of the peak position from the Bragg grating arguments (Eq. [4.1], [4.2], and [4.3]). Values in parentheses represent the total heights of the bumps for different samples.